



**NTNU – Trondheim**  
Norwegian University of  
Science and Technology

# Acoustic Emission from Arctic Steels and Fractographic Investigations

**Cathrine Gjerstad Hartwig**

Master of Science in Mechanical Engineering

Submission date: June 2015

Supervisor: Christian Thaulow, IPM

Norwegian University of Science and Technology  
Department of Engineering Design and Materials



## PREFACE

This report is the result of the work with the master thesis during the spring of 2015. It is conducted at the department of Product Development and Materials Engineering at NTNU.

The objective of the thesis is a better understanding of brittle fracture using Acoustic Emission to measure the micro-cracking activity. Through the work with the thesis, I have collaborated with Andreas Vrenne Larsen. The theses is written separately, but we have worked together towards the same objective, focusing on different aspects.

I would like to thank my supervisor Christian Thaulow for guidance throughout the work with the thesis. I would also like to thank Odd Magne Akselsen and Erling Østby for sharing their expertise on the subject and Tore Andre Kristensen for conducting the fracture mechanic testing. Last, I would like to thank Andreas Vrenne Larsen for the cooperation through a challenging but also very interesting semester.

Cathrine Gjerstad Hartwig

## PROBLEM DEFINITION

THE NORWEGIAN UNIVERSITY  
OF SCIENCE AND TECHNOLOGY  
DEPARTMENT OF ENGINEERING DESIGN  
AND MATERIALS

### MASTER THESIS SPRING 2015 FOR STUD. TECHN. CATHRINE GJERSTAD HARTWIG

#### **Acoustic Emission from Arctic Steels and Fractographic Investigations**

#### ***Akustisk emisjon fra arktiske stål og bruddflateundersøkelser***

Brittle fracture in steel is a process that is intricately linked to the microstructure in the material. Usually the fracture starts somewhere in front of the macroscopic crack, often associated with some kind of second phase particle. The local crack may propagate to become a global crack or it could possibly be arrested when facing microstructural barriers to further crack growth. The latter is a very interesting phenomenon; however, it is difficult to analyze just based on the traditional mechanical testing, as the events often are too small to cause any visible signs in the load-displacement curves. The use of Acoustic Emission (AE) offers a means to monitor this microcracking activity in more detail. There are several features that can be measured. The number of AE signals (stemming from microcrack nucleation) generated represents the rate of microcrack nucleation. However, recent research carried out also has demonstrated that the amplitude of the AE signal can be linked to the size of the arrested microcrack, allowing more quantitative data to be extracted from the testing. Thus, AE can be a valuable tool to better understand which microstructural features could lead to local crack arrest, and eventually provide valuable input to models for describing brittle fracture in steels.

During the work the candidate shall cooperate closely with stud techn Andreas Vrenne Larsen who will focus on AE measurements and analysis of the recorded AE signals..

The scope of the project thesis is:

- Introduction to AE and summary of the results obtained for Arctic Steels.
- Introduction to fractography and methods to quantify the fracture surfaces.
- Characterization of the microstructure and the fracture surfaces from the screening tests
- Detailed examinations of selected tests to determine the size of arrested microcracks
- Linking of the results to theoretical models for brittle fracture

#### **Formal requirements:**

Three weeks after start of the thesis work, an A3 sheet illustrating the work is to be handed in. A template for this presentation is available on the IPM's web site under the menu




"Masteroppgave" (<http://www.ntnu.no/ipm/masteroppgave>). This sheet should be updated one week before the master's thesis is submitted.

Risk assessment of experimental activities shall always be performed. Experimental work defined in the problem description shall be planned and risk assessed up-front and within 3 weeks after receiving the problem text. Any specific experimental activities which are not properly covered by the general risk assessment shall be particularly assessed before performing the experimental work. Risk assessments should be signed by the supervisor and copies shall be included in the appendix of the thesis.

The thesis should include the signed problem text, and be written as a research report with summary both in English and Norwegian, conclusion, literature references, table of contents, etc. During preparation of the text, the candidate should make efforts to create a well arranged and well written report. To ease the evaluation of the thesis, it is important to cross-reference text, tables and figures. For evaluation of the work a thorough discussion of results is appreciated.

The thesis shall be submitted electronically via DAIM, NTNU's system for Digital Archiving and Submission of Master's theses.



Torgeir Welo  
Head of Division



Christian Thaulow  
Professor/Supervisor



## SUMMARY

There is a need for better understanding of brittle fracture due to an increased interest in exploring the undiscovered hydrocarbon resources in the arctic region. There is also a need for development of steels with better low temperature fracture toughness, as steels are experiencing a drastic decrease in toughness in the HAZ after welding.

This thesis uses acoustic emission in the investigation of the brittle initiation and propagation micromechanisms for a low carbon HSLA steel. Acoustic emission is emitted when a microcrack nucleates, and by monitoring this, it is possible to investigate the crack nucleation rate during loading. Recent research has also demonstrated that the amplitude of the AE signal can be linked to the size of the arrested microcrack. This can be measured using AE monitoring in fracture mechanic testing, by interrupting the loading when the first AE signal is emitted, and then study the fracture surface in SEM.

The work carried out in this thesis covers microstructural analysis and fracture surface investigation in SEM of interrupted fracture mechanic tested samples and samples run to final fracture. The testing is conducted on the HAZ of the steel at low temperatures. The fracture mechanic testing with AE monitoring is conducted by SINTEF, while this thesis uses the results in the discussion of the brittle micromechanisms.

The results indicate that the steel investigated is mostly nucleation controlled in the HAZ, i.e. after a microcrack initiates there is not many obstacles for crack propagation. The crack initiation mechanism seems to be from inclusions induced to a local stress and strain concentration. Perhaps a few large martensite-austenite (M-A) constituents also initiate fracture. These are commonly formed in the HAZ and is regarded as one of the main reasons for the loss of toughness in the HAZ. The low carbon content in the steel seemed to have reduced the amount of large M-A constituents drastically.

The inclusions are widely scattered which are believed to be the reason for the scatter in fracture toughness obtained from testing. The fracture toughness is also lower than what would be expected with the reduction of M-A constituents. The reason for this are assumed to be due to low crack propagation resistance, associated with coarse upper bainite and large prior austenite grains found in the HAZ through microstructural investigation.

There was limited result regarding microcrack arrest (and initiation) due to the samples only emitting a few AE signals during testing. Only one sample had an arrested microcrack that could be linked to the AE signal. It is therefore need for more research on the relation between the size of the arrested microcrack and the AE signal amplitude. It is beneficial that this is conducted on a steel that has better propagation resistance than the steel investigated in this thesis. For monitoring microcrack nucleation on samples running to final fracture, AE is a useful tool.

## SAMMENDRAG

Det er behov for bedre forståelse av sprøbrudd på grunn av økt interesse for å utforske de uoppdagede hydrokarbonressursene i den arktiske regionen. Det er også et behov for utvikling av stål med bedre lavtemperaturbruddseighet, siden stål opplever en drastisk reduksjon i seighet i den varmpåvirkede sonen etter sveising.

Denne masteroppgaven bruker akustisk emisjon i undersøkelse av de sprø initiering og propagerings mikromekanismene for et lavkarbon HSLA stål. Akustisk emisjon avgis når en mikrosprekk initieres, og ved å måle denne er det mulig å undersøke sprekkinitieringshastigheten under påført last. Nylig forskning har også vist at amplituden av AE signalet kan være knyttet til størrelsen av den stoppede mikrosprekken. Dette kan måles ved hjelp av AE i bruddmekanisk testing, ved å avbryte lasten når det første AE signal utsendes, og deretter undersøke bruddflaten i SEM.

Arbeidet som er utført i denne masteroppgaven omhandler mikrostrukturanalyse og bruddflateundersøkelse i SEM av avbrutte bruddmekaniske prøver og prøver kjørt til endelig brudd. Dette er utført på den varmpåvirkede sonen i stålet og ved lave temperaturer. Den bruddmekaniske testingen med AE måling er utført av SINTEF, mens denne oppgaven bruker resultatene i diskusjonen av mikromekanismene for sprøbrudd.

Resultatene indikerer at bruddmekanismen for den varmpåvirkede sonen i det undersøkte stålet hovedsakelig kontrolleres initiering, dvs. etter en mikrosprekk initieres det ikke er mange hindringer for sprekkpropagering. Initieringsmekanismen synes å være fra inneslutninger som også har en lokal spenning og tøyingskonsentrasjon. Det er også mulig at noen få store martensitt-austenitt (M-A) partikler initierer brudd. Disse er ofte dannet i den varmpåvirkede sonen og regnes som en av de viktigste årsakene til tap av seighet i denne sonen. Det lave karboninnholdet i stålet ser ut til å ha redusert mengden av store M-A partikler drastisk.

Inneslutningene ligger veldig spredt på bruddflaten, dette antas å være årsaken til den store spredning i bruddseighetsresultatene fra testingen. Bruddseigheten er også lavere enn hva som ville være forventet med reduksjonen av M-A partikler. Grunnen til dette er antatt å være på grunn av lav sprekkpropageringsmotstand, forbundet med grov øvre bainitt og store austenittkorn som var observert i den varmpåvirkede sonen gjennom mikrostrukturundersøkelse.

De avbrutte prøvene ga et begrenset resultat på grunn av prøvene bare sendte ut et par AE signaler under testing. Bare en prøve hadde en stoppet mikrosprekk som kan være knyttet til AE-signalet. Det er derfor behov for mer forskning på sammenhengen mellom størrelsen på den stoppede mikrosprekken og amplituden til AE signalet. Det er gunstig at dette blir gjennomført på et stål som har bedre propageringsmotstand enn stålet undersøkt i denne masteroppgaven. For overvåking mikrosprekkinitiering på prøver som blir kjørt til endelig brudd er AE et nyttig verktøy.

## NOMENCLATURE

AE	Acoustic Emission
AM	Artic Materials
ASTM	American Society for Testing and Materials
CCT	Continuous Cooling Transformation
CGHAZ	Coarse grained HAZ
CMOD	Crack Mouth Opening Displacement
CTOD	Crack Tip Opening Displacement
EDS	Energy Dispersive Spectroscopy
EPFM	Elastic Plastic Fracture Mechanics
HAZ	Heat-Affected Zone
HSLA	High Strength Low Alloy
ICCGHAZ	Intercritically reheated CGHAZ
LAF	Local Approach to Fracture
LEFM	Linear Elastic Fracture Mechanics
M-A	Martensite-Austenite
RT	Room Temperature
SEM	Scanning Electron Microscope
SENB	Single Edged Notched Beam
TMCP	Thermo-mechanically controlled processing

## LIST OF SYMBOLS

$\gamma$	Austenite
$\alpha$	Ferrite
$A_3$	Austenite to two-phase area transformation temperature
$A_1$	Two-phase area to ferrite transformation temperature
$M_s$	Martensite transformation start temperature
$M_f$	Martensite transformation finish temperature
$T_p$	Peak temperature in welding
$\Delta t_{8-5}$	Cooling time from 800 to 500 °C
$L_{max}$	Maximum length of the M-A constituents
$L_{min}$	Minimum length of the M-A constituents
$L_{max}/L_{min}$	Aspect ratio of the M-A constituents
$X_c$	Length from pre-test fatigue notch to cleavage initiation site
$P_f$	Probability of fracture
$\sigma_{M-A}^c$	Critical stress to fracture a M-A particle
$\sigma_1$	Local maximum principal stress
$\sigma_{pm}$	Critical stress for crack propagation through a particle/matrix interface
$\sigma_{mm}$	Critical stress for crack propagation through a matrix/matrix interface
$\sigma_y$	Yield strength
$K_{IC}$	Stress intensity factor
$J$	J-integral
$a_{micro}$	Length of arrested microcrack
$V_{AE}$	Voltage amplitude in the AE transducer
$D$	Elastic displacement caused by a sudden creation of a circular microcrack
$r$	Radius of a microcrack
$R$	Distance to from the microcrack to the point of observation
$A_{AE}$	dB amplitude of a AE signal
$V_{ref}$	Reference voltage
$A_{pre}$	Amplitude of pre-amplifier



# TABLE OF CONTENTS

Preface.....	i
Problem definition.....	ii
Summary .....	iv
Sammendrag .....	v
Nomenclature.....	vi
List of symbols.....	vii
1. Introduction.....	1
2. Theoretical Background .....	3
2.1 Microstructures.....	3
2.1.1 Equilibrium phases of steel .....	3
2.1.2 Bainite.....	4
2.1.3 Martensite .....	5
2.1.4 Etching.....	6
2.1.5 Grain size determination.....	7
2.1.6 Hardness measurements.....	7
2.1.7 Thermo-mechanically controlled processing (TMCP) .....	8
2.2 Microstructures in the HAZ .....	9
2.2.1 Regions in the HAZ .....	9
2.2.2 CGHAZ.....	11
2.2.3 ICCGHAZ .....	11
2.2.4 M-A constituents.....	11
2.2.5 Weld simulation .....	13
2.3 Fracture .....	14
2.3.1 Ductile fracture.....	14
2.3.2 Cleavage fracture .....	14
2.3.3 Intergranular fracture.....	16
2.3.4 Fracture mechanics .....	16
2.3.5 Scatter in cleavage fracture toughness.....	16
2.3.6 Ductile-to-brittle transition .....	17
2.3.7 Fractography .....	18
2.4 Crack initiation.....	18

2.4.1	Initiation by M-A constituents .....	19
2.4.2	Initiation by inclusions.....	20
2.4.3	Strain induced initiation .....	21
2.4.3	Location of crack .....	21
2.5	Crack propagation and arrest.....	22
2.5.1	Multiple barrier model .....	22
2.5.2	Microstructural aspects to crack propagation and arrest .....	23
2.6	Acoustic emission .....	24
2.7	Previous results from Artic Materials I using AE .....	25
2.7.1	Quantitative relation between acoustic emission signal amplitude and arrested microcrack size .....	25
2.7.2	Monitoring of cleavage microcrack arrest in weld thermal simulated microstructures by means of acoustic emission .....	28
3.	Material .....	30
3.1	Base plate properties .....	30
3.2	Weld simulation properties.....	30
3.3	Microstructure examination .....	32
3.4	Vickers hardness measurements .....	32
4.	Experimental methods .....	33
4.1	Fracture mechanic testing with Acoustic emission.....	33
4.1.1	Test set-up and sample preparation .....	33
4.1.2	Test program .....	34
4.2	Microstructural characterization .....	35
4.2.1	Microstructure in HAZ.....	35
4.2.2	Microstructure in base material.....	36
4.2.3	Grain size determination.....	36
4.2.4	Vickers Hardness measurements .....	36
4.3	Fracture surface characterization .....	36
4.3.1	SEM analysis .....	36
4.3.2	EDS analysis .....	36
5.	Results .....	38
5.1	Microstructure .....	38



5.1.2 M-A phases.....	42
5.1.3 Vickers hardness.....	45
5.2 Fracture toughness and AE signals.....	45
5.2.1 Size of the arrested microcrack.....	47
5.2.2 Shape of AE signal .....	48
5.3 Fractured samples (run to final fracture).....	49
5.4 Interrupted samples.....	53
5.4.1 Correlation between AE amplitude and arrested microcrack .....	61
5.4.2 Crack initiation .....	62
5.4.3 Inclusions.....	64
5.4.4 EDS analysis .....	67
5.4.5 Shape of AE signals.....	68
6. Discussion .....	70
6.1 Microstructure .....	70
6.1.1 Base material and intergranular fracture.....	71
6.1.2 M-A phases.....	71
6.2 Flat areas on the fracture surface .....	72
6.3 Crack initiation.....	73
6.4 Crack propagation .....	73
6.4.1 AE signals and barriers to crack propagation.....	73
6.4.2 Arrested microcrack size .....	74
6.4.3 Source of AE signal .....	74
6.4.4 Multiple barrier model .....	75
6.5 Comparing the results to AM I .....	75
6.6 AE signal amplitude vs arrested cleavage microcrack size .....	75
6.7 Suggestion for further work .....	76
7. Conclusion .....	77
8. References.....	78
9. Appendices .....	81
9.1 Tables from testing.....	81
9.2 Micrographs .....	85
9.3 Fractographs.....	89

9.4 Risk assessment..... 94

## 1. INTRODUCTION

It is estimated that around 30 % of the world's undiscovered gas resources and 13 % of the undiscovered oil reserves are located in the arctic region. Exploration and extraction of oil and gas in this region is therefore of great interest. However, this is challenging due to the harsh climatic conditions. For materials, the most critical condition is the low temperatures, reaching as low as - 60°C. (Akselsen, 2014b, Akselsen, 2014c)

The problem with low temperatures is materials getting brittle. HSLA (High Strength Low Alloy) steels are usually used for construction at low temperatures due to their good combination of strength and toughness; with a ductile-to-brittle transition temperature as low as - 70 °C. The problem arises when these steels are welded, resulting in a drastic decrease in toughness. This is due to the change in microstructure in the heat-affected zone (HAZ) caused by the heat from the welding process. (Bhadeshia and Honeycombe, 2006)

In order to develop materials with better weldability, there is a need for a better understanding of brittle fracture mechanisms of different weld microstructures. The Artic Materials (AM) project addresses this problem. This is a collaborative project between SINTEF, NTNU and several industrial companies. The overall objective is to establish criteria and solutions for safe and cost-effective application of materials for hydrocarbon exploration and production in arctic regions. The project is divided into AM I (2008-2013), and AM II (2013-2017). (SINTEF, 2010)

As a part of the AM project, Østby et al. (2012) made use of the Acoustic Emission (AE) emitted when a microcrack nucleate in steel, in order to investigate the micromechanisms happening during brittle fracture. They established a quantitative relation between acoustic emission signal amplitude and arrested cleavage microcrack size. This lay the basis for this thesis. There is a need more data confirming this relation, especially in regards to different steels.

Investigation of the arrested cleavage microcrack size is important in order to determine microstructural barriers to crack propagation. This can be used to produce steels with better low temperature toughness, and as input to modeling the expected fracture toughness of materials at different temperatures. Recent theoretical models for brittle fracture, like the multiple-barrier model (Lambert-Perlade et al., 2004a), bases the failure criteria on the probability for initiation times the probability of propagation through several barriers.

In order to further develop these models, there is a need for more quantitative input. This thesis investigate how a 420 MPa rolled steel plate with very low carbon content behaves in regards to the multiple-barrier model and to the relation between the AE signal amplitude and the arrested microcrack size established by Østby et al. (2012).

The thesis is written in cooperation with Andreas Vrenne Larsen. He did a pre-master project on this topic and continues the work in his master thesis. This thesis focuses more on the microstructure and its relation to initiation and propagation in brittle fracture, while he

focuses on AE in regards to the equipment, sorting and analysis of the results obtained from fracture mechanic testing using AE measurement. This thesis will therefore just give a short introduction to the AE, with the necessary information needed to use this approach in characterizing the brittle fracture micromechanisms for this steel. The result concerning AE data and fracture toughness from Larsen's project work will be added in the result section of this thesis.

The work carried out in this thesis is microstructural analysis of the steel and fracture surface investigation. The fracture surface investigation covers a screening of specimens run to fracture and a detailed analysis of specimens interrupted in fracture mechanic testing when the first AE signal corresponding to a microcrack nucleation was detected. This is the method in which Østby et al. (2012) developed the relation between AE signal amplitude and size of the arrested microcrack. More information of this will be given in the following chapter.

## 2. THEORETICAL BACKGROUND

*This chapter present the necessary theoretical background and research carried out on brittle fracture initiation and propagation. There will also be a presentation of Østby et al. (2012) paper, and a summarize of the result from a follow up paper by Østby et al. (2013), for comparison with the steel investigated in this thesis.*

### 2.1 MICROSTRUCTURES

*The microstructure in metal alloys depends on alloying elements present, their concentrations and the heat treatment (Callister and Rethwisch, 2011). In this chapter, the main relevant microstructures for the steel used in this thesis will be presented together with techniques for revealing the microstructure. In addition, Thermo-mechanically controlled processing (TMCP) will be presented.*

#### 2.1.1 EQUILIBRIUM PHASES OF STEEL

The equilibrium phases of steel are presented in a phase diagram, which illustrate different microstructures obtained with varying carbon content and temperature. Austenite ( $\gamma$ ) is the equilibrium phase at high temperatures, while ferrite ( $\alpha$ ) and cementite ( $\text{Fe}_3\text{C}$ ) is the equilibrium phases at low temperatures (cementite is strictly speaking metastable, but it is stable for all practical purposes). (Callister and Rethwisch, 2011)

Austenite can dissolve up to 2.14 wt% carbon, while the solubility of carbon is 0.022 wt% in ferrite. This is explained by the crystal structure, with austenite a having FCC structure with larger interstitial positions than ferrite with a BCC structure. After the solubility limit cementite is formed, which is hard and brittle. (Callister and Rethwisch, 2011)

Figure 1 illustrate the phase diagram and microstructures at a carbon content between 0.022 and 0.76 wt%. This composition is less than the eutectoid composition and is termed hypoeutectoid. At the eutectoid composition, pearlite is formed during slow cooling from austenite. Pearlite is a microstructure consisting of alternating layers of ferrite and cementite. For steels with a carbon content less than this, proeutectoid ferrite is formed in addition to pearlite, as illustrated in the figure. This is the case for HSLA steel, which has a carbon content less than 0.1 wt% (Solberg, 2007).

In the phase diagram, the temperature in which austenite transform to ferrite upon cooling, i.e. the line between austenite and the two-phase area of austenite and ferrite, is termed  $A_3$ . Upon further cooling, at the temperature in which austenite and ferrite is transformed to ferrite and cementite, the term is  $A_1$ . These temperatures are dependent of the alloying elements.(Bhadeshia and Honeycombe, 2006)

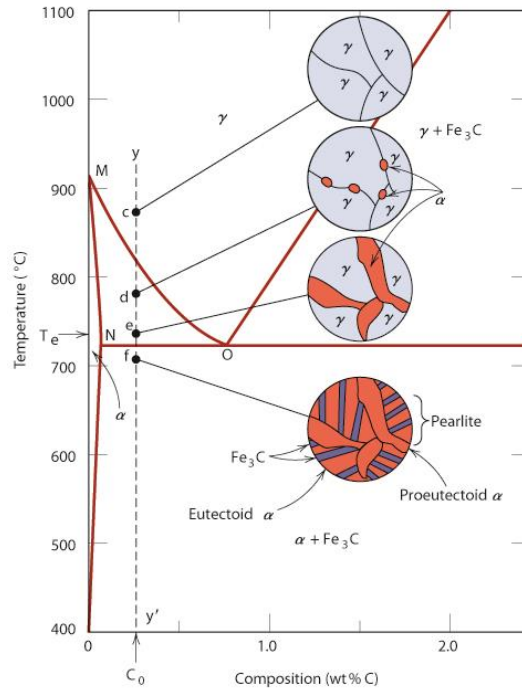


Figure 1 – Schematic representation of the microstructures for an iron-carbon alloy of hypoeutectoid composition (Callister and Rethwisch, 2011)

### 2.1.2 BAINITE

Bainite is formed at a temperature range between the pearlite and martensite transformation. This can be illustrated in a continuous cooling transformation (CCT) diagram shown in Figure 2. This also illustrate the cooling rate needed to produce bainite for the given alloy composition.

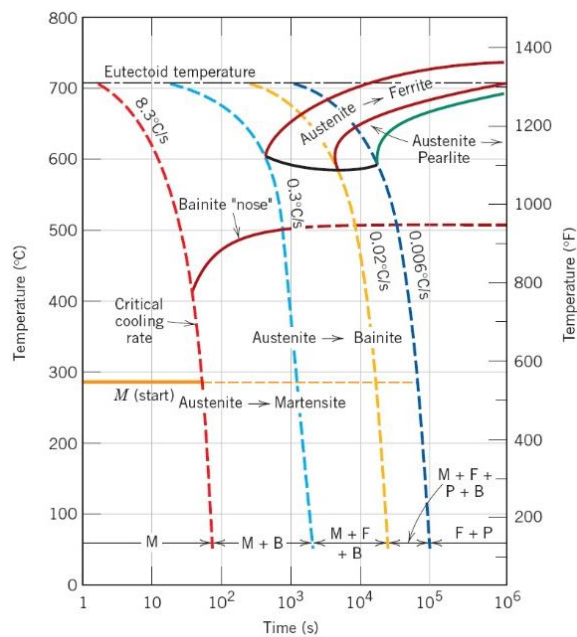


Figure 2 – CCT diagram for an iron-carbon alloy (Callister and Rethwisch, 2011)

The bainitic microstructure consist of ferrite and carbides in a needle like shape. It is formed as packets of ferrite grown from the austenite grain boundaries with carbides precipitated between the ferrite plates. Bainite is commonly divided into two broad categories; upper and lower bainite. Upper bainite is formed at higher temperatures, where the carbon from the ferrite transformation is allowed to diffuse into austenite and carbide precipitates between the ferrite plates. At low temperatures, carbon diffusion is slower and incomplete, leading to the precipitation of carbides in both the interlath region and in the ferrite lath interior. This is illustrated in Figure 3. Lower bainite has both a higher strength and toughness than upper bainite, as the overall morphology is much finer. (Vander Voort, 2004)

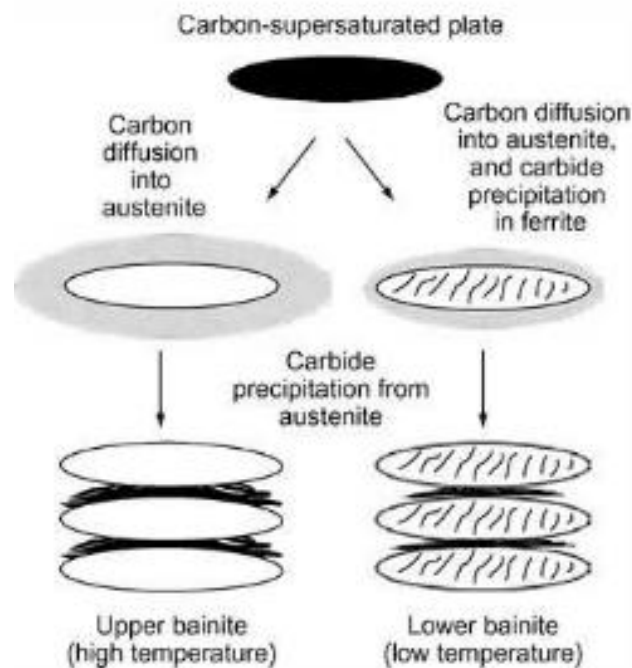


Figure 3 – Development of upper and lower bainite (Vander Voort, 2004)

### 2.1.3 MARTENSITE

Martensite is formed when austenite is cooled rapid enough to prevent carbon diffusion. The rapid cooling leads to a plate- or needle like appearance, making martensite hard, strong and brittle. The amount of martensite depends on the degree of under cooling below the transformation start temperature  $M_s$ . The transformation ends at a temperature  $M_f$ , which is often defined as the temperature where the fraction of martensite equals 95%. The  $M_s$  and  $M_f$  temperatures are independent of cooling rate and are characteristic for a given alloy. Figure 4 illustrate the effect of carbon on  $M_f$  and  $M_s$ . The effect of alloying elements on  $M_s$  are given in equation 1. (Bhadeshia and Honeycombe, 2006)

$$M_s = 539 - 423(\%C) - 30.4(\%Mn) - 17.7(\%Ni) - 12.1(\%Cr) - 7.5(\%Mo) \quad (1)$$

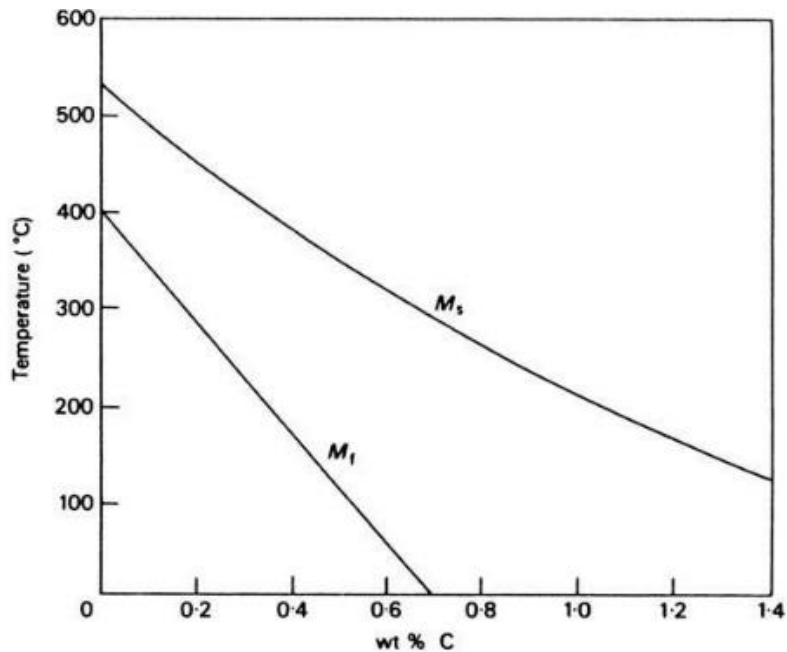


Figure 4 – The effect of carbon on  $M_s$  and  $M_f$  (Bhadeshia and Honeycombe, 2006)

Martensite is very strong, but also very brittle. Tempering is often conducted to regain ductility. This is accomplished by heating a martensitic steel to a temperature below the eutectoid for a specified time period. Thus, the carbon are allowed to diffuse, and the result is a dispersion of coarse carbides in a ferritic matrix. If  $M_s$  are high, the first formed martensite can be auto-tempered in the remainder of the quench. (Bhadeshia and Honeycombe, 2006)

#### 2.1.4 ETCHING

Etching is a process of controlled corrosion. Every microstructural constituent within a metal has a different surface electrochemical potential and thus different corrosion behavior. Constitutes that are more electropositive are attacked more easily than those who are more electronegative. This will expose defects such as grain boundaries and bring out the contrast between different phases or different crystallographic orientations that etch at different rates. (Bramfitt and Benscoter, 2001)

##### 2.1.4.1 NITAL

Different etchants are used to revile different constituents. To reveal ferrite grain boundaries, nital is commonly used. Nital reveal ferrite grains, martensite and bainite by attacking the ferrite grains and grain boundaries to produce “relief” on the specimen surface. Nital does not attack carbides but enhances the interface between the carbide and the matrix. It is a mixture of nitric acid and ethanol, with 2 % being the common mixing ratio, i.e. 2 mL nitric acid and 98 mL ethanol. (Bramfitt and Benscoter, 2001)

##### 2.1.4.2 LEPERA

LePera etchant is a mixture of 1% aqueous solution of sodium metabisulfite ( $\text{Na}_2\text{S}_2\text{O}_2$ ) and 4% picric acid ( $\text{C}_6\text{H}_2(\text{NO}_2)_3\text{OH}$ ) in ethyl alcohol in a 1:1 ratio (LePera, 1979). It is used to reveal M-



A phases, leaving them white in contrast to ferrite which appears tan and with grain boundaries not strongly etched. This is illustrated in Figure 9 and Figure 10 (in M-A chapter).

#### 2.1.5 GRAIN SIZE DETERMINATION

In the ASTM standard “standard test methods for determining average grain size” (2014), it’s described three manual basic procedures to determine the average grain size:

- *Comparison procedure*: Involves comparison of the grain structure to a series of graded images.
- *Planimetric procedure*: Involves a count of the number of grains within a known area.
- *Intercept Procedure*: Involves a count of the number of grains intercepted by a test line or the number of grain boundary intersections with a test line, per unit length of test line.

In this thesis, given limited need for exact grain size measurements and the amount of time it would take, these methods will not be used and are therefore not explained further. Another possible way of measuring grain size is automatically, which also won’t be explored any further. In a rolled product, the transverse section is commonly used to measure grain size (Bramfitt and Benscoter, 2001).

#### 2.1.6 HARDNESS MEASUREMENTS

Hardness is a material’s resistance to localized plastic deformation, e.g. a small dent or a scratch. Measurements is done by applying force from a small indenter on the material to be tested, under controlled conditions of load and rate. The depth or size of the resulting indentation is measured, which in turn is related to a hardness number. Softer materials will exhibit a larger and deeper indentation, with a corresponding lower hardness index number. Vickers hardness testing is used for small specimens, and the surface should be grinded and polished for accurate measurement. Hardness testing can help identify the microstructure, as they have a more or less distinct hardness. (Callister and Rethwisch, 2011)

Fairchild et al. (2000) tested the Vickers hardness for a steels somewhat similar to the steel investigated in this thesis, which will be used in discussing of the microstructure. The results are seen in Figure 5. The different Gleeble numbers are for different weld simulated cooling times resulting in different microstructures. Gleeble 1 gives a microstructure of mostly upper bainite with around 25 % martensite. The increasing cooling times for Gleeble 2 and 3 gave no martensite, and a coarser structure.

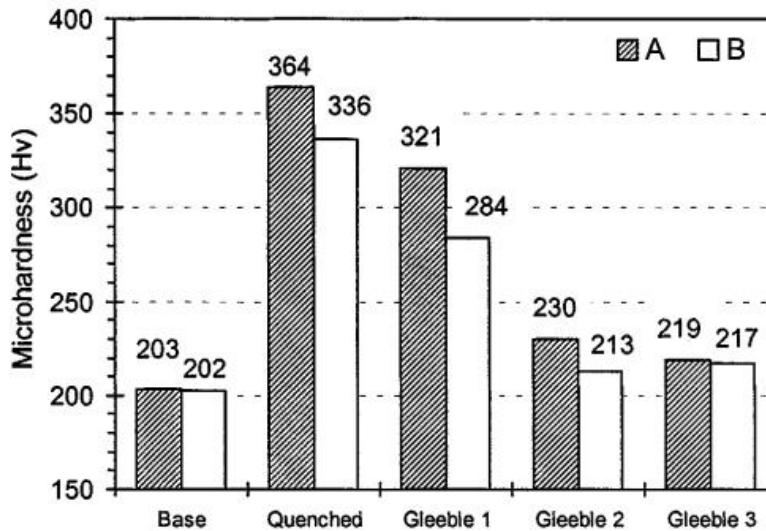


Figure 5 – Micro-hardness (HV) result for weld simulated steel. The different Gleeble numbers are different cooling times resulting in different microstructures.

#### 2.1.7 THERMO-MECHANICALLY CONTROLLED PROCESSING (TMCP)

The only information given about the production method for the steel plates used in this thesis is that they are produced with thermomechanical rolling and accelerated cooling, i.e. TMCP. This is how HSLA get their strength, in addition to adding specific alloying elements (Solberg, 2007). Findings on the fracture surface of the investigated steel, led to an exploration off the rolling process for possibly explaining the findings. Thus, following is a summarize of different methods of the TMCP, as described by Solberg (2007).

The advantage of TMCP is that it produces a fine-grained structure, which is beneficial to strength and toughness. First, the steel is heated to around 1200 °C to precipitate coarse carbon nitrides. Following is a significant deformation through several coarse rolling steps while the temperature decreases to around 950 °C. The repeatedly rolling and carbon nitrides precipitating on the deformation structure restricts grain growth, thus produces grain refining after each rolling step.

After around 950 °C different variants of controlled rolling is possible resulting in different microstructures as illustrated in Figure 6. A simple version (A in the figure) is just to cool the steel after the coarse rolling resulting in a fine grained ferrite with a grain size of about 15-20 μm, with carbon nitrides precipitated in the ferrite.

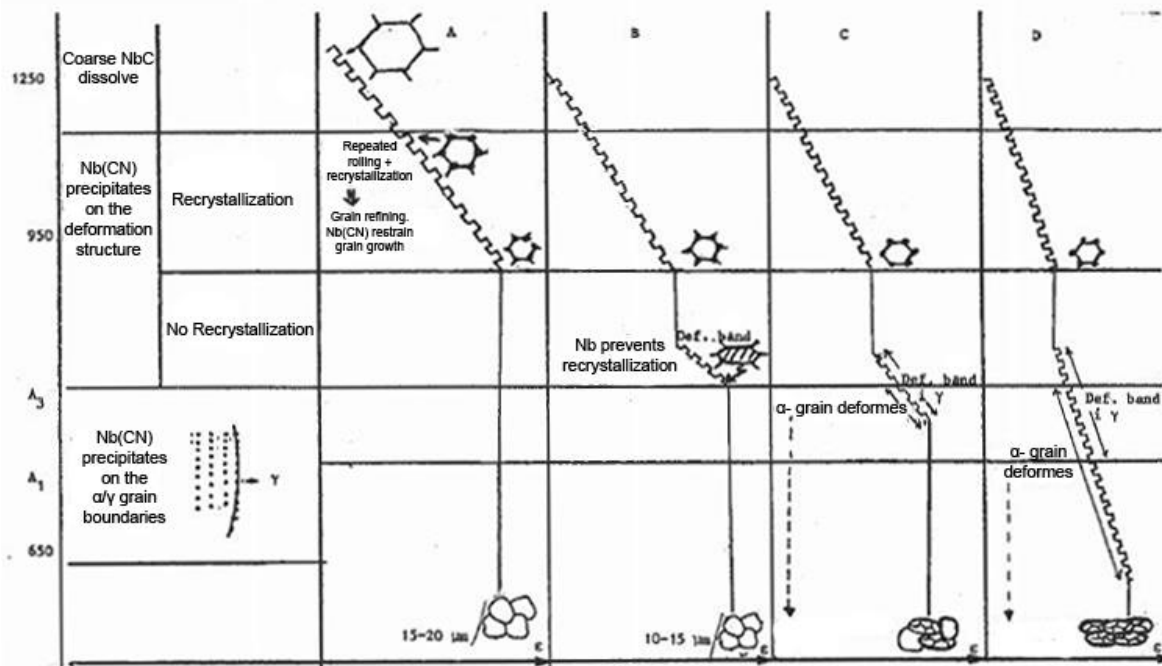


Figure 6 - Four different varieties of controlled rolling of micro-alloyed steel, adapted from (Solberg, 2007)

Another version is to perform fine rolling from 950 °C to  $A_3$  (B in the figure). In this temperature range there is no recrystallization due to the alloying elements, with niobium as the biggest contributor. This results in flat austenite grains with a high grain boundary area, and deformation bands going through the grains. Cooling under  $A_3$  leads to ferrite nucleating on both the deformation bands and the grain boundaries, leaving a ferrite grain size at around 10-15  $\mu\text{m}$ . The gap where no rolling is conducted in the figure is due to being the temperature range in which austenite partly recrystallize. There should be no rolling here because it could lead to a few big austenite grains. Version C and D in the figure is the same as in B, except for rolling over a longer temperature range leaving a structure as seen in the figure. The grain size can be further reduced by accelerated cooling.

## 2.2 MICROSTRUCTURES IN THE HAZ

*During welding, the microstructure in the heat-affected zone (HAZ) changes, resulting in a drastic decrease in toughness. This is the region close to the weld, where the heat input during welding changes the microstructure without melting the steel. The risk of developing cracks is highest in this region of the weld (Arntsen, 2000). This chapter presents the different regions in the HAZ and the M-A phases developed there, which are believed to be one of the biggest contributor to the decrease in toughness.*

### 2.2.1 REGIONS IN THE HAZ

The HAZ is divided into four main regions, given by the distance away from the fusion boundary; subcritical HAZ (SGHAZ), intercritical HAZ (ICHAZ), fine grained HAZ (FGHAZ) and coarse grained HAZ (CGHAZ). These regions exhibits different microstructures due to reaching different peak temperatures,  $T_p$ , from the welding process, illustrated in Figure 7 (a) and Figure

8. The cooling rate is less sensitive to the distance from the fusion boundary, and can be stated as the time,  $\Delta t_{8-5}$ , taken to cool over the temperature range 800-500 °C (Bhadeshia and Honeycombe, 2006). For simplification in this thesis, the  $\Delta t_{8-5}$  will be written after stating the microstructure. For example, CGHAZ 15 is the same as a CGHAZ microstructure with a  $\Delta t_{8-5}$  of 15 seconds.

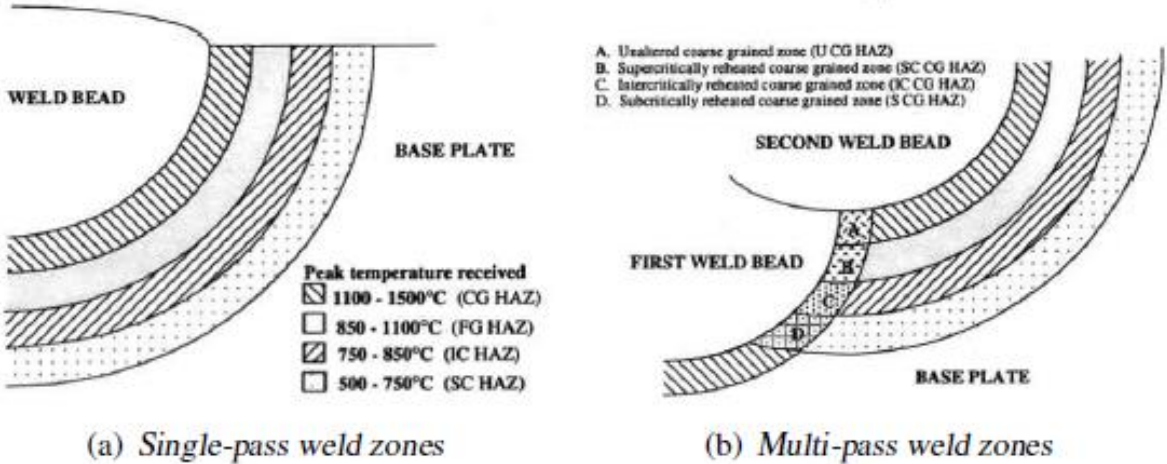


Figure 7 – Schematic diagram of the HAZ: (a) single pass-weld, and (B) multi-pass weld (Davis and King, 1994)

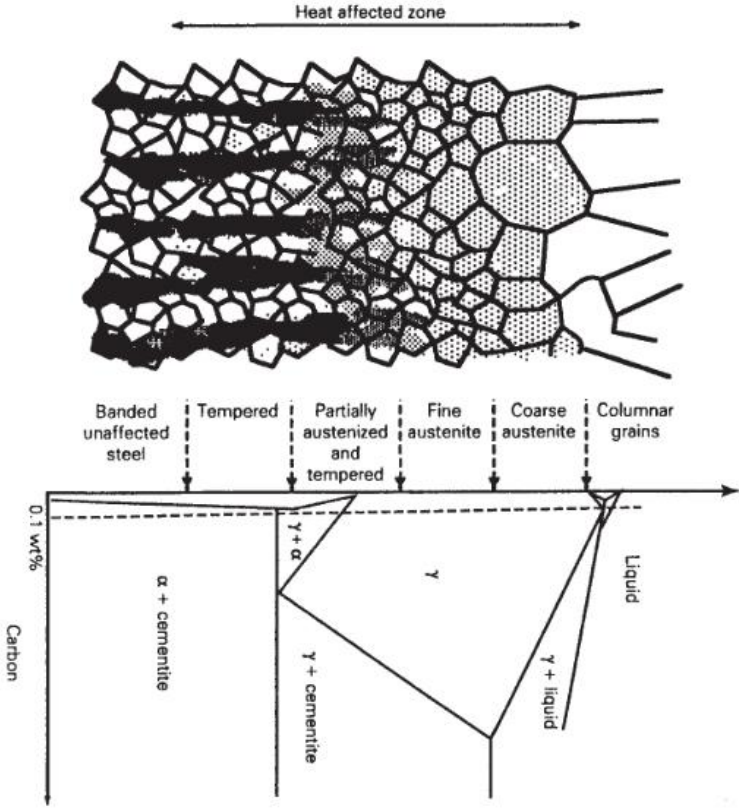


Figure 8 - Schematic illustration of the microstructural variation to be expected in the HAZ of steel welds (Bhadeshia and Honeycombe, 2006)

### 2.2.2 CGHAZ

The region closest to the weld bead, CGHAZ, is the most critical zone in regards to loss in toughness. Here, the temperature is way beyond  $A_3$ , resulting in large grained austenite giving unfavorable microstructures upon cooling, such as coarse ferrite side plates (like upper bainite). In addition, if some austenite is retained after the bainite transformation, martensite–austenite (M–A) constituents can be formed, which further decreases toughness. These are formed in the last stage in the transformation process by ferrite growing in contact with each other, leaving untransformed austenite regions among them. The M–A constituents may be located between bainitic laths as well as at prior austenite grain boundaries. (Mohseni et al., 2014, Lambert-Perlade et al., 2004b, Cuixin et al., 2008)

### 2.2.3 ICCGHAZ

During multi-pass welding, the HAZ formed by the first heating cycle is modified by the subsequent thermal cycles. Reheating CGHAZ into the mixed austenite and ferrite region in the phase diagram gives an intercritically reheated CGHAZ (ICCGHAZ) microstructure, as seen in Figure 7 (b). Heating to this region transforms part of the microstructure into austenite. Depending on the prior CGHAZ, the austenite nucleates and grow along the prior austenite grain boundaries, bainite lath boundaries or at carbides. These austenite areas (islands) becomes enriched in carbon due to austenite having a higher solubility than ferrite, and transforms to hard and brittle M-A constituents upon cooling. For a CGHAZ of upper bainite with a large prior austenite grain size, a necklace type of M-A distribution along prior austenite grain boundaries is expected in the ICCGHAZ. This region have been found to demonstrate an even lower toughness than CGHAZ, and the most important reason for this is believed to be the formation these M-A constituents. (Davis and King, 1994, Moeinifar et al., 2010)

For a bainitic CGHAZ, reheating also reduces the size of the bainitic ferrite, which transforms partially into mixed bainite and ferrite. (Yokoyama and Nagumo, 1998)

### 2.2.4 M-A CONSTITUENTS

M-A constituents are formed as described in the previous sub-chapters. According to Davis and King (1994), they appear in two distinct morphologies:

- (1) Blocky particles of the order of 3 to 5  $\mu\text{m}$  in diameter that form at the prior austenite grain boundaries.
- (2) Elongated stringer-type particles that develop between bainite/martensite laths, approximately 0.2 to 1  $\mu\text{m}$  in width and several microns in length.

Mohseni et al. (2014) found these blocky particles when using LePera etchant on API X80 pipeline (HSLA) steel weld simulated to get an ICCGHAZ microstructure. This is shown in Figure 9, with arrows indicating M-A particles. Arrow 1 and 2 indicates M-A particles on the prior austenite grain boundary, while arrow 3 indicates an intergranular M-A particle. They also found elongated M-A stringers, shown in Figure 10. Their investigation concluded that the

formation of M–A constituents along prior austenite grain boundaries was one of the most important reasons for the loss in ICCGHAZ toughness after welding of HSLA steels.

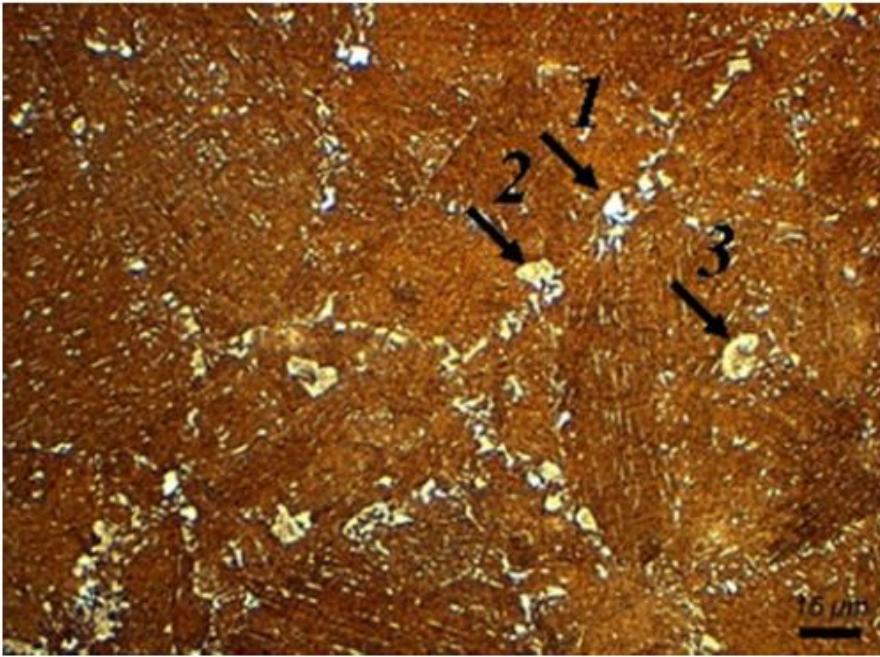


Figure 9 – Micrograph of the ICCGHAZ, M-A constituents indicated by arrows, using LePera etchant (Mohseni et al., 2014)

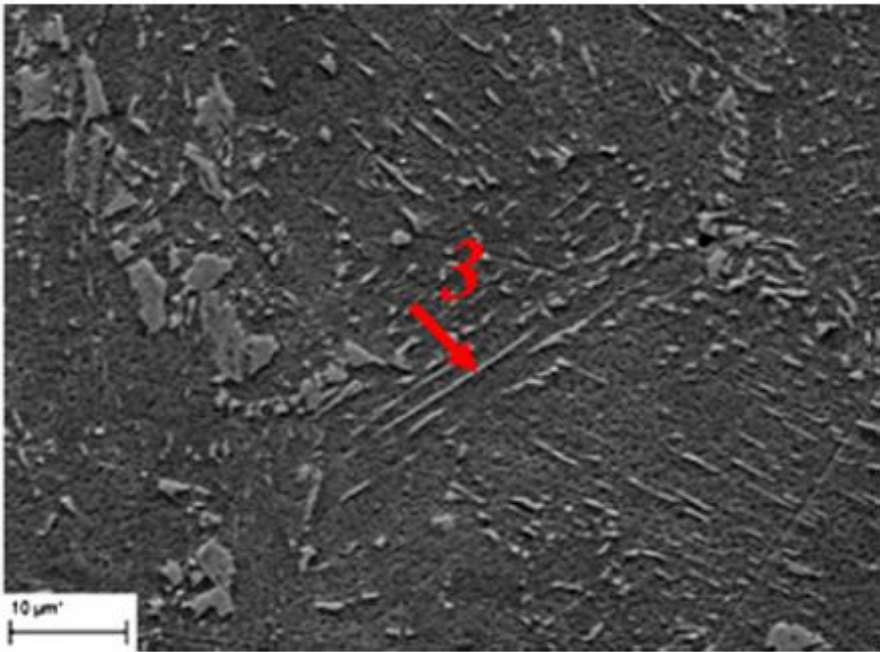


Figure 10 – SEM micrograph of the ICCGHAZ, stringer M-A constituent indicated by the arrow (Mohseni et al., 2014)

For CGHAZ, Cuixin et al. (2008) concluded that M-A constituent was not the main influencing factor in the decrease of toughness, due to the M-A constituents in CGHAZ having a smaller



size and area fraction than for ICCGHAZ. In addition, residual austenite in M-A islands is a favorable phase because it can reduce stresses in the crack tip and consume expansion energy.

It has been shown that small austenite islands (< 1 μm in diameter) formed during the second thermal cycle remain as austenite even following fast cooling, and the amount of retained austenite in the M-A particles decreases as the M-A particle size increases. (Davis and King, 1994)

M-A constituents can be characterized by its maximum length,  $L_{max}$ , and the aspect ratio,  $L_{max}/L_{min}$  (minimum length). Bonnevie et al. (2004) classified particles larger than 2 μm as large particles and an particles with an aspect ratio of more than 4 as elongated stringer particles. The morphology of the M-A phases for CGHAZ and ICCGHAZ found in their research are summarized in Figure 11. As seen, the M-A phases in ICCGHAZ is bigger than for CGHAZ. This could explain why ICCGHAZ is more brittle than CGHAZ.

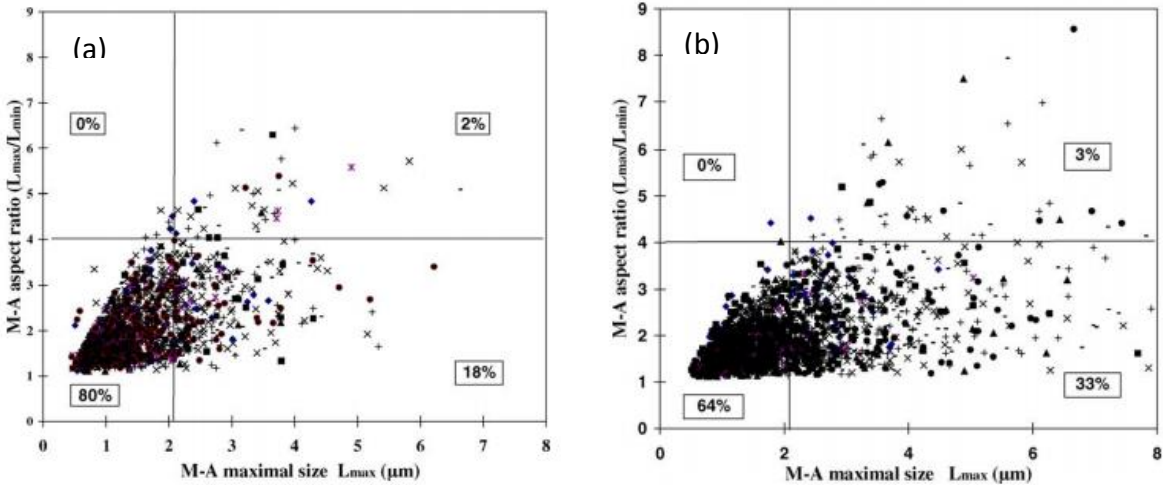


Figure 11 – Morphology of M-A constituents in (a) CGHAZ 30 and (b) ICCGHAZ 30

The formation of M-A phases have been found to be affected by the cooling rate. Cuixin et al. (2008) found the maximum area fraction of M-A phases with a cooling rate,  $\Delta t_{8-5}$ , of 7 seconds with decreasing M-A fraction with further increase of cooling time. The steel investigated was HSLA with 0.059 wt% carbon, and CGHAZ weld simulated. Lan et al. (2011) found the maximum volume fraction of M-A phases in CGHAZ for low carbon bainitic steel with 0.06 wt% carbon to increase with increasing cooling rate, and the corresponding morphology going from small dot-shaped particles to larger elongated block-shaped particles.

2.2.5 WELD SIMULATION

Weld simulation is used to simulate the HAZ and is conducted by heating a specimen with a thermo-element. More information about this process can be found in literature and in Larsen (2014) project work. Weld simulation allows detail control of the heating and cooling, and have been shown to simulate HAZ with the same toughness ranking as those on actual weld HAZ. Simulation tests are therefore an economical and reproducible method of analyzing the

microstructure and micromechanisms of failure in any individual HAZ region (Moeinifar et al., 2010).

## 2.3 FRACTURE

*In metals, there are two possible fracture modes: ductile and brittle. The classification is based on the ability for the metal to experience plastic deformation. Fracture can, however, also occur from fatigue and creep (Callister and Rethwisch, 2011). This chapter gives a short presentation to the mechanisms and fractographic appearance of these fracture modes. Following is some more short presentations, including fracture mechanics, scatter in cleavage fracture toughness, the ductile-to-brittle transition and methods in fractography.*

### 2.3.1 DUCTILE FRACTURE

In ductile fracture, extensive plastic deformation takes place before failure. Ductile materials usually fail as a result of nucleation, growth and the coalescence of microscopic voids that initiate at inclusions and second-phase particles. Figure 12 (a) illustrate this. The fracture surface for ductile fracture is characterized by dimples formed after microvoid coalescence. Ductile materials exhibits a longer stretching zone than brittle materials. This zone is formed as a result of blunting and stretching at a crack tip. In fracture mechanic testing, this can be seen after the pre-test fatigue notch as a smooth surface. (Anderson, 2005, Weidner et al., 2013)

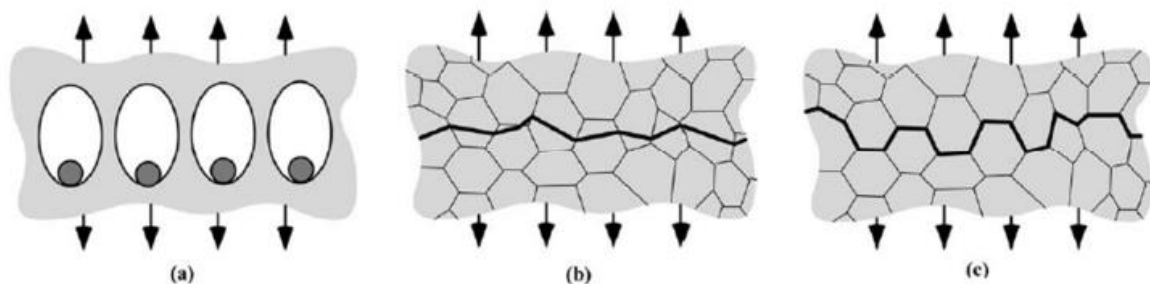


*Figure 12 –Micromechanisms of fracture in metals: (a) ductile fracture, (b) cleavage, and (c) intergranular fracture (Anderson, 2005)*

### 2.3.2 CLEAVAGE FRACTURE

For most brittle crystalline materials, crack propagates rapid by cleavage, i.e. successive and repeated breaking of atomic bonds along specific crystallographic planes. This is termed transgranular fracture, as the fracture pass through the grains, illustrated in Figure 12 (b). The preferred cleavage planes are those with the lowest packing density, since fewer bonds must be broken and the spacing between planes is greater. Each time the crack crosses a grain boundary it changes direction when seeking the most favorably orientated plane. The nominal orientation of the cleavage crack is perpendicular to the maximum principal stress. (Anderson, 2005)



Cleavage is most likely to occur when the plastic flow is restricted, i.e. when the number of slip systems are limited. At low temperatures the number of active slip systems in BCC metals (e.g. ferrite) decreases, causing cleavage fracture. (Anderson, 2005)

In order for cleavage to initiate, there must be a local discontinuity (e.g. a second phase particle) ahead of a macroscopic crack, creating a local stress sufficient to exceed the bond strength. This also creates a local strain in the matrix that initiate a crack in the second phase particle, illustrated in Figure 13. If the stress ahead of the macroscopic crack is sufficient, the microcrack propagates into the ferrite matrix, causing failure by cleavage. (Anderson, 2005)

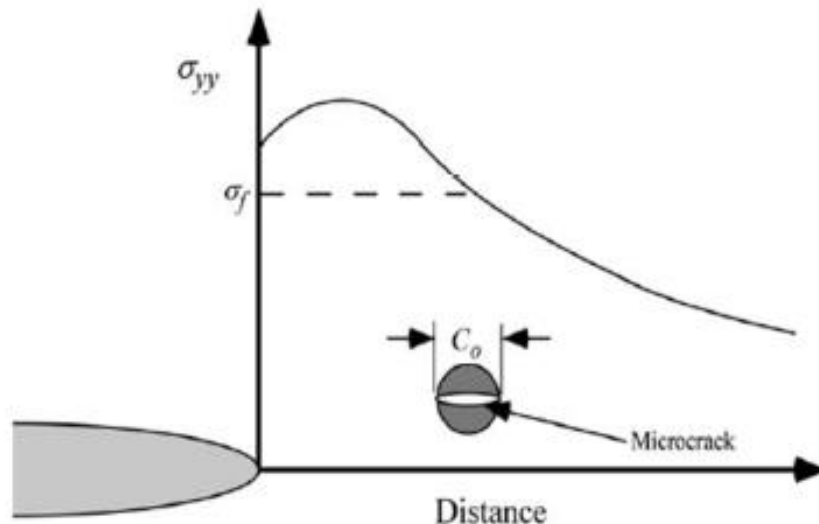
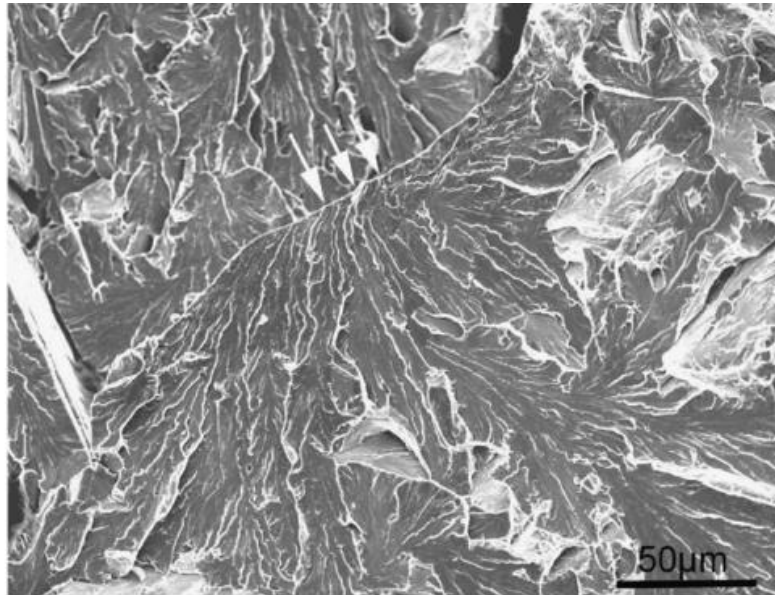


Figure 13 – Initiation of cleavage at a microcrack that forms in a second-phase particle ahead of a macroscopic crack (Anderson, 2005)

The fracture surface appearance of cleavage fracture has typically multiple flat facets containing river patterns. These patterns are formed when a propagating crack forms on several parallel planes, and when crack encounters a grain boundary with a different orientation. As the multiple cracks propagates, they are joined by tearing between planes. There is a tendency for multiple cracks to convert into a single crack because this consumes less energy. (Anderson, 2005)

The size of the facets could give an indication of the propagation energy. If the facets are large, the crack propagated easily. Figure 14 shows a large cleavage facet, in which the crack propagated across a prior austenite grain in a straight way. (Lan et al., 2011)



*Figure 14 – Cleavage facets, arrows indicating crack initiation (Lan et al., 2011)*

### 2.3.3 INTERGRANULAR FRACTURE

In a few cases, fracture can occur along grain boundaries, known as intergranular fracture. This is illustrated in Figure 12 (c). Several possible situations can cause this type of fracture, including precipitation of a brittle phase on the grain boundary, environmental assisted cracking, intergranular corrosion and grain boundary cavitation and cracking at high temperatures. (Anderson, 2005)

Relevant to the fracture mechanic testing of the steel in this thesis only brittle phases on the grain boundary is a possibility. This can be caused by improper tempering. Tempering near 350 °C can result in tempered martensite embrittlement, and tempering near 550 °C can result in tempering embrittlement. Both involve the segregation of impurities such as phosphorous and sulfur, to prior austenite grain boundaries. (Anderson, 2005)

### 2.3.4 FRACTURE MECHANICS

Fracture mechanics is the assessment of the material integrity for flawed mechanical structures. Two types of approaches have been developed for this purpose; the global and local approach. The global approach is essentially based on linear elastic fracture mechanics (LEFM) and elastic plastic fracture mechanics (EPFM). These approaches assumes that the fracture resistance can be measured in terms of a single parameter, such as  $K_{IC}$ ,  $J$  and  $CTOD$ . The local approach to fracture (LAF) bases modeling of fracture toughness on a local fracture criteria at every location of a loaded component, in order to derive a failure criterion for this component using a weakest-link assumption. More information of these approaches can be found in literature. (Pineau, 2007, Lambert-Perlade et al., 2004a)

### 2.3.5 SCATTER IN CLEAVAGE FRACTURE TOUGHNESS

Zhang and Knott (1999) investigated the scatter in cleavage fracture toughness by looking at the fracture behavior in bainite, auto-tempered martensite and a mixture of the two

microstructures. They found considerably more scatter for the mixed microstructure than for the single-phase microstructures, with values for the mixed microstructure spreading widely between those for the single bainite and single martensite. This is most likely because the cleavage fracture toughness depends on the phase in which the cleavage fracture first initiated in. The auto-tempered martensite had a notable higher toughness than bainite.

Another explanation for the scatter in cleavage fracture toughness is due to the location of the fracture-triggering particle. Two nominal identical specimens made of the same material may display vastly different toughness values because the location of the critical fracture-triggering particle is random. (Anderson, 2005)

Østby et al. (2011) investigated the cleavage scatter in weld simulated samples fracture mechanic tested at low temperatures. The CGHAZ and ICCGHAZ simulated samples had similar values in the lower range, however, the scatter and the average values were higher for CGHAZ. Additional information indicated that this could be due to ICCGHAZ simulated samples commonly initiating from large blocky M-A constituents, which was not found to be present in the CGHAZ. Brandt et al. (2012) also found more scatter in CGHAZ compared to ICCGHAZ simulated samples. They came to the same conclusion, with ICCGHAZ initiating from M-A constituents, while the CGHAZ initiating from slag particles that are more scattered than the M-A constituents.

The fracture toughness is dependent on the specimen geometry and mode of loading, i.e. it is not a material parameter. This is often referred to as the so-called constraint effects. It arises due to the fact that varying the defect depth and/or mode of loading will have an influence on the local stress level in front of the crack tip. (Østby et al., 2011)

#### 2.4.6 DUCTILE-TO-BRITTLE TRANSITION

The fracture toughness of ferritic steels can change drastically over a small temperature range, going from ductile at high temperatures to brittle at low temperatures. This is illustrated in Figure 15. In the transition region between ductile and brittle behavior, both micromechanisms of fracture can occur in the same specimen. The transition region is highly scattered due to the mention randomly location of a fracture-triggering particle. It has been found through fracture mechanic testing and studying of the fracture surface in SEM that the distance from the initiation to the original crack tip correlates very well with the measured fracture toughness. The material has higher toughness as the critical particle is further away from the crack tip, i.e. the specimen has to sample more material by ductile tearing before cleavage occurs at the critical particle. (Anderson, 2005)

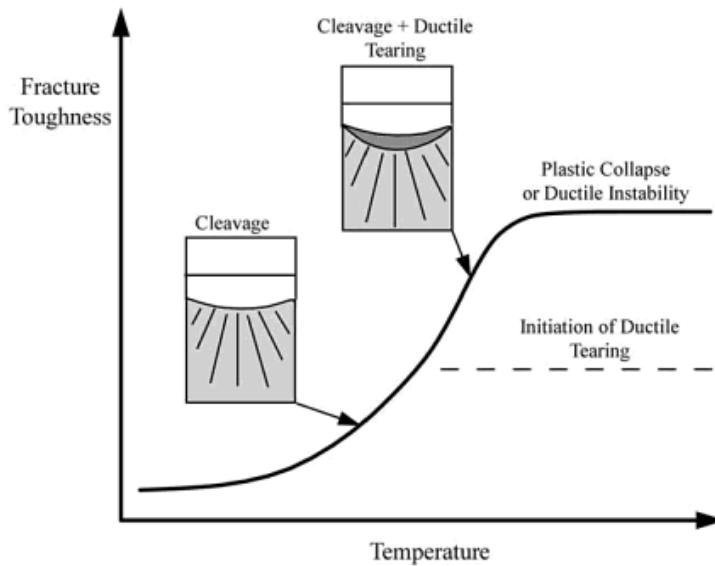


Figure 15 – Ductile-brittle transition in ferritic steel (Anderson, 2005)

### 2.3.7 FRACTOGRAPHY

Fractography is the study of fracture surfaces of materials. A scanning electron microscope (SEM) is preferred for fractographic examination given its good resolution and depth of field (Callister and Rethwisch, 2011).

#### 2.4.7.1 SEM

In SEM, a primary electron beam interacts with the specimen surface to produce secondary electrons, backscattered electrons and x-rays. The backscattered electrons are those electrons that are scattered from the specimen surface, while the secondary electrons are knocked loose from the specimen by the primary electron beam. Secondary electrons are only detected from the surface of the specimen, thus reveal the surface topography. (Bramfitt and Bencoter, 2001)

#### 2.4.7.2 EDS

The chemical elements of an area on the fracture surface can be identified with an EDS (energy dispersive spectroscopy). This collects the X-rays emitted from the specimen due energy release from the atom. If the hole left by the primary electron beam (from SEM) is in the inner shell of the atom, an electron from an outer shell fills it. The outer electron is in a higher energy state, and when it drops to the inner shell, it releases energy through X-rays. The X-rays emitted are characteristic in energy and wavelength for the particular atomic species present and also which shell lost electrons and which shells replaced them. (Bramfitt and Bencoter, 2001)

## 2.4 CRACK INITIATION

*The nature of the microstructural feature that nucleates cleavage depends on the alloy and the heat treatment (Anderson, 2005). This chapter investigates different possible crack initiation mechanisms in cleavage fracture for the HAZ.*

### 2.4.1 INITIATION BY M-A CONSTITUENTS

In the ICCGHAZ, M-A constituents are believed to initiate cleavage. Davis and King (1994) presented four possible mechanisms for initiation associated with M-A constituents, illustrated in Figure 16:

- (1) The M-A constituent is a brittle phase and cracks readily. This microcrack initiates cleavage in the ferrite matrix.
- (2) The austenite to martensite transformation results in a volume expansion that gives a transformation-induced residual tensile stress in the surrounding ferrite matrix. This tensile stress assists cleavage fracture.
- (3) On loading, initially both the matrix and M-A particles will deform elastically and no stress concentration will result as both have the same elastic modulus. However, at a certain point the matrix will begin to deform plastically and shed load into the M-A particles due to the M-A particles being harder than the matrix. This may cause the M-A particles to debond from the matrix as large stresses develop across the interface.
- (4) A microcrack is formed at the boundary between the MA and the ferrite matrix. This microcrack initiates cleavage fracture in the ferrite matrix.

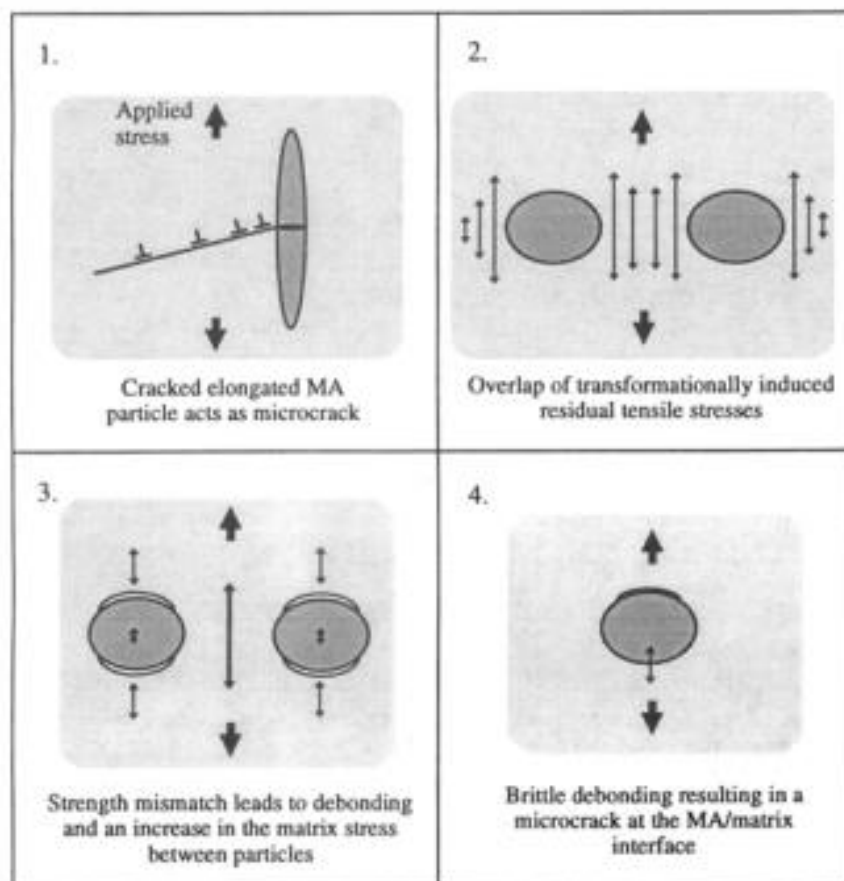


Figure 16 – Schematic representation of the four proposed initiation mechanisms (Davis and King, 1994)

Davis and King (1994) found fracture initiation to occur preferentially between two closely spaced M-A particles that debonded rather than cracked. Thus, suggested the critical mechanism for crack initiation in their investigation to be transformation induced residual tensile stress and debonding. Their investigation also indicated that the significantly drop in toughness in ICCGHAZ is associated with a near-connected grain boundary network of blocky M-A constituent that is harder than the surrounding matrix. In addition, for martensite microstructure with a similar hardness as the M-A phases, cleavage initiation is not associated with M-A particles.

Mohseni et al. (2014) also found brittle cracks to initiate in the ICCGHAZ either by debonding of M-A constituents or in the region between two or more closely separated blocky M-A constituents. This was also the case for Brandt et al. (2012). In addition, they possible found a deboning mechanism to occur by M-A phases forming on de-oxidation particles which facilitated the debonding between the M-A constituents and the matrix. Slag (oxide and sulphide) particles were observed in the ICCGHAZ in Brandt et al. (2012) investigation. However, all the crack initiations were found associated with M-A phases. They concluded that M-A constituents are more potent in triggering cleavage fracture than the slag particles are because no residual transformation stresses are present in the steel matrix around the latter. Besides, sulphidic slag particles are soft and ductile and will not cause high deformation stresses in the surrounding steel matrix.

The size of the M-A constituents are important regarding crack initiation. The M-A particles has to have be sufficiently large to initiate fracture. (Cuixin et al., 2008, Lan et al., 2011).

#### 2.4.2 INITIATION BY INCLUSIONS

Large inclusions are well known to initiate cleavage cracks in welded joints (in addition to the M-A constituents), and studies report a decrease in fracture toughness with an increasing amount of inclusions. This is especially concerning angular inclusions with sharp edges and spherical inclusions that have cavities around them. The cavities are formed by for example sulphide inclusions, which has a higher coefficient of thermal expansion than steel. Hence, upon solidification they shrink much more than the steel leading to the formation of the cavities, which are sites for microcrack nucleation. The possibility of fracture increases with both the size of the cavity and close spacing between them, as microcracks can grow to connect with each other. (Lan et al., 2011, Agboola, 2010)

Oxides are found to initiate fracture by tensile stresses created at the matrix-inclusion interface by oxide having a lower coefficient of thermal expansion than steel. The stress concentration can significantly change the property of the surrounding steel matrix and cause localized plastic deformation. (Agboola, 2010)

Brandt et al. (2012) found both sulfide and oxide slag particles to initiate cleavage by the matrix debonding from these particles in the CGHAZ.

Fairchild et al. (2000) found TiN particles to initiate fracture in CGHAZ, and being responsible for a greater loss in toughness between two steels with similar microstructure and chemical content. The amount of Ti was 0.048 wt% for the steel that exhibited fracture by TiN inclusions, and 0.011 wt % for the steel that showed no sign of initiating from these.

Cracked particle can be found in the steel from the TMCP. The accelerated cooling could crack the particles by stresses from unrelieved thermal expansion mismatch. The relieve of particle-matrix mismatch stress could blunt out as it reaches the ferrite matrix by the activation of slip systems, and play no part in later cleavage. Alternatively, these cracks in the particles may initiate fracture later. (Ortner, 2006, Agboola, 2010)

#### 2.4.3 STRAIN INDUCED INITIATION

Yokoyama and Nagumo (1998) found cleavage fracture to initiate at intersections of small bainitic grains with different orientations in a mixed area of bainite and ferrite in the proximity of a boundary between coarse bainite. The size of the facets corresponded to the coarse bainite grains, and the brittle crack propagated through these grains. They concluded that the reason for this initiation were due to strain concentrations. The inhomogeneous microstructure in HAZ gives rise to intense strain localizations due to the constraint of plastic deformation and will induce a high defect density and create microcracks in the mixed area of bainite and ferrite. For the crack to propagate, however, the existence of an easy crack path nearby is necessary. This is why they found coarse bainite close to the initiation sites.

#### 2.4.3 LOCATION OF CRACK

The maximum stress ahead of a macroscopic crack occurs at approximately the double CTOD (Crack Tip Opening Displacement) distance away from the crack tip (Anderson, 2005). Mohseni et al. (2014) found cleavage crack initiation to occur at distances,  $X_c$ , shorter than this. Thus, they concluded that the cleavage initiation is influenced not only by the maximum tensile stress distribution in front of the crack tip, but also by the strain condition. Figure 17 illustrate this effect. The total level of stress around the M–A constituents may become significantly larger than the nominal stress value, and consequently cause initiation of cleavage fracture. Brandt et al. (2012) also found the cleavage crack initiation sites to occur typically closer than one CTOD distance from the crack tip. Mohseni et al. (2014) found a tendency of  $X_c$  values increasing with increasing CTOD values, which increased with increasing test temperature, although the scatter was large. As Yokoyama and Nagumo (1998) described, the location of the localized strain also affect the crack initiation location.

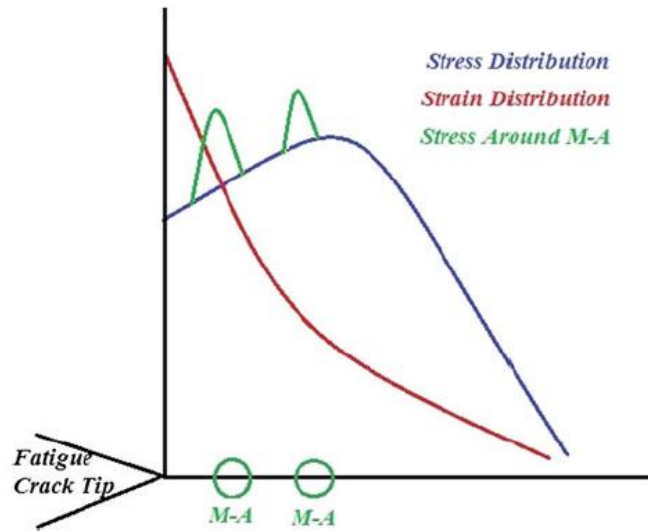


Figure 17 – Stress and strain distribution in front of a fatigue crack tip (Mohseni et al., 2014)

## 2.5 CRACK PROPAGATION AND ARREST

Once a cleavage initiates, the crack may either propagate or arrest. The propagation is controlled by the microstructure and the global driving force. The overall probability of failure is equal to the probability of initiation times the conditional probability of propagation (Lambert-Perlade et al., 2004a). The multiple barrier model addresses this subject. This chapter presents this model, together with microstructural features affecting cleavage crack propagation.

### 2.5.1 MULTIPLE BARRIER MODEL

According to the multiple barrier model, cleavage fracture occurs by following three steps successively, illustrated in Figure 18. The probability of fracture,  $P_f$ , of the specimen is given by the combined probability of each step. (Lambert-Perlade et al., 2004a)

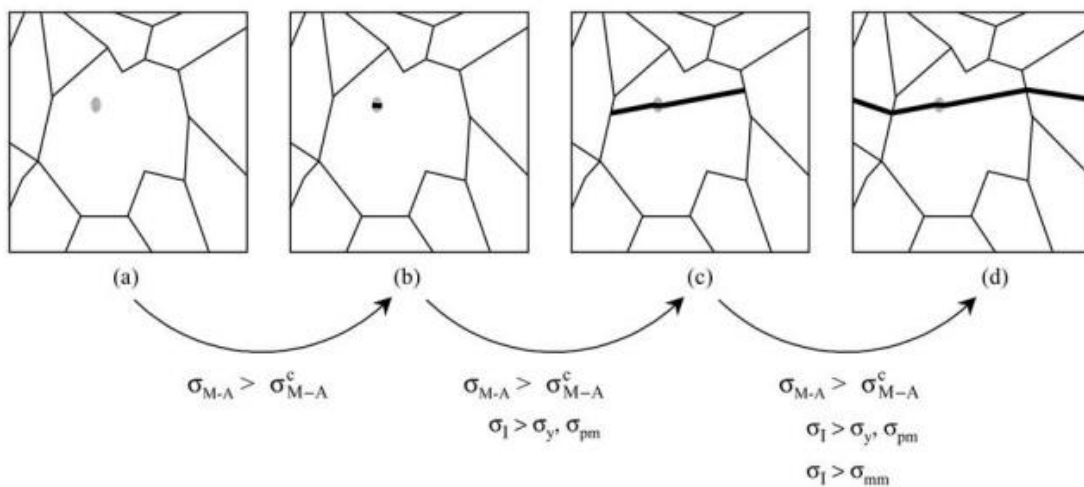


Figure 18 – Schematic representation of the role of microstructural barriers on failure mechanisms (Lambert-Perlade et al., 2004a)



The initiation mechanism can vary as explained in the previous chapter. In the investigations of Lambert-Perlade et al. (2004a), the initiation mechanism was assumed to be due to an intergranular M-A constituent. To initiate cleavage, the local stress has to be larger than the critical stress at the M-A particle,  $\sigma_{M-A}^C$ . The resulting microcrack immediately reaches the particle/matrix interface of strength  $\sigma_{pm}$  and continues to propagate into the matrix if the local maximum principal stress,  $\sigma_1$ , is larger than  $\sigma_{pm}$ . The microcrack quickly reaches a “strong” matrix/matrix interface, which is represented as a high-angle packet boundary of strength  $\sigma_{mm}$  in Lambert-Perlade et al. (2004) paper.  $\sigma_1$  has to be larger than  $\sigma_{mm}$  for the crack to propagate across the matrix/matrix interface and eventually lead to final failure.

The weakest strength barrier is dependent on temperature. The effect of temperature on failure micromechanisms can be described by considering four temperature ranges (Lambert-Perlade et al., 2004a):

- Temperature range I: At very low temperatures,  $\sigma_{mm} < \sigma_{pm} < \sigma_y$  (yield strength). As soon as  $\sigma_1 \geq \sigma_y$  the first particle-cracking event immediately leads to final fracture as the strength of the microstructural barriers is less than the already reached yield strength. Thus at these temperatures, the fracture is nucleation controlled.
- Temperature range II: At somewhat higher temperatures,  $\sigma_{mm}$  is still lower than  $\sigma_{pm}$ . However,  $\sigma_{pm}$  is higher than  $\sigma_y$ , so when  $\sigma_1 \geq \sigma_y$ , the crack arrest after crack initiation at the particle/matrix interface until  $\sigma_1$  reaches  $\sigma_{pm}$ . Thus, at this temperature range, failure is controlled by the strength of the particle/matrix interfaces as it reaches final fracture after this barrier is crossed.
- Temperature range III: At higher temperatures,  $\sigma_y < \sigma_{pm} < \sigma_{mm}$ . Thus, the failure is controlled by the matrix/matrix interfaces as this is the highest strength boundary, i.e. the crack can arrest here if  $\sigma_1$  is not sufficient increased.
- Temperature range IV: At even higher temperatures,  $\sigma_{mm}$  is very high, and ductile fracture occurs before cleavage cracking could develop into the bainitic matrix.

Temperature ranges II and III correspond to propagation controlled cleavage cracking. This was the case in Lambert-Perlade et al. (2004) investigation for temperatures higher than -170 °C. Cleavage microcracks were found to initiate at M-A constituents and propagated through the M-A/bainite interface. At temperatures higher than -60 °C, the microcracks occasionally stopped at high-angle bainite packet boundaries in compliance with temperature range III.

#### 2.5.2 MICROSTRUCTURAL ASPECTS TO CRACK PROPAGATION AND ARREST

According to Lan et al. (2011), some of the microstructural characters controlling cleavage crack propagation are the dislocation structure, grain boundary misorientation and the amount of intergranular ferrite. Once a microcrack forms and propagates into the surrounding matrix, high misorientation boundary is regarded as the only effective obstacle to crack propagation. The crack can be arrested at the high angle boundary (above 30°), or deviate if the angle is somewhat lower. No noticeable deviation is expected for low angle boundaries. It

is generally accepted that a high density of high misorientation boundaries is beneficial to improve the CGHAZ toughness.

Lan et al. (2011) found microstructures with a higher fraction of high angle boundaries to exhibit a larger crack propagation absorbed energy than for microstructures with a lower fraction of these. Coarse-grained bainite in their investigation had a low high angled boundary fraction, and it was concluded that these had little effect on crack deviation and/or arrest during crack propagation. They found the formation of a microcrack in the matrix of this microstructure to immediately lead to final failure. Thus, the fracture micro-mechanism for this microstructure was dominated by crack initiation by large M-A constituents. In their investigation, the coarse-grained bainite contained more and larger M-A constituents than for the less coarse microstructures, which was one of the reasons for the little effect of the high angled grain boundaries, with many initiations in M-A particles happening simultaneously. Lambert-Perlade et al. (2004b), also describes high-angled boundaries as the effective obstacle to crack propagation.

If the bainite packets are sufficiently small, M-A particles are expected not to be significantly harmful. This is due to crack arrest at the packet (angle) boundaries. Investigations with “refined bainite” simulated HAZ microstructure showed numerous of dimples on the fracture surface, both within the cleavage facets and as ductile ligaments (Lambert-Perlade et al., 2004a).

## 2.6 ACOUSTIC EMISSION

*A detailed description about acoustic emission and the equipment used for measuring it can be found in Larsen (2014) project work and master thesis. This chapter summarizes the main aspects.*

Acoustic emission is the transient elastic waves generated in a solid by a rapid, usually localized, stress or strain relaxation (Wadley et al., 1981). This could be due to a wide range of deformation and fracture processes, for example nucleation of a cleavage microcrack. When elastic waves are generated, they move through the material and stimulates a transducer on the material surface. This is a sensor consisting of a piezoelectric element in which a crystal is used to transform the pressure variation (from AE) into electric charge (Larsen, 2014).

AE is commonly used to detect nucleation of cleavage microcracks (Østby et al., 2013). An amplitude of under 50 dB, using an amplifier of 20 dB, is normally considered as background noise, and disregarded in testing. An amplitude of more than 113 dB is regarded as final fracture, and the load is released at this amplitude during fracture mechanic testing (Larsen, 2014). Thus, an amplitude between 50 and 113 dB is considered a local microcrack event. In fracture mechanic testing, Lambert-Perlade et al. (2004a) considered fracture to be controlled by crack propagation, as long as (at least) one microcrack event could be detected before final fracture of the specimen.

The shape of the AE signal associated with the arrest of microcracks is a so-called “burst” signal, shown in Figure 19. The signal rapidly reach the peak amplitude, i.e. has a rapid rise time, followed by a characteristic signal ring-down.

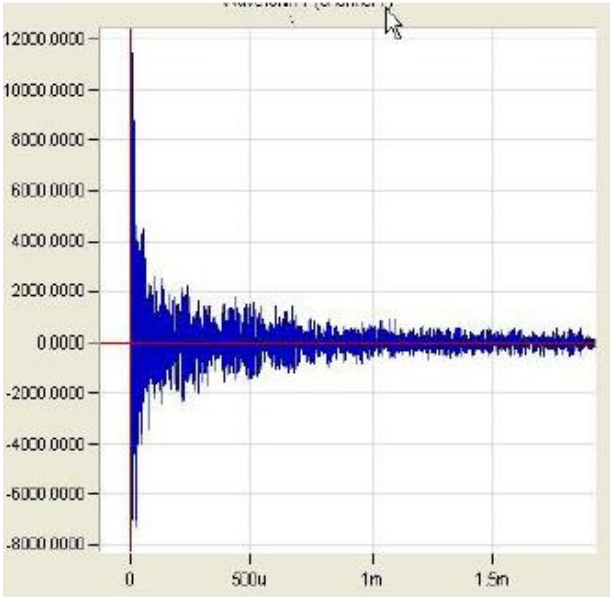


Figure 19 - Example of AE "burst" signal associated with microcrack arrest (Østby et al., 2013)

2.7 PREVIOUS RESULTS FROM ARTIC MATERIALS I USING AE

In the Artic Material I project (AM I), the 420 MPa steel plate used in the investigation has the chemical composition as shown in Table 1. This chapter summarizes two relevant papers from this project. To ne noted, the article referenced earlier by Brandt et al. (2012) is also a part of this project, using the same 420 MPa steel.

Table 1 – Chemical composition of 420 MPa steel from Artic Materials I

C	Si	Mn	P	S	Cu	Ni	Nb	N	CEV
.09	.19	1.54	.0004	.002	.28	.72	.013	.0035	.41

2.7.1 QUANTITATIVE RELATION BETWEEN ACOUSTIC EMISSION SIGNAL AMPLITUDE AND ARRESTED MICROCRACK SIZE

The sub-chapter heading is the name of the article by Østby et al. (2012) which lay the basis for this thesis. The following is a summary of their article.

The material tested was an API X65 pipeline (2 samples) and the 420 MPa rolled plate (7 samples) with chemical composition given in Table 1. Both materials were weld simulated in order to obtain ICCGHAZ 15 microstructure, with a peak temperature for the first cycle at 1350 °C and 775 °C for the second cycle. This resulted in an austenite grain size of approximately 100 µm after the first cycle, and M-A phases in the final microstructure formed on the prior austenite grain boundaries.

The specimens were subjected to 3-point bending loading at  $-30\text{ }^{\circ}\text{C}$ , with AE transducers to measure the AE signals. Before testing, the specimens were machined down to a cross section of  $10\times 10\text{ mm}$ , and a notch of  $5\text{ mm}$  was created with spark erosion followed by fatigue loading. In order to easily find and measure the size of the arrested cleavage microcrack, the loading was stopped after reaching the first AE signal (after a given threshold amplitude of  $50\text{ dB}$ ), and then fatigue fractured.

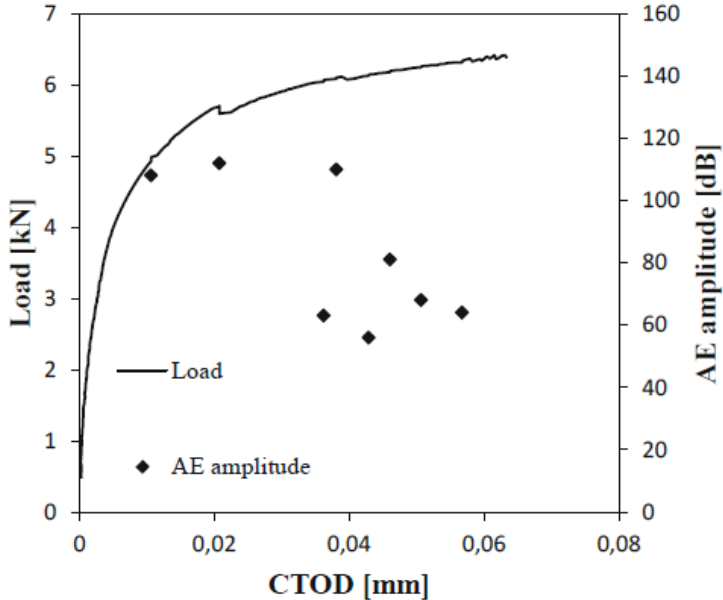


Figure 20 - Example of load drop with high AE signal amplitude (Østby et al., 2012)

The AE amplitude signals was in the range of  $64\text{--}112\text{ dB}$ , and had the characteristic “burst” shape, seen in Figure 19. For specimens with high AE amplitude signals there were a small load drop associated with the AE signal on the global load vs CTOD curves. This is illustrated in Figure 20 for a specimen loaded to macroscopic fracture. This support the assumption of a correlation between AE amplitude and the size of a local microcrack event.

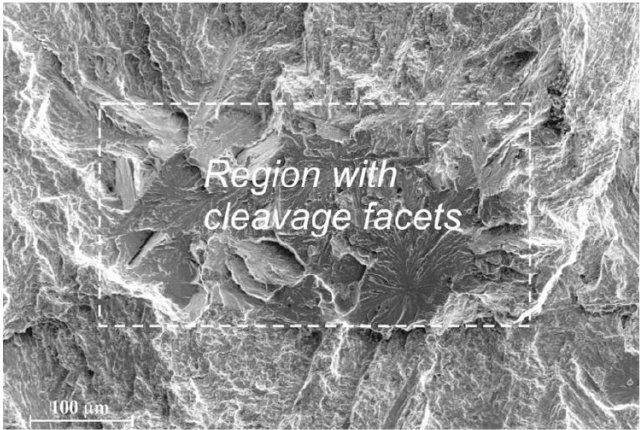


Figure 21 - Area with isolated cleavage facets observed in SEM of X65 test no. 1 (Østby et al., 2012)

Each sample revealed one area of isolated cleavage facet at or just in front of the pre-test fatigue notch tip when examined in SEM. This is shown in Figure 21 for the X65 test No. 1. The square root of the indicated rectangle is taken as an approximately measure of the microcrack size,  $a_{micro}$ . This was linked to the AE signal amplitude with the following equation:

$$V_{AE} = k(a_{micro})^2 \tag{2}$$

where  $V_{AE}$  is the voltage amplitude in the AE transducer and  $k$  is a constant. This equation is a simplification from a relation theoretically derived by A.V. Lysak, for the elastic displacement,  $D$ , caused by a sudden creation of a circular microcrack in a semi-infinite medium:

$$D = F \frac{r^2}{R} \tag{3}$$

where  $r$  is the radius of the microcrack,  $R$  is the distance from the microcrack to the point of observation, and  $F$  is a function depending on several factors like microcrack orientation etc. Equation 2 is further linked to the AE signal amplitude by using the relation:

$$A_{AE} = 20 \log \left( \frac{V_{AE}}{V_{ref}} \right) + A_{pre} \tag{4}$$

where  $A_{AE}$  is the dB amplitude of the AE signal,  $V_{ref}$  is a reference voltage (1  $\mu$ V), and  $A_{pre}$  is the amplitude of the pre-amplifier which was set to 20 dB.

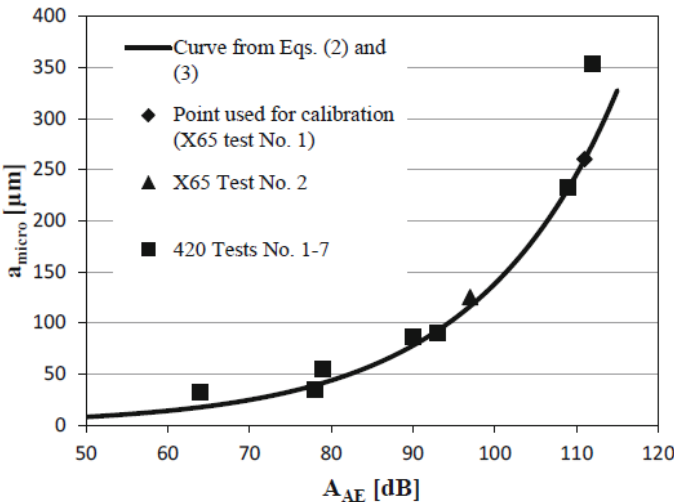


Figure 22 – Relation between the microcrack size and AE signal amplitude (Østby et al., 2012)

The curve illustrating the relations in equation 2 and 4 can be seen in Figure 22 (named eq. (2) and (3) in the figure), calibrated from sample X65 test No. 1. The measured results from the tested samples are also plotted, and show a good fit to the curve. This indicates that there is

a strong correlation between the measured local cleavage microcrack size and the amplitude of the AE signal recorded, and that this is the relation theoretically derived by Lysak.

#### 2.7.2 MONITORING OF CLEAVAGE MICROCRACK ARREST IN WELD THERMAL SIMULATED MICROSTRUCTURES BY MEANS OF ACOUSTIC EMISSION

This paper by Østby et al. (2013), take in use the relationship between microcrack size and AE signal amplitude, established in the previous paper. The investigation considers the effect of temperatures and HAZ microstructures, and the relative importance of crack nucleation rate and arrest of microcracks on fracture toughness.

The material tested was the same 420 MPa rolled plate, with the same weld simulation parameters (except for second weld simulation cycle having a  $T_p$  of 780 °C), and with the same AE set up/parameters for fracture mechanic testing as in the previous paper, although all these specimens were run to fracture. The different temperatures for fracture mechanic testing and HAZ microstructures are shown in Figure 23. The prior austenite grains size was estimated to be approximately 130  $\mu\text{m}$  for the ICCGHAZ 15 microstructure and approximately 100  $\mu\text{m}$  for the CGHAZ 5 and ICCGHAZ 5 microstructures.

The result showed an increase in CTOD values for all temperatures, especially at 0 °C, seen in Figure 23 (see Østby et al. (2013) for more, and bigger graphs). As seen, the CTOD values for ICCGHAZ 5 is highest and most increasing with temperatures, reaching ductile behavior at 0 °C. This is in good correlation with the number of AE signals, i.e. number of local micro-cracking events. The rate of nucleation decreases with increasing CTOD, which indicate that there is less nucleation for higher CTOD values.

For ICCGHAZ 15, this rate is more or less constant for 0 to -60 °C, as seen in the figure. Thus, the increase in CTOD values with increasing temperatures is probably due to an increase in local crack arrest toughness with increasing temperature. The crack nucleation rates is much less for 0 °C, which could indicate that the higher CTOD value at 0 °C is due to a strong reduction in crack nucleation.

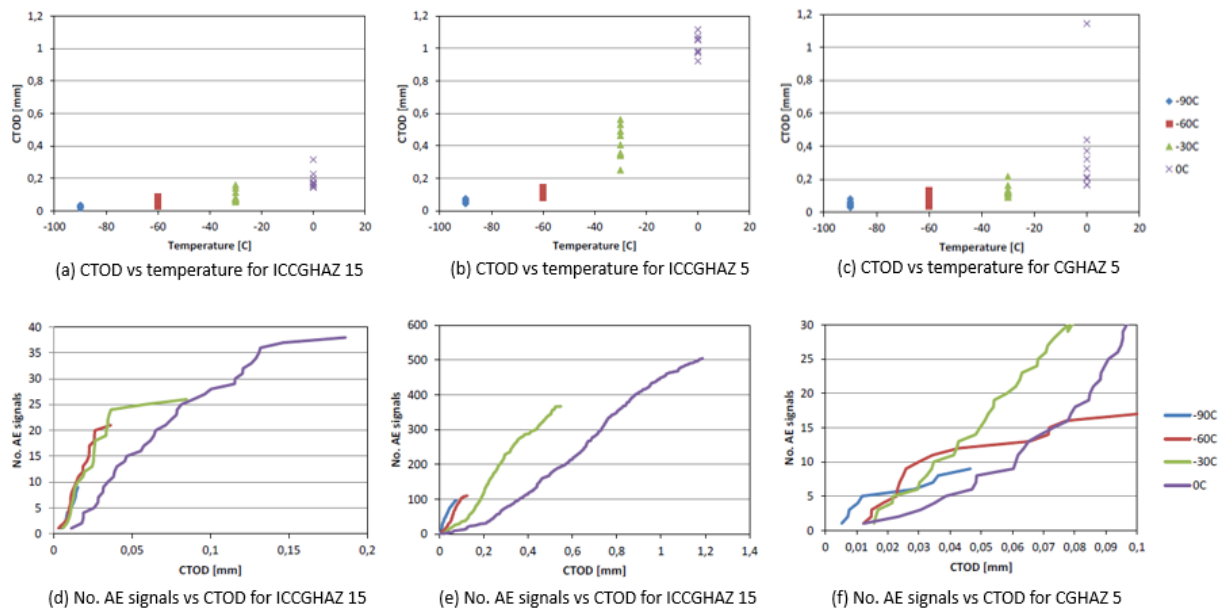


Figure 23 – Graphs from Østby et al. (2013)

Regarding the arrested microcrack sizes calculated from the AE signal amplitude, ICCGHAZ 15 seemed to be more dependent of temperature, and have a larger size than the others. This was estimated to be in the range of about 70-150  $\mu\text{m}$ , while for the others it was in the range of about 40-50  $\mu\text{m}$ . 0  $^{\circ}\text{C}$  has the smallest arrested microcrack size for ICCGHAZ 15, which could indicate a local increase in crack arrest toughness as well as decrease in nucleation rate. The size difference between the different weld simulations could be linked to the prior austenite grain size, as this value is higher for ICCGHAZ 15.

All three microstructures displays significantly AE activity. Given this is most likely due to crack nucleation, this means that there must be a lot of local crack arrest prior to macroscopic fracture, otherwise the fracture would happen much faster given all the cracks. This demonstrate that the microstructures display a significant influence of propagation control, i.e. the critical stage is not nucleation of the crack but further propagation, when it comes to global brittle fracture.

### 3. MATERIAL

The material investigated in this thesis is a Ruukki 420 MPa steel plate. A screening test of this has been published in a restricted report (Akselsen, 2014a). This chapter summarizes the results regarding the base plate properties and the weld simulation.

#### 3.1 BASE PLATE PROPERTIES

The plates chemical composition and mechanical properties reported by Ruukki is given in Table 2 and Table 3, respectively.

Table 2- Chemical composition of the plate

Cast No	Chemical composition %											Additional elements	CEV	Pcm
	C	Si	Mn	P	S	Al	Cu	Cr	Ni	Mo				
72722	.019	.25	1.59	.008	.002	.027	.257	.23	.34	.206		Nb, Ti	.41	.15

Table 3- Mechanical properties of the plate given by Ruukki

Plate no.	Thickness (mm)	Tensile tests				Charpy-V impact test at - 60 °C				
		Test direction	Rp0.2 (MPa)	Rm (MPa)	A5 (%)	Test direction	Impact energy (J)			
							individual	avg		
72722-041	50	Transverse, head	498	580	23.9	Transverse, head	350	362	330	347
		Transverse, tail	505	581	24.1					

The screening tests SINTEF did of the base material gave an average yield strength of 480 and 491 MPa at room temperature and at – 60 °C, respectively. The average tensile strength was 575 and 626 MPa, respectively. This is approximately compliance with Ruukki’s results.

#### 3.2 WELD SIMULATION PROPERTIES

Weld simulation were conducted on specimens which were cut from the base metal with their length axes perpendicular to the plate rolling direction and machined to "standard" weld thermal simulation specimen size of 11x11 mm<sup>2</sup> cross section and 100 mm length. Both CGHAZ and ICCGAZ microstructures were simulated with a peak temperature of 1350 °C for the first cycle for both microstructures and 780 °C for the second cycle for ICCGAZ. The cooling rate, Δt<sub>8-5</sub>, was 5, 10 and 15 seconds.

The Charpy-V notch toughness for the weld simulated samples at -60 °C is shown in Figure 24. Information about this test method can be found in literature, it will not be further discussed in this thesis. The result presented here is just to give an indication of the fracture toughness.



“The CGHAZ and ICCGAZ toughness levels seem to increase with increasing  $\Delta t_{8/5}$  values (increasing heat input), which is contrary to the trend normally observed in such experiments. Although huge scatter is found, only high CGHAZ Charpy values were found for the slowest cooling rate ( $\Delta t_{8/5}$  of 15s). Also the ICCGAZ had one high value here. Otherwise, the ICCGAZ impact properties were low (< 50 J). The reason for this is yet not known. Since the low steel carbon content should prevent the blocky M-A (martensite-austenite) phase to form, somewhat better toughness should have been expected.” (Akselsen 2014, p.10)

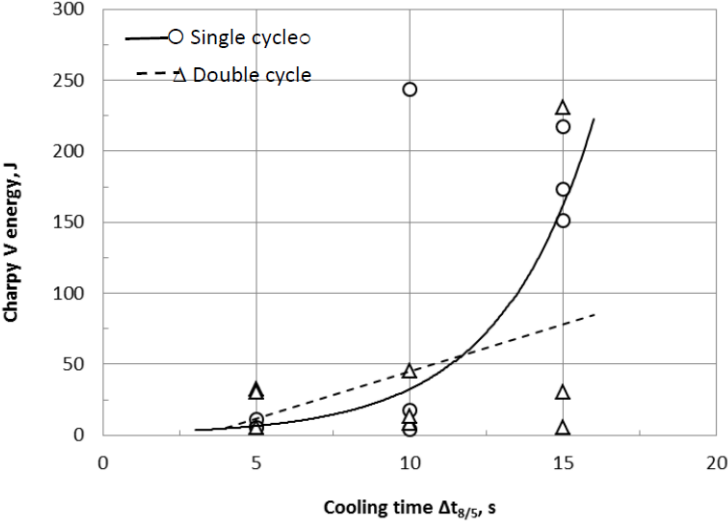


Figure 24 – Effect of cooling time on Charpy-V notch toughness at – 60 °C for weld simulated samples (Akselsen, 2014a)

The CTOD fracture toughness for the weld simulated samples at -60 °C is shown in Figure 24. As for the Charpy specimens, it is a large scatter and the trend is that the CTOD results increases with increasing cooling time.

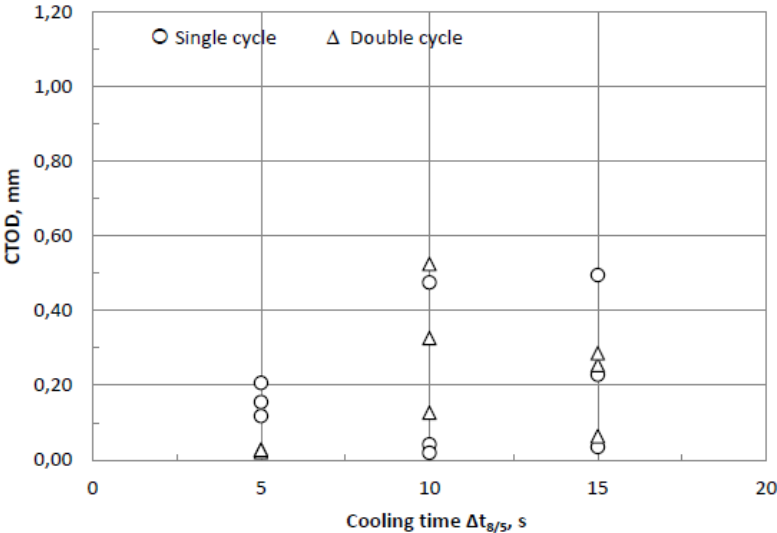


Figure 25 - Effect of cooling time on CTOD toughness at – 60 °C for weld simulated samples (Akselsen, 2014a)

### 3.3 MICROSTRUCTURE EXAMINATION

Figure 26 show the microstructure for the weld simulated samples. For the single cycle, bainite seems to be the primary microstructure constituent with some fine ferrite grains nucleated. There seem to be a general coarsening with increasing cooling time. The microstructure for the double cycled weld simulations does not seem to change much from the single cycle. Hence, the microstructure for ICCGHAZ is predominantly bainitic. There were virtually no sign of M-A islands. Based on this microstructural examination, Akselsen (2014a) concluded that there were not any straight relationship between the microstructures and the observed toughness.

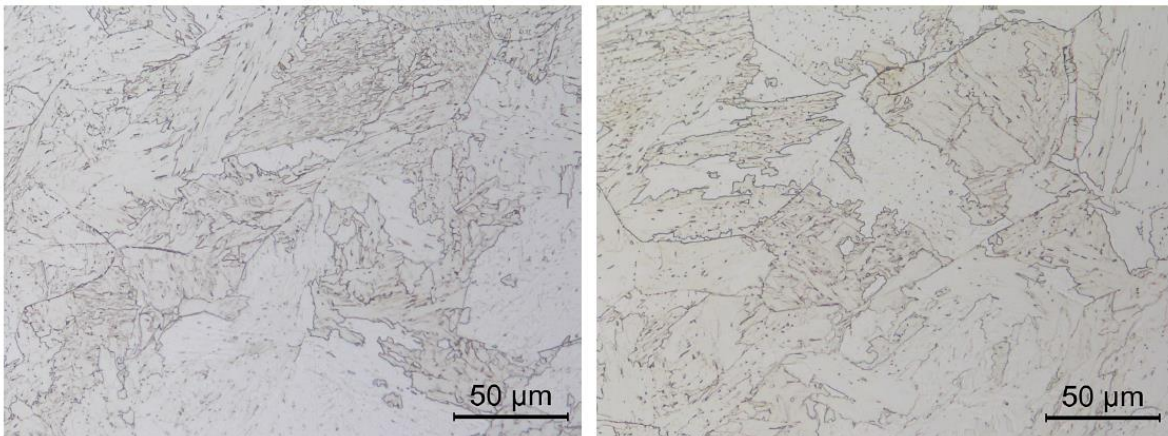


Figure 26 – Weld simulated microstructures, left: CGHAZ 15, right: ICGHAZ 15

### 3.4 VICKERS HARDNESS MEASUREMENTS

Vickers hardness measurements for weld simulated samples are given in Figure 27. According to Akselsen (2014a), these values are low. The hardness is similar for both weld simulations, and it seems to increase a slightly with increasing cooling time.

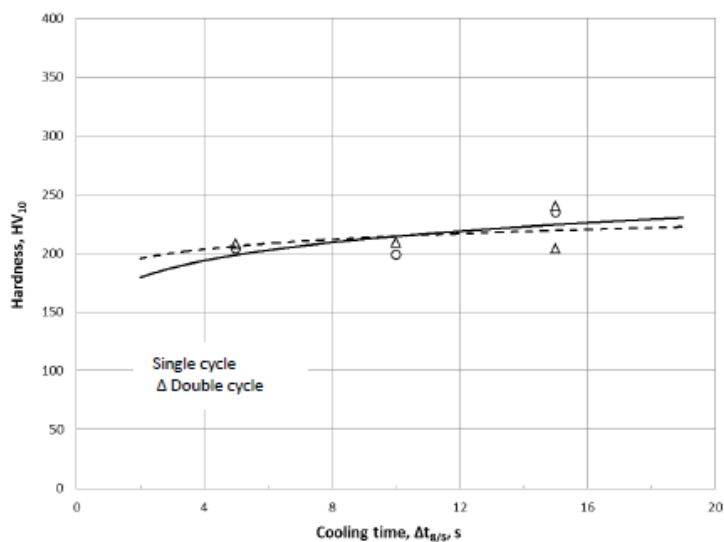


Figure 27 – Effect of cooling time on mean hardness (Akselsen, 2014a)

## 4. EXPERIMENTAL METHODS

*This chapter present the experimental methods conducted in this thesis, in order to better understand the brittle fracture micromechanisms for the steel.*

### 4.1 FRACTURE MECHANIC TESTING WITH ACOUSTIC EMISSION

#### 4.1.1 TEST SET-UP AND SAMPLE PREPARATION

The fracture mechanic testing with acoustic emission and sample preparation for this was conducted by SINTEF, and has been carried out since the autumn of 2014. The first results were sorted and analyzed in Larsen (2014) project work. In this thesis, these results will be discussed together with the test results from 2015, concerning 3-point bending loading with a notch depth of 5 mm (SENB05), as this is the same test method conducted in 2014. Information about fracture mechanic testing can be found in literature and in Larsen (2014) project work. The necessary information about the testing for this thesis is the following:

Weld simulation specimens were cut from a 50 mm thick plate, as illustrated in Figure 28. The specimen were cut in the transverse direction, with a cross section of 11x11 mm<sup>2</sup> a few mm from the top and bottom (i.e. two specimens cut from the transverse height). After weld simulation, the specimens were machined to CTOD testing parameters, i.e. with a cross section of 10x10 mm<sup>2</sup>, and a length of 100 mm. A notch was created with spark eroding for 4 mm and fatigue cracking for 1 mm to obtain SENB05. The testing was conducted in the isolated chamber seen in Figure 29. The specimen set up is illustrated in Figure 30, which is the same as by Østby et al. (2013). A force is applied on the opposite edge of the notch, the same edge in which AE-sensors are attached to collect the AE signals.

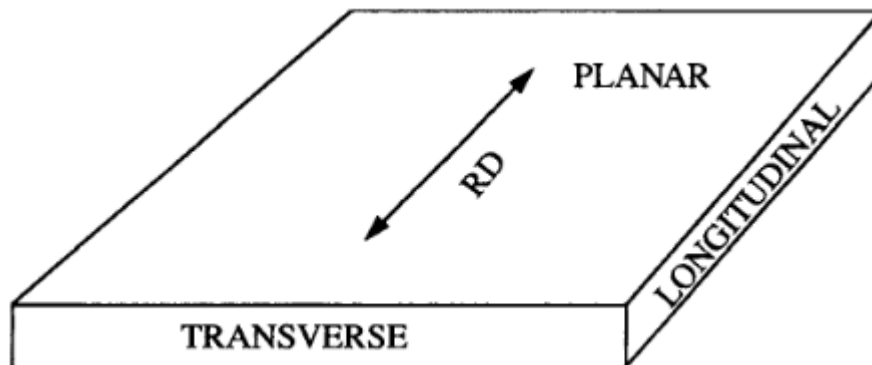


*Figure 28 - The three planes in a rolled product. The rolling direction (RD) is shown by the arrow (Bramfitt and Benscoter, 2001)*

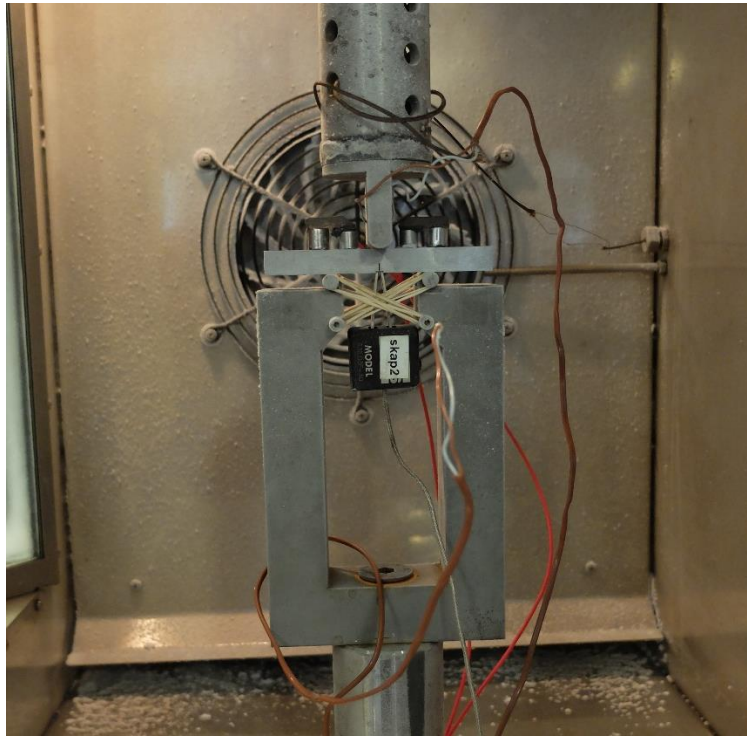


Figure 29 – Test set-up

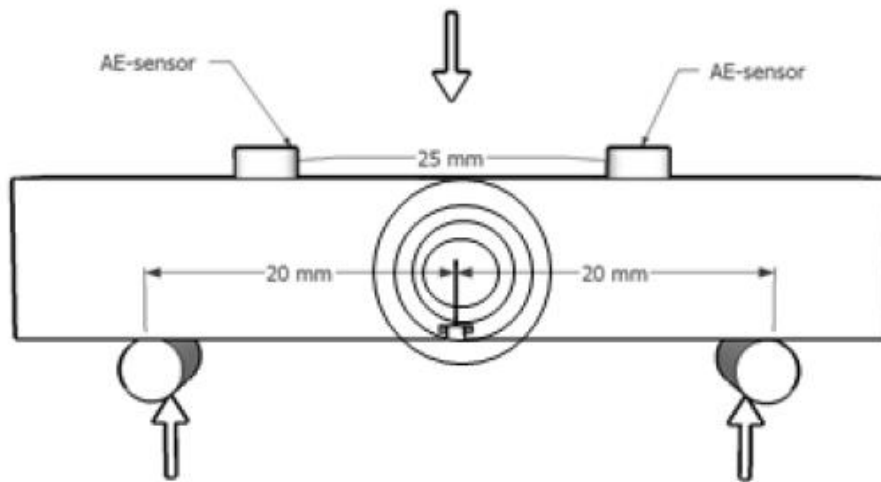


Figure 30 – Specimen test set-up (Østby et al., 2013)

#### 4.1.2 TEST PROGRAM

The weld simulation parameters were for all specimens, a 1350 °C the peak temperature for the first cycle and 780 °C for the second cycle. For the test conducted in 2014, three parallels at - 60 °C were run for CGHAZ and ICCGAZ 5, 10 and 15 (SENB05). P-TPI X80 pipeline steel was also tested in 2014, but this thesis only focuses on the 420 MPa steel. The program for the tests run in 2015 is summarized in Table 4, as seen only one cycle weld simulated samples were tested.

Table 4 – Test program in 2015

Test temperature:	CGHAZ 5	CGHAZ 15	CGHAZ 25
22 °C (RT)	3	3	0
0 °C	3	3	0
-30 °C	3	3	3
-45 °C	0	0	3
-60 °C	0	0	3
-75 °C	0	0	3

The test described above, are all run to fracture. As mention in the introduction, interrupted test are also run. These tests was stopped after reaching the first AE signal, after a threshold amplitude of 50 dB, and then the specimen was fatigue fractured. This was conducted in order to easily find and measure the size of the arrested cleavage microcrack , as conducted by Østby et al. (2012). The test program for the interrupted samples was approximately as shown in Table 5.

Table 5 – Test program for interrupted samples

Test temperature:	CGHAZ 5	CGHAZ 15	CGHAZ 25	ICCGHAZ 5	ICCGHAZ 15	ICCGHAZ 25
-30 °C	4	3	0	1	2	0
-45 °C	0	0	0	0	1	1
-60 °C	2	5	3	8	7	9

## 4.2 MICROSTRUCTURAL CHARACTERIZATION

### 4.2.1 MICROSTRUCTURE IN HAZ

In order to characterize the microstructure in the HAZ, fractured specimens were cut, grinded, polished and etched. This was done at the metallurgy laboratory at IPM, NTNU. Seven samples were investigated; one sample for each weld simulation parameter of the tests from 2014, except for the CGHAZ 10, in which two samples were investigated. The specimens were cut by an aluminum oxide abrasive cut-off wheel (Struers 30A15), around 10 mm from the fracture surface. The side vertical to the fracture surface corresponding to the transverse rolling direction was then grinded with various steps of waterproof silicon carbide grinding paper, starting from a P#80 finishing with a P#4000 mesh. The samples were cleaned in an ultrasonic bath do remove all the dirt, before polishing with a diamond spray of first 3 µm and then 1 µm.

After polishing, the samples were etched with 2 % nital for 15 seconds. After investigation of the nital etched samples in a light microscope, one sample from CGHAZ 15 and one sample from ICCGHAZ 15 was LePera etched for 20 seconds in order to reveal possible M-A constituents. These was studied in SEM. After both etching procedured, the samples were thoroughly rinsed with ethanol and dried with a hair dryer.

#### 4.2.2 MICROSTRUCTURE IN BASE MATERIAL

The base material on an ICCGHAZ 15 simulated sample were also investigated. This was cut around 15 mm from the other side of the fracture surface in order to be sure that the material was not affected by the heat from the weld simulation. The side investigated was the same as the one cut, i.e. corresponding to the longitudinal rolling direction. The grinding and polishing was the same as explained above, and it was also etched with 2 % nital for 15 seconds.

#### 4.2.3 GRAIN SIZE DETERMINATION

The prior austenite grain size was measured by looking in the light microscope and comparing several micrographs taken of the specimens. This is a very rough measurement and only in one orientation. As the grain structure is not equiaxed, the grain size should have been evaluated on at least two of the three principle planes (Figure 28) and averaged, according to the ASTM International standard (2014). As this would be very time consuming, this was not conducted. The microscopic analysis was conducted at the microscopy laboratory at IPM, NTNU.

#### 4.2.4 VICKERS HARDNESS MEASUREMENTS

Vickers hardness measurements was conducted in order to better classify the microstructure. See Larsen's master thesis for the procedure, as this was conducted by him.

### 4.3 FRACTURE SURFACE CHARACTERIZATION

#### 4.3.1 SEM ANALYSIS

The samples was cut as explained above, and put in an ultrasonic bath in a beaker containing ethanol for two minutes, in order to clean the samples. Secondary electrons in SEM was used to reveal the topography of the fracture surfaces. The samples investigated was the other fracture surface of the ones conducted a microstructural analysis on, except for one of the CGHAZ 10 samples. In addition, one more CGHAZ 5 and 15 simulated samples and three CGHAZ 25 simulated samples from 2015 were investigated. All of the SEM investigations were conducted at the nano-mechanical laboratory at IPM, NTNU.

#### 4.3.2 EDS ANALYSIS

An EDS analysis were conducted on the fracture surface for the interrupted samples. Several spots were taken on the different features to account for potential scatter. Table 6 summarizes the different features investigated and how many of each on the different samples. This was mostly conducted by Larsen.

*Table 6 – EDS investigation features, and amount of different sites for each feature*

<b>Sample</b>	<b>Matrix</b>	<b>Flat area</b>	<b>Inclusion</b>
<b>126</b>	2	3	2
<b>167</b>	2	4	3
<b>180</b>	6	5	2
<b>217</b>	4	4	3
<b>339</b>	2	1	1

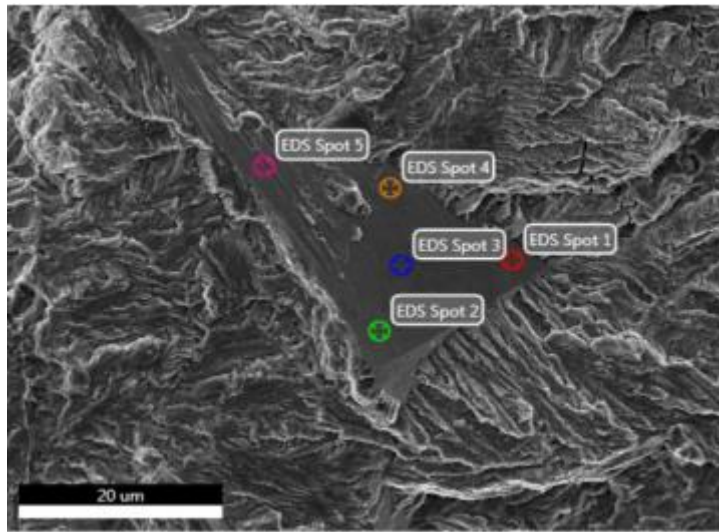


*Figure 31 – Example of EDS analysis sampling from sample 167*

## 5. RESULTS

*This chapter presents the results, with a short discussion with some of them to be able to present it better. An extensive discussion will be conducted in the next main chapter. It is to be noted that the sample numbers are from SINTEF's markings.*

### 5.1 MICROSTRUCTURE

The material is highly inhomogeneous, both in the base material and in the HAZ. It is therefore very difficult to classify the microstructure. The samples presented in this chapter are etched with nital. In general for this etchant, martensite would appear brown, grain boundaries black and ferrite white. However, this could deviate some in regards to the orientation of the grains.

Almost all of the specimens had an approximately average prior austenite grain size of 100  $\mu\text{m}$ . This number could have a deviation of around  $\pm 30 \mu\text{m}$ . In addition, to there were some natural deviation in the prior austenite grain sizes. The general microstructure for all specimens seemed to be a mixture of upper bainite and martensite with varying degree of auto-tempering, and perhaps some ferrite. It is believed to be auto-tempered martensite present because the  $M_s$  for the steel is high. According to equation 1 and Table 2, it would be at 472.3 °C. There seem to be a coarsening in the microstructure as the cooling time increases, and a tendency to form more upper bainite than martensite, as seen in Figure 32. Bigger micrographs of the samples is found below and in the appendix. All micrographs, except for the base material, are obtained close to the fracture surface, i.e. in the CGHAZ/ICCGHAZ.

The CGHAZ 15 simulated microstructure is seen in Figure 33 for sample 7. As seen, the microstructure consist mostly of coarse upper bainite with dotted lines due to the small amount of carbon. There is some areas that are believed to be auto-tempered martensite appearing as white with black dots. This could be, however upper bainite with grain orientation in/outwards off the plane. All of these microstructures are indicated with arrows in the figure. Sample 12 (ICCGHAZ 15) has similar microstructure as sample 7 (CGHAZ 15), seen in Figure 34. However, it seems to contain more of the auto-tempered martensite.

It is difficult to determine any differences in the microstructure for sample 17 and 18 (ICCGHAZ 10). Although they both are etched for 15 seconds, sample 18 seems to be a little over-etched. There seemed to be a tendency to have more of the areas indicated with an arrow in Figure 35, i.e. a very fine-grained structure, with shorter cooling times. It is uncertain what this area is, but it is believed to be either martensite or fine-grained bainite with possible some ferrite.

The base material for sample 12 is shown in Figure 36 and Figure 37. As seen, the grains are elongated in longitudinal rolling direction. Some large white grains were found. The high magnification in Figure 37 indicate that these could be further divided into smaller grains, and the small, almost invisible lines in them indicate that they could be bainite or martensite, as ferrite should not contain any black particles with its low solubility of carbon. The grains are varying in size, some are found as small as 2  $\mu\text{m}$ .



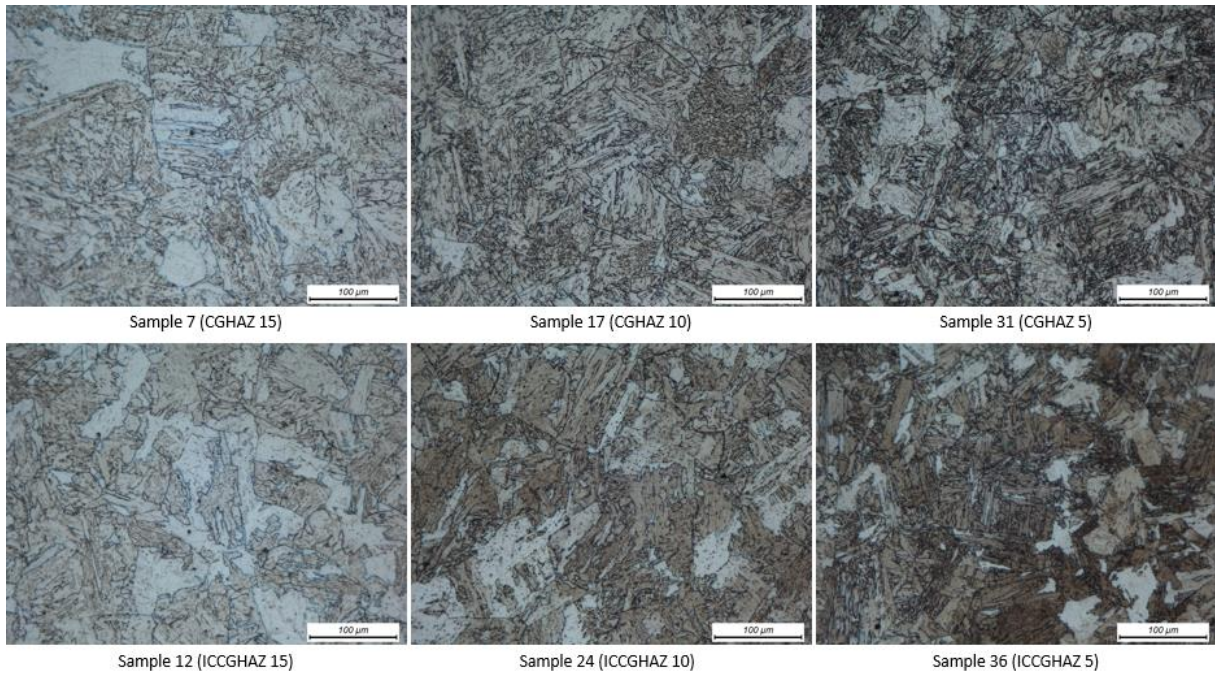


Figure 32 – Micrographs of the specimens with different weld simulations

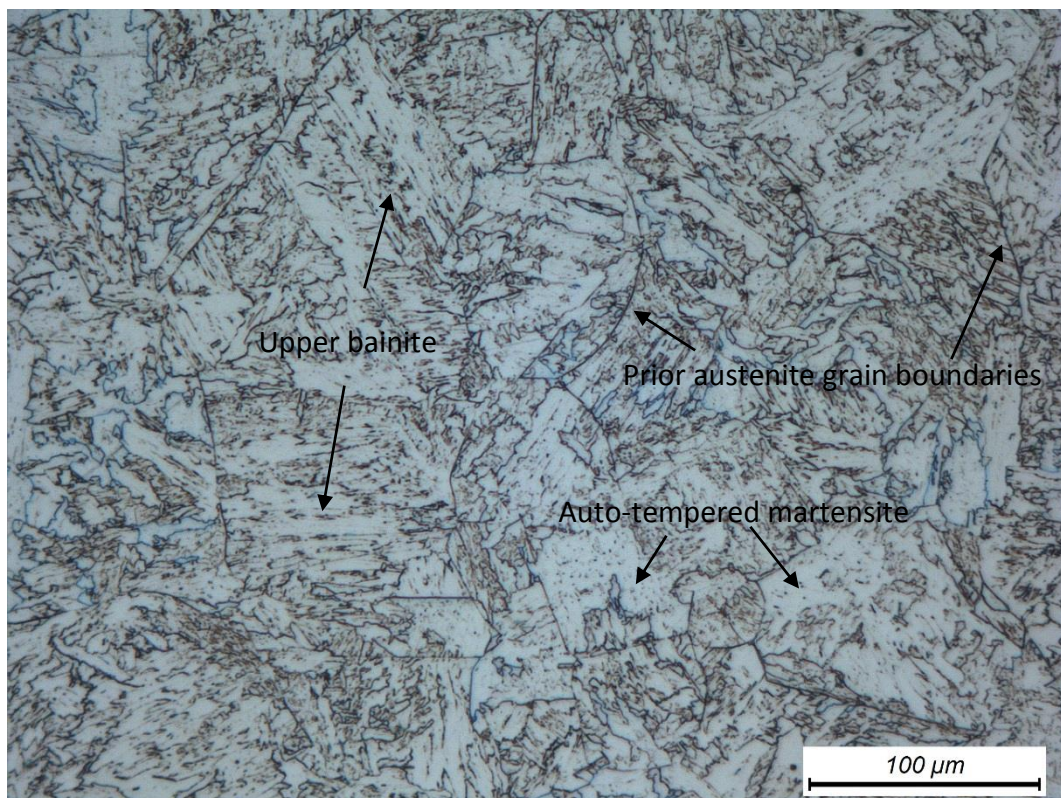
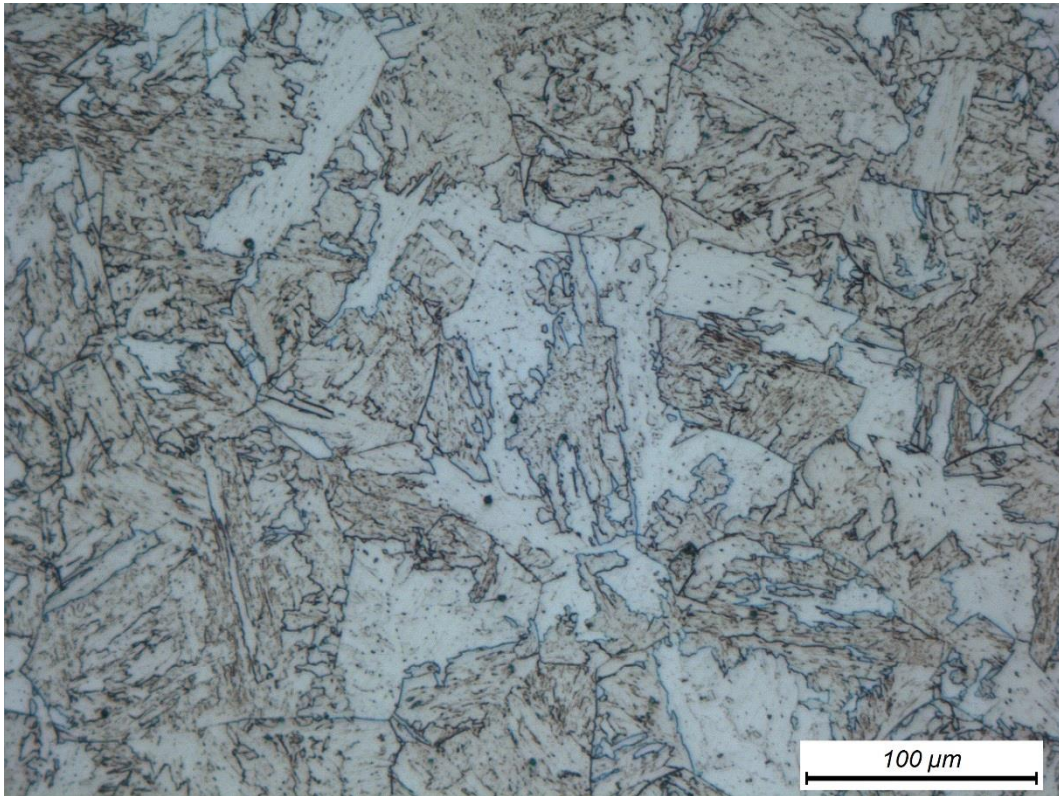
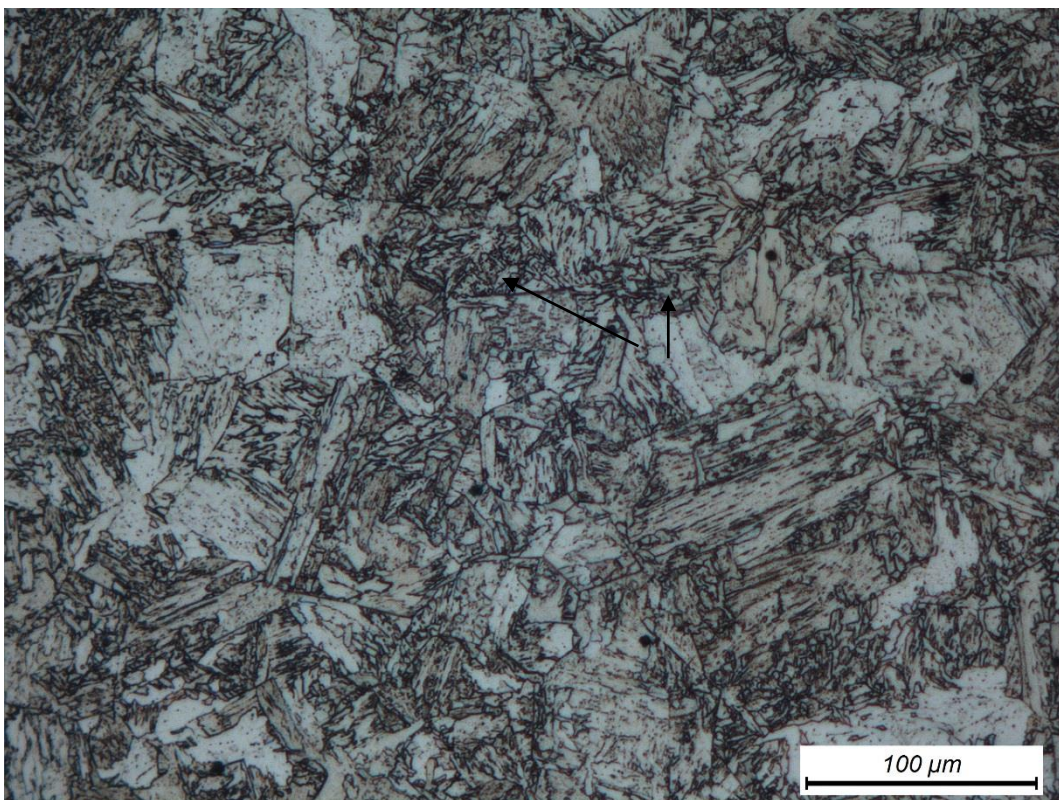


Figure 33 – Micrograph of sample 7 (CGHAZ 15)





*Figure 34 – Micrograph of sample 12 (ICCGHAZ 15)*



*Figure 35 – Micrograph of sample 31 (CGHAZ 5), arrows indicating possible martensite or fine-grained bainite and ferrite*



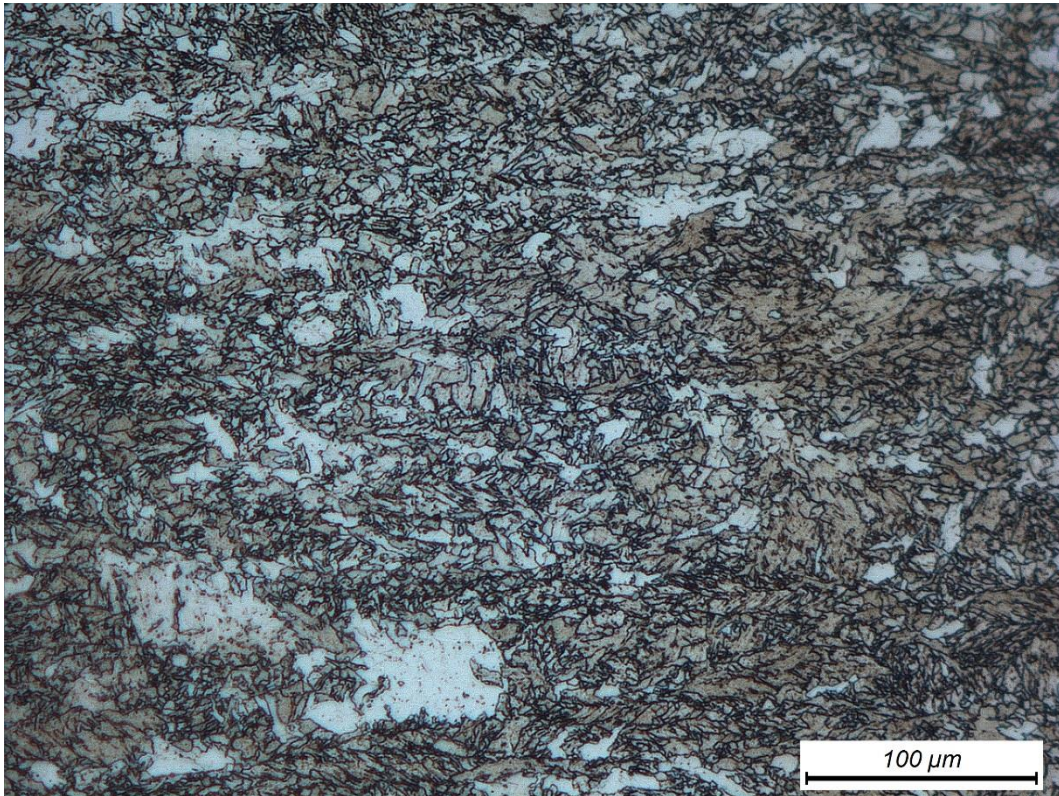


*Figure 36 - Micrograph of the base material in sample 12*

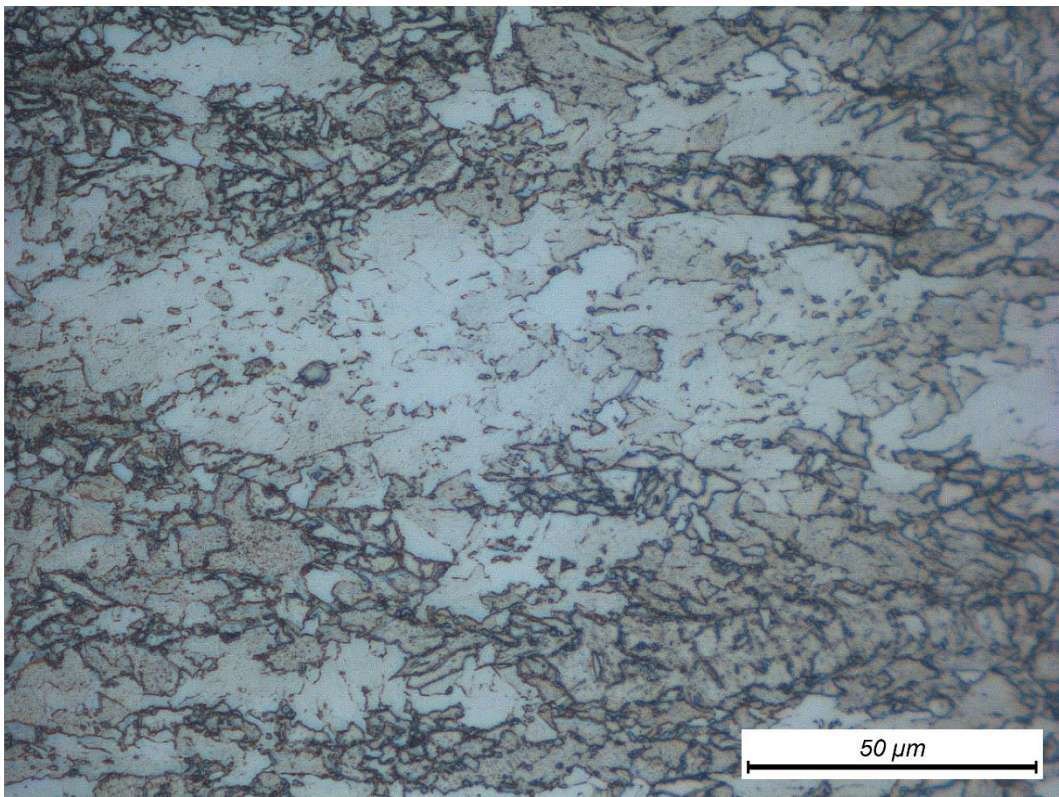


*Figure 37 - Micrograph of the base material in sample 12*

### 5.1.2 M-A PHASES

The LePera etched samples indicated very similar M-A amounts and morphology in both the CGHAZ 15 and ICCGHAZ 15 simulated samples. The following descriptions apply for both samples. The M-A phases was distributed approximately as seen in Figure 38 through Figure 41. As seen, there is little M-A constituents on the prior austenite grain boundaries for both samples. The M-A constituents were mostly short elongated stringers or very small blocky particles located between bainite or martensite laths.  $L_{max}$  for the blocky particles were typically less than 1  $\mu\text{m}$ , and for the stringers it was around 2  $\mu\text{m}$ , similar to the one indicated in Figure 38.

These results comply with the results from Aksel Louis Legouy Kvaal and Brage Dahl Snartland's master theses, written simultaneously as this one. They are conducting nanomechanical testing on weld simulated specimens from the same steel investigated in this thesis. Their M-A investigations was conducted on the transverse rolling direction, and the weld simulations were CGHAZ 15 and ICCGHAZ 15. (A.L.L Kvaal and B.D.S 2015, pers.comm., 1 June)

Kvaal and Snartland did not find any big M-A constituents, in contrast with the investigation results in this thesis. Some stringer M-A constituents were found to have a  $L_{max}$  up to 7  $\mu\text{m}$ , and a few blocky M-A island were found up to around 3  $\mu\text{m}$ . These were found both intergranular and on prior austenite grain boundaries, indicated with arrows in Figure 40 and Figure 41.



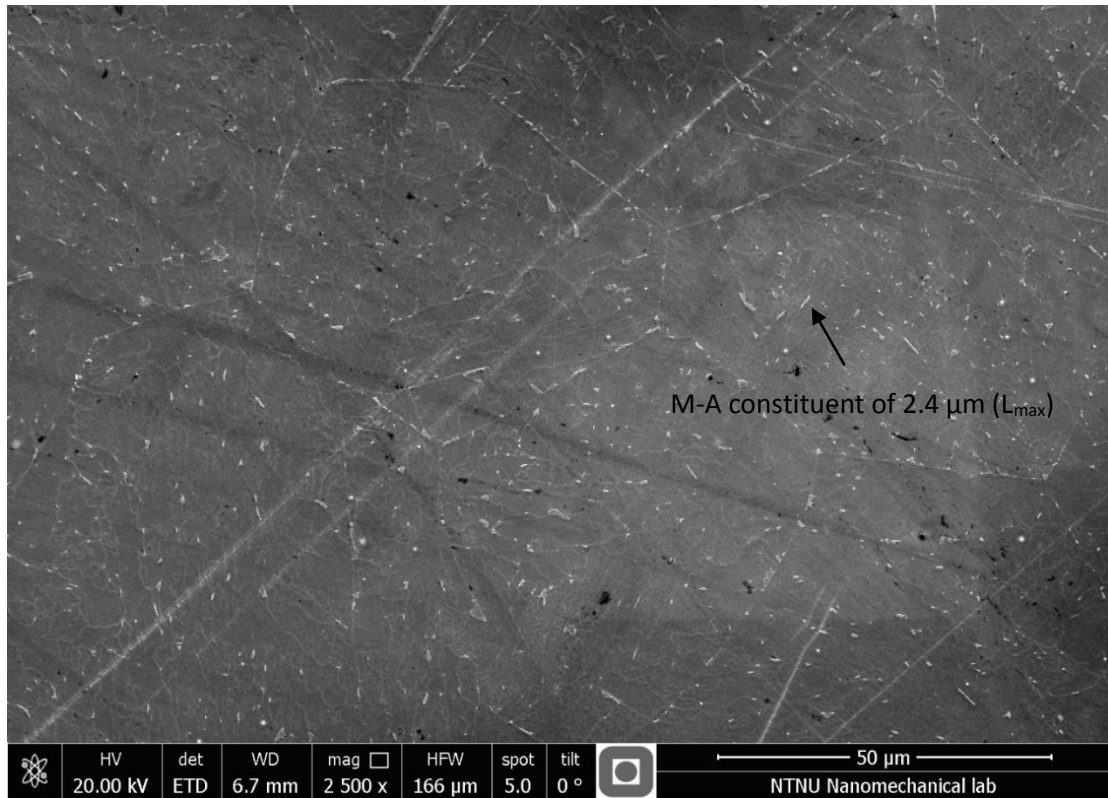


Figure 38 – SEM micrograph of sample 7 (CGHAZ 15), close to the fracture surface. LePera etched for approx. 20 sec.

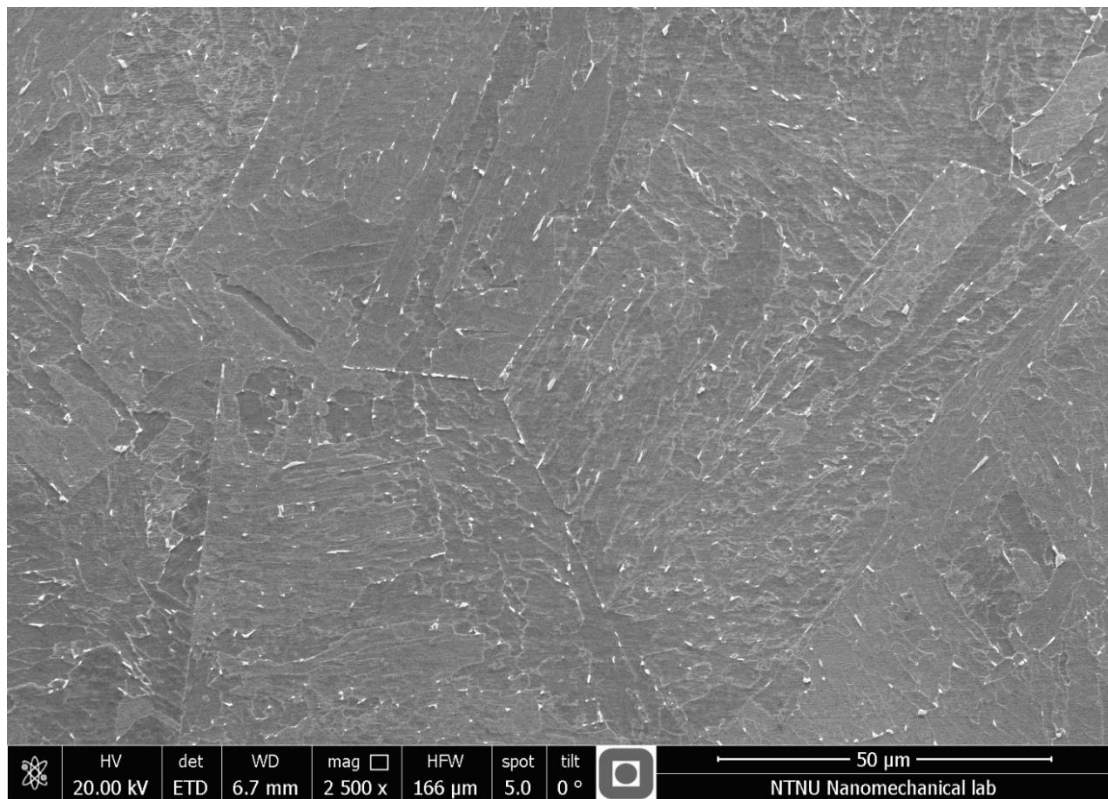


Figure 39 – SEM micrograph of sample 12 (ICCGHAZ 15), close to the fracture surface. LePera etched for approx. 20 sec.

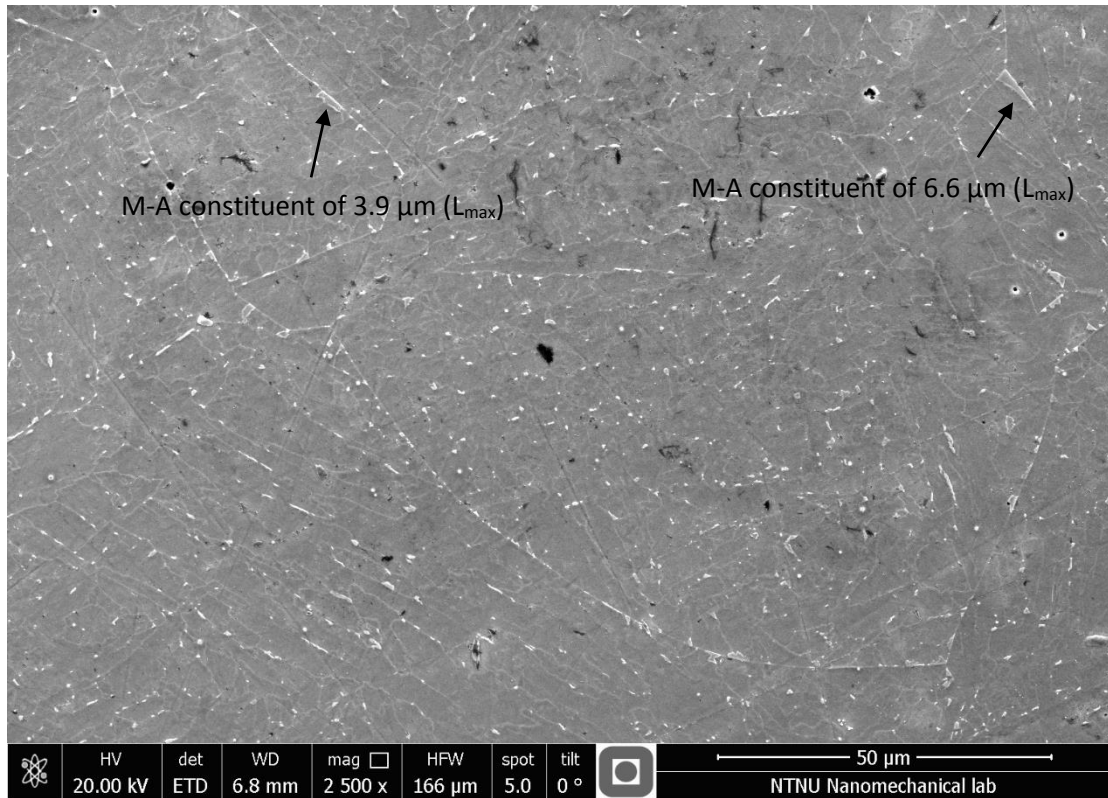


Figure 40 - SEM micrograph of sample 7 (CGHAZ 15), close to the fracture surface. LePera etched for approx. 20 sec.

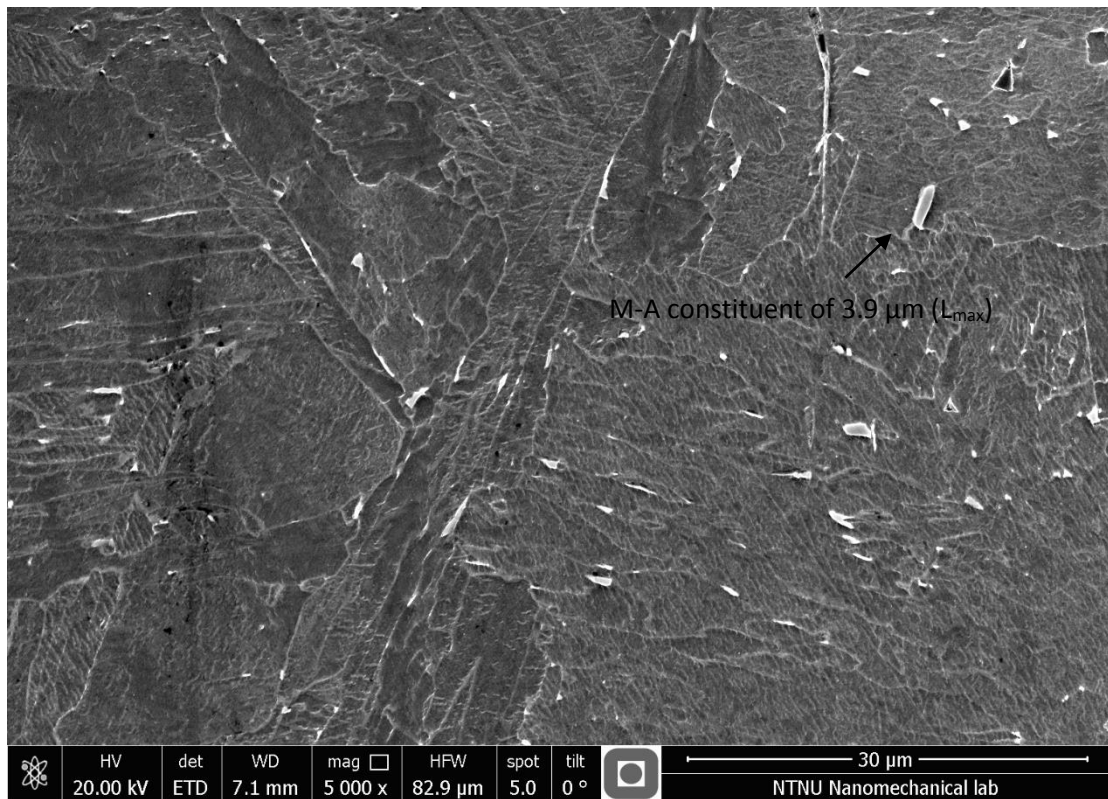


Figure 41 - SEM micrograph of sample 12 (ICCGHAZ 15), close to the fracture surface. LePera etched for approx. 20 sec. (High magnification).

### 5.1.3 VICKERS HARDNESS

The Vickers hardness measurements are summarized in Table 7. The measurements are taken on the grinded, polished and etched surface, around 1 mm from to the fracture surface. Measurements taken around 5 mm from the fracture surface are at around  $190\pm 10$  HV, with a standard deviation around of 15 for all samples.

Table 7 – Vickers hardness results

Sample	HV	Standard deviation
24 (ICCGHAZ 10)	239.2	10.67
7 (CGHAZ 15)	234.4	20.03
17 (CGHAZ 10)	232.0	10.35
31 (CGHAZ 5)	231.4	12.92
18 (CGHAZ 10)	231.2	18.78
36 (ICCGHAZ 10)	228.1	14.05
12 (ICCGHAZ 15)	225.8	11.58

### 5.2 FRACTURE TOUGHNESS AND AE SIGNALS

The fracture toughness result in this section is both from the testing SINTEF conducted in 2014 and 2015 regarding the 420 MPa steel plate from Ruukki. Figure 42 summarizes the test result from 2014 (SENB05 at  $-60$  °C) while Figure 43 summarizes the test result from the SENB05 testing in 2015. For the samples with a high CMOD value, these were interrupted before final fracture, the rest of the samples went to final fracture. Corresponding tables are found in the appendix.

The values are given in CMOD (Crack Mouth Opening Displacement), and not the common fracture toughness parameter CTOD (Crack Tip Opening Displacement) because the software that register the AE signals and the corresponding CMOD and load is not in compliance with the load-displacement curve plotted in parallel with the AE data. More information about this is found in Larsen's thesis. The fracture toughness values from the screening report are the corresponding CTOD values to Figure 42.

In general, samples with high CMOD have a higher amount of AE signals than for samples with low CMOD, especially for low temperatures. For the test run in 2014, the highest CMOD value for samples without a AE signal was 1.01 mm, and for 2015 this number was 0.82 mm. Sample 18 (CGHAZ 10) had the highest amount of AE signals with 13, and sample 134 (CGHAZ 25) had the next highest amount with 12. As seen in Figure 44, most of the AE signals for samples with more than two AE signals are at the peak of the load displacement curve and with decreasing load values.

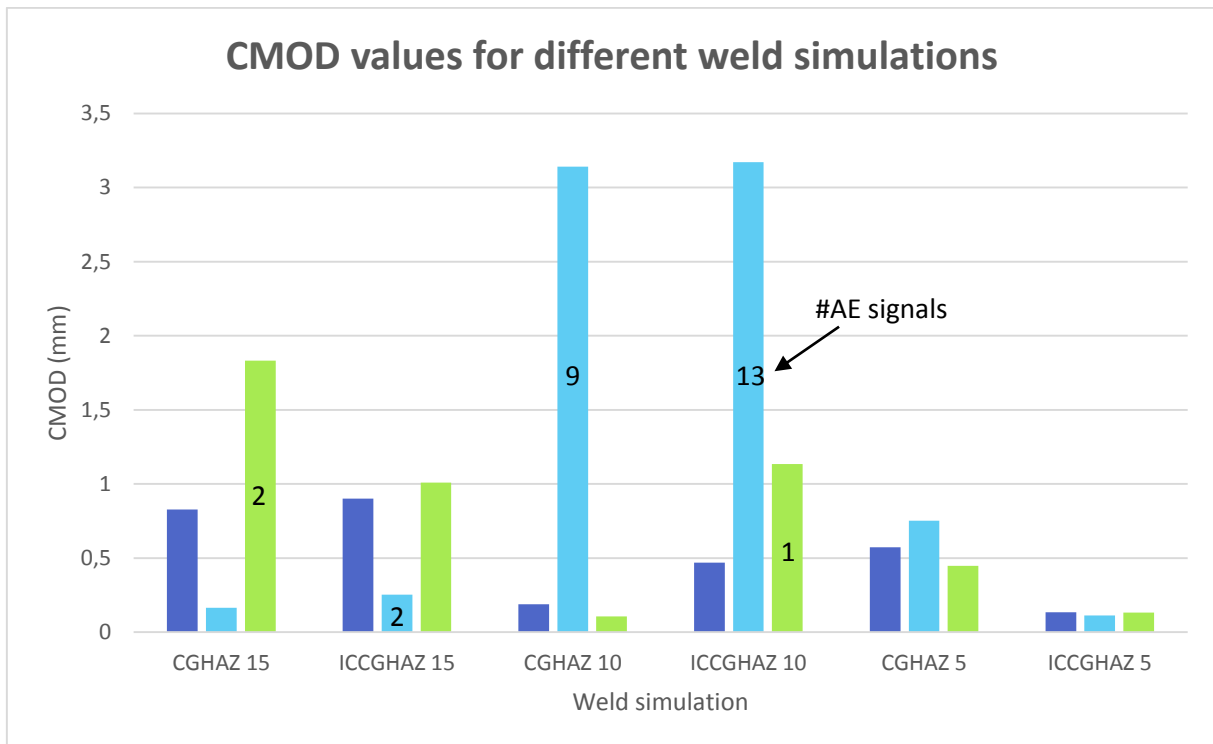


Figure 42 – CMOD values for the different weld simulations from the 2014 testing, the number of AE signals are marked at the corresponding sample. Samples without valid AE signals have no number.

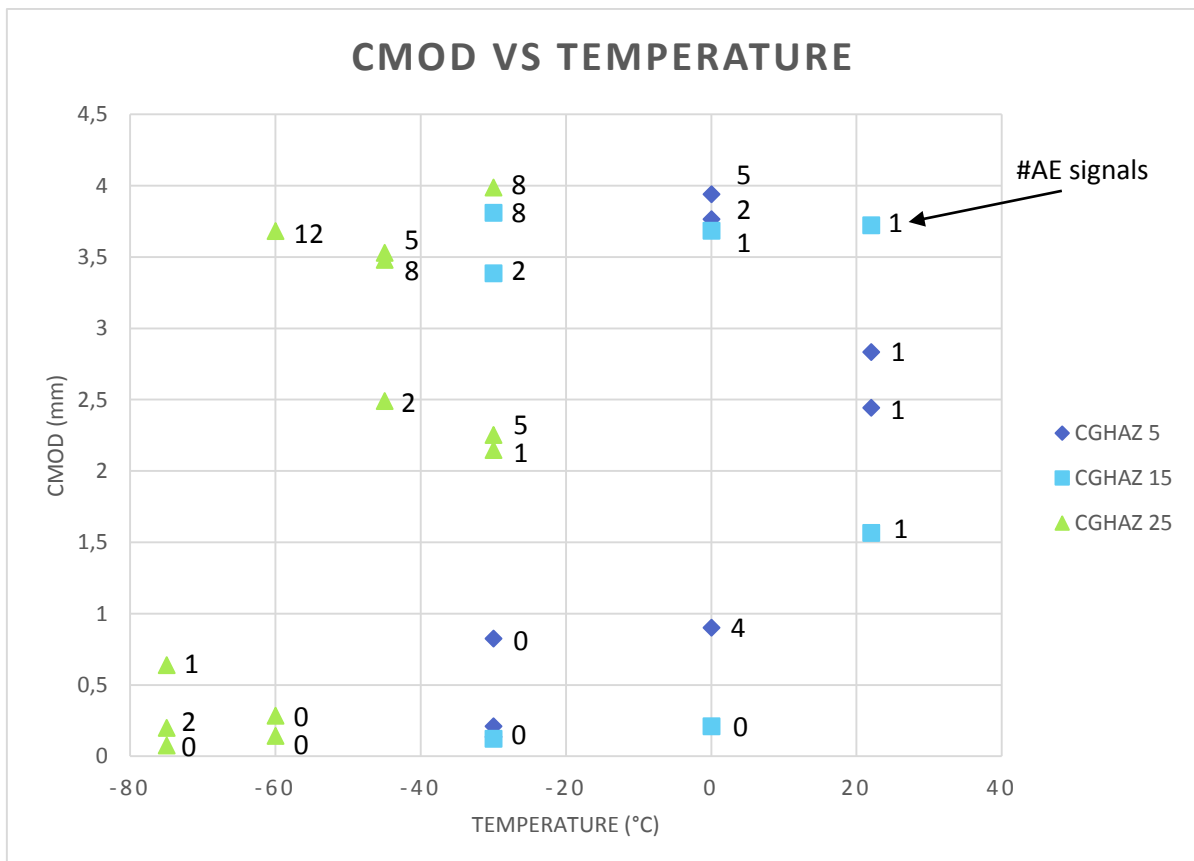


Figure 43 – CMOD vs temperature for fracture mechanics testing in 2015 on SENB05. The number of AE signals are marked at the corresponding sample.



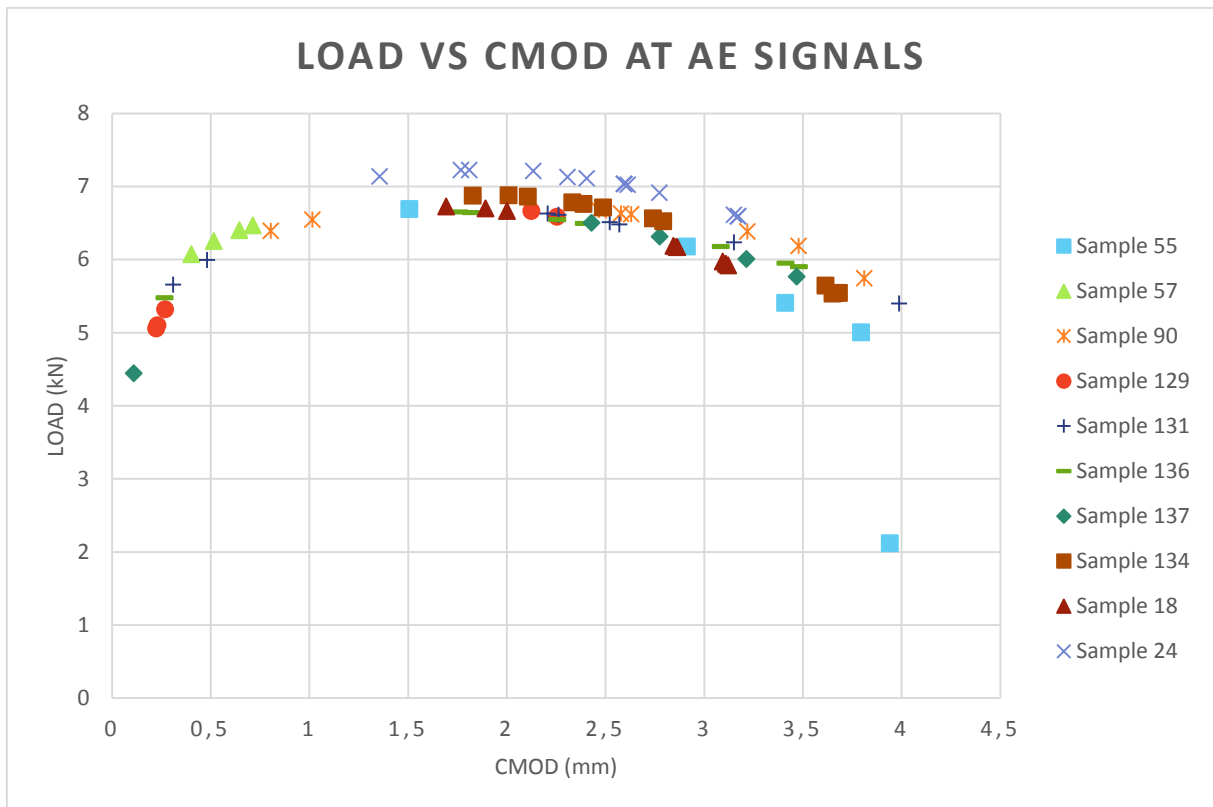


Figure 44 – Load vs CMOD at AE signals for samples with more than two AE signals

### 5.2.1 SIZE OF THE ARRESTED MICROCRACK

The predicted size of the microcrack related to the AE signal amplitude was calculated using the exponential trend line generated by excel from the original values from Østby et al. (2012). The equation from the trend line and the expected microcrack sizes from this is seen Figure 45. The samples chosen in the plot have all one of the amplitudes over 80 dB, i.e. at least one expected arrested microcrack of more than approximately 50  $\mu\text{m}$ . All of the samples not seen in the plot has AE signal amplitudes under 80 dB.

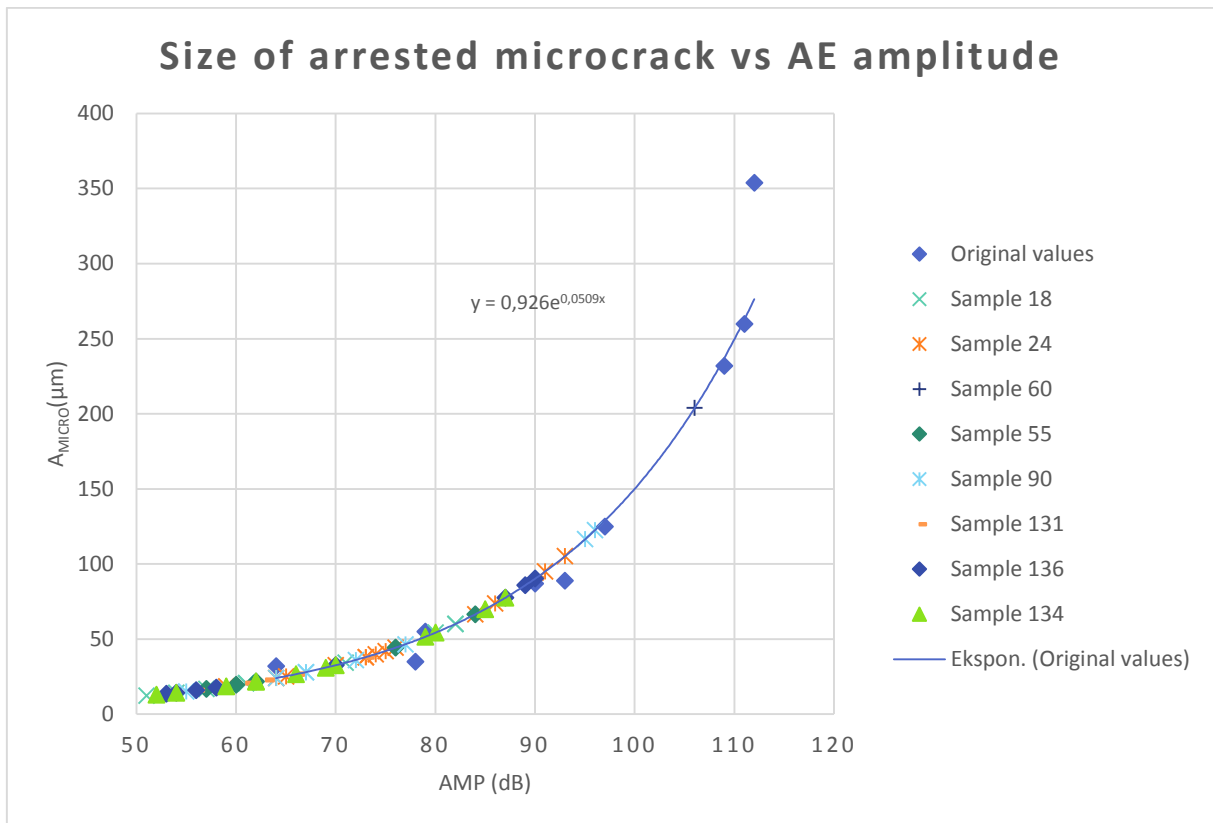
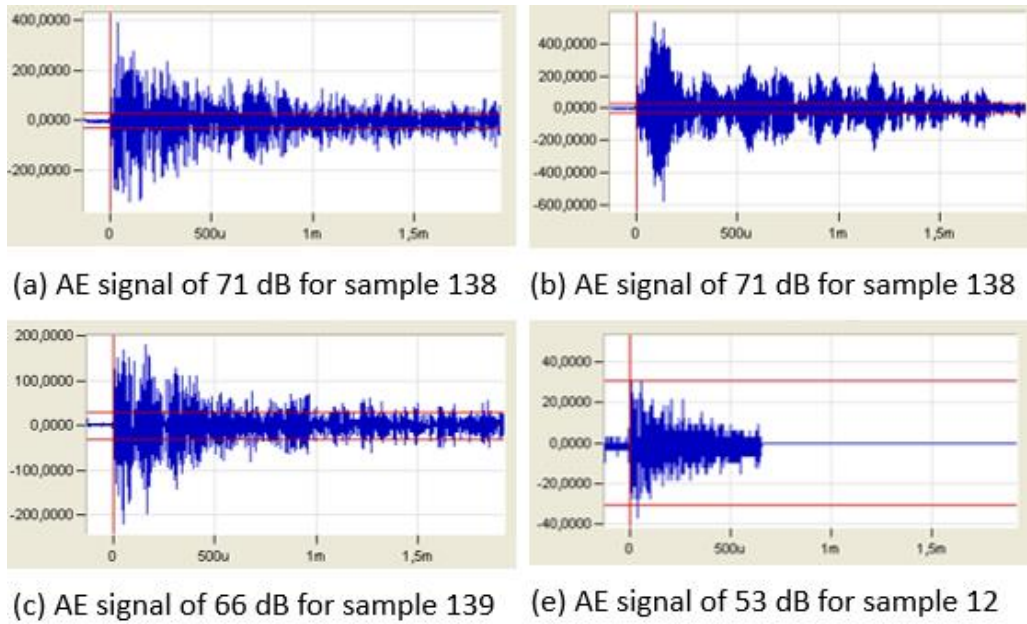


Figure 45 – Prediction of the size of arrested microcrack, using Østby et al. (2012) model

### 5.2.2 SHAPE OF AE SIGNAL

The samples in Figure 42 and Figure 43 that have AE signal at low CMOD values are further investigating in relation to the shape of the AE signal. For CGHAZ 25, these are sample 138 (2 AE signals) and sample 139 (1 AE signal) and for ICCGHAZ 15 this is sample 12 (2 AE signals). The AE signal for these are shown in Figure 46. The other AE signal for sample 12 is similar to the one in the figure. The AE signals for sample 57, which was also investigated, seemed to have the typical “burst” shape. This sample correspond to the lowest CMOD value for CGHAZ 5 with valid AE signals.



*Figure 46 – Shape of AE signals*

### 5.3 FRACTURED SAMPLES (RUN TO FINAL FRACTURE)

A screening of the fracture surfaces on the samples run to final fracture was conducted to get an impression of the fracture surfaces and relate it to AE signals and CTOD.

The number of AE signals vs CMOD for the samples conducted fracture surface screening on is shown in Figure 47. As seen, sample 24 is the most ductile, i.e. highest CMOD, followed by sample 18, 129, 7, 49, 31, 139, 12, 138, 91 and 36 as the least ductile sample (corresponding weld simulation and test temperature for these samples are found in the tables in the appendix). This complies approximately with the fracture surfaces for all samples except sample 18 and 31. Sample 18 has a low amount of dimples associated with ductile fracture before the cleavage facets, while sample 31 has many dimples before the cleavage facets. Most likely, the samples have been incorrectly marked, as sample 18 would fit with the ductility of sample 31. Further conformant of this is that sample 18 which was conducted microstructure analysis contained a lot of plastic deformation.

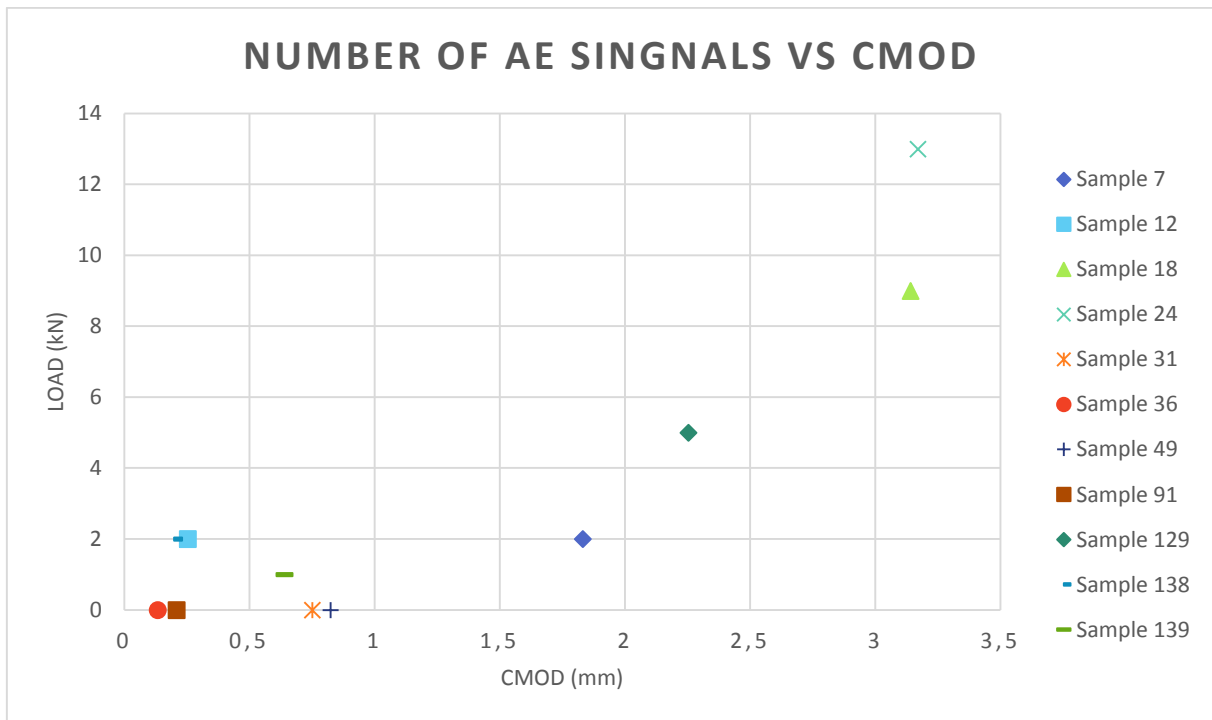


Figure 47 – Number of AE signals vs CMOD for screening samples

There is not many AE signals for the samples, i.e. not a lot of microcrack nucleation (Østby et al., 2012). It is difficult to determine the number of initiation sites on the fracture surface as all of the sample have connected cleavage facets. A detailed study is not conducted, thus distinguishing the different amounts of initiation sites related with the number of AE signals on the samples is not possible. However, an interesting relation to AE is the CTOD in which the signal was emitted. For sample 129, 24 and 18 (assumed to be sample 31 in the fracture surface investigation), the CMOD values, and the expected corresponding CTOD values for these that gave AE signals, was within the ductile area of the fracture surface. The AE signals for these samples were varying from 51 to 93 dB. This will be discussed further later. Fractograph of sample 24 is found in the appendix, in addition to the fracture surface of sample 138, to illustrate the difference for a very brittle fracture.

One of the AE signal emitted related to CTOD for sample 7 (CGHAZ 15), could indicate that it is a cleavage microcrack initiation. This was one of the most studied samples, and there were only found two distinct initiation sites as these two are the only found initiation sites with river marks originating from the sites and growing in all directions. These initiation sites is shown in Figure 49 and Figure 51. The initiation site in Figure 49 is located 470  $\mu\text{m}$  away from the pre-test fatigue notch. Thus, this could be related to one of the AE signals. However, there is no way of determining which one it is, and where it arrested in regards to the amplitude of the AE signal. Relating the AE signal amplitude to Østby et al. (2012) model, the arrested microcrack area should be 2704  $\mu\text{m}^2$  if the AE signal was 79 dB and 625  $\mu\text{m}^2$  if the AE signal was 64 dB. The rectangle in the figure illustrate the micro crack area if the related AE signal was 79 dB.

The initiation site in Figure 51 is located mid-section of the fracture surface, approximately 1.2 mm away from the pre-test fatigue notch. Thus, this is most likely not related to the one of the AE signals because the measured CMOD at these signals was at 1.57 and 1.63 mm giving a much smaller CTOD than 1.2 mm. The initiation site was therefore most likely the final fracture leading to an AE signal of more than 113 dB. All of the fracture surfaces had a lot of secondary cracks. This can be seen in Figure 51 for a small arrested secondary crack and in Figure 48 for a big secondary crack.

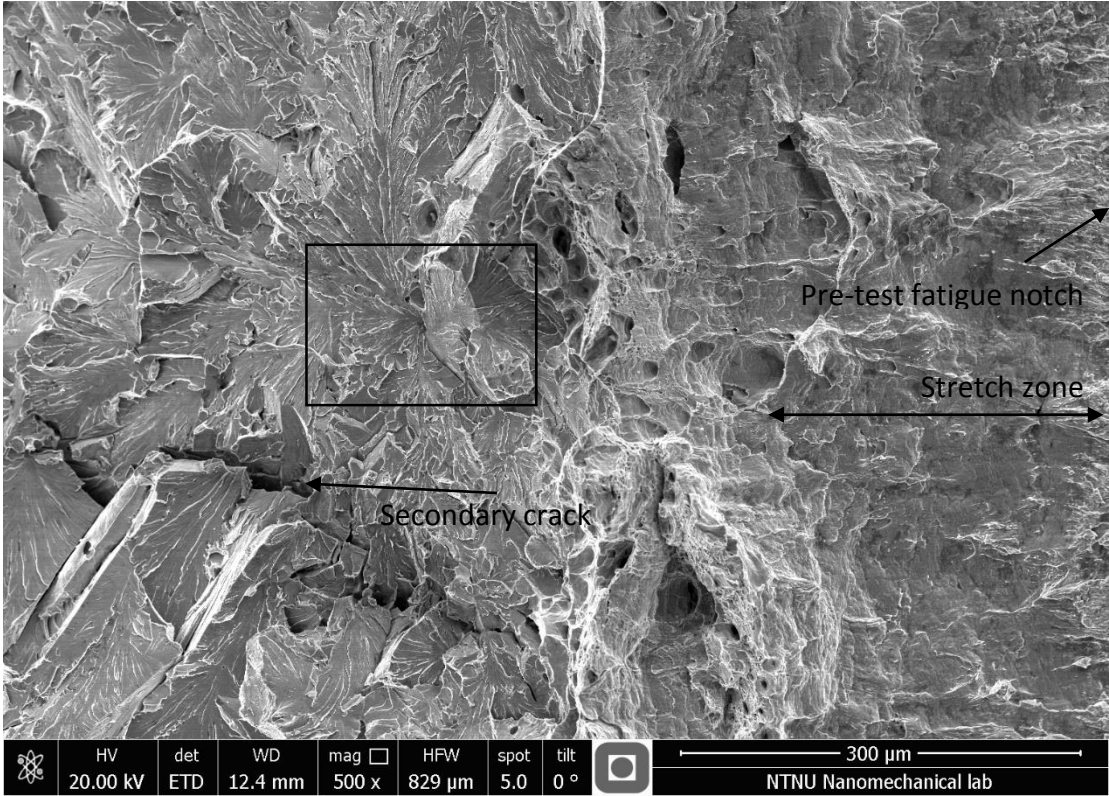


Figure 48 – SEM fractograph of sample 7 (CGHAZ 15), indicating crack initiation 470 μm from the pre-test fatigue notch. Approx. located little under the mid-section of sample the sample.

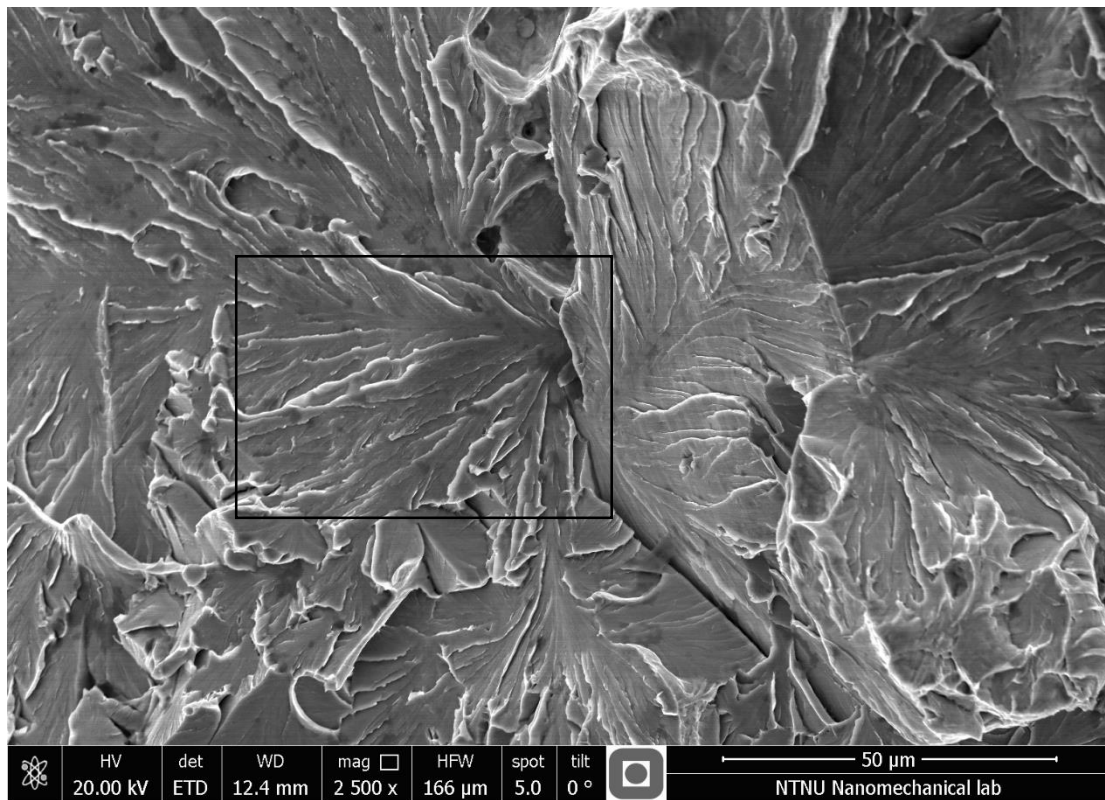


Figure 49 – SEM fractograph of sample 7 (CGHAZ 15), close-up of the marked area in Figure 48. The marked area in this figure indicate the facet area that would relate to the biggest AE amplitude from the sample.

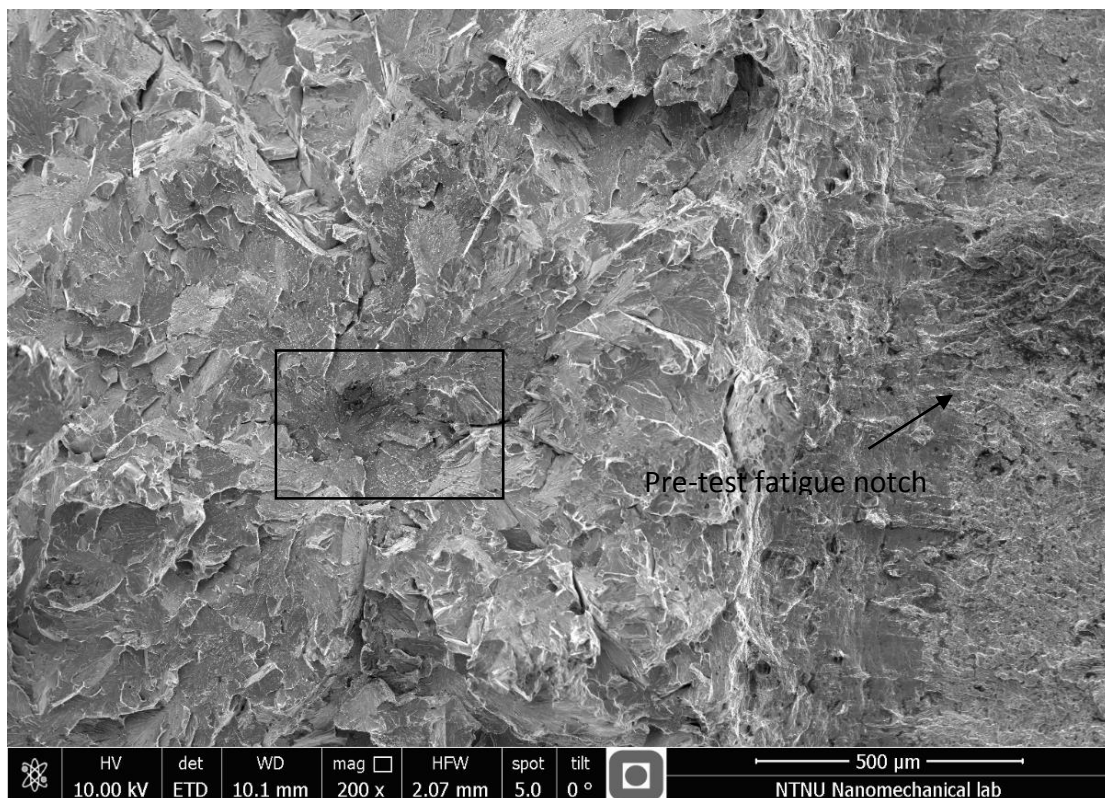


Figure 50 – SEM fractograph of the middle section of sample 7 (CGHAZ 15)



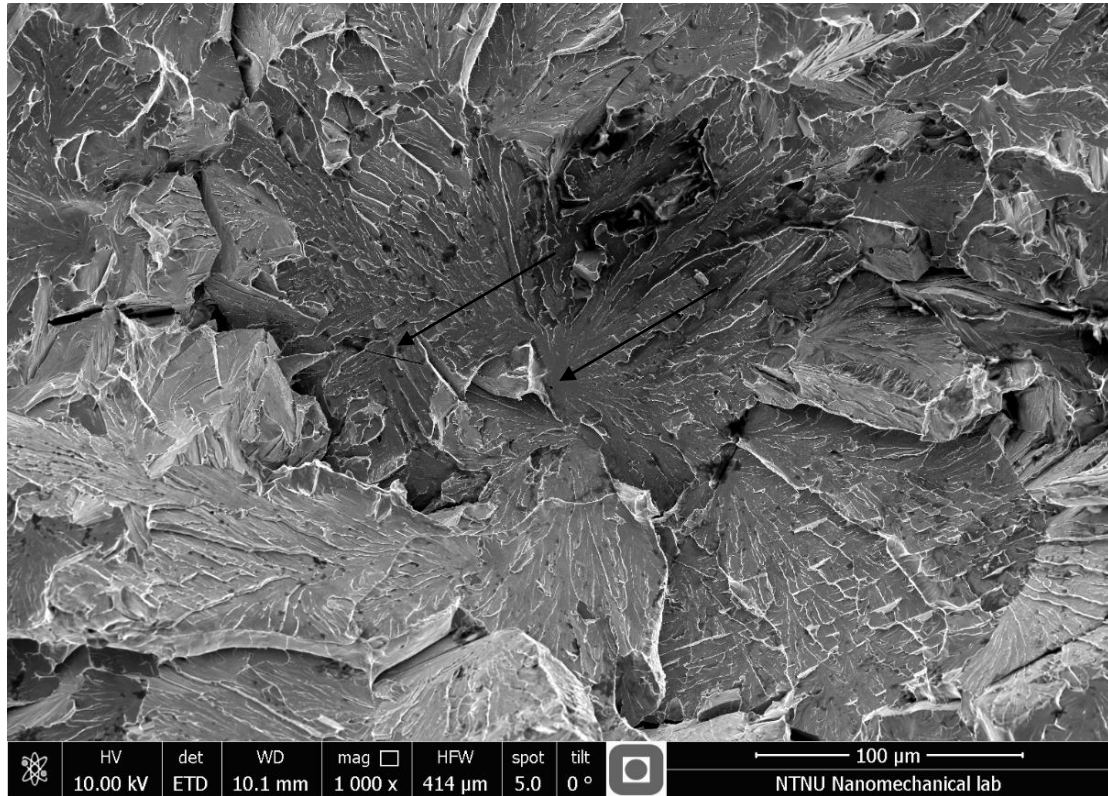


Figure 51 – SEM fractograph of sample 7 (CGHAZ 15), close-up of the marked area in Figure 50. Arrows indicating secondary crack and initiation site.

#### 5.4 INTERRUPTED SAMPLES

Only one interrupted sample gave a valid and good AE signal. Some gave a valid AE signals in regards to the filtering conditions, but were not investigation due to it most likely being very difficult to find the cleavage facet. This concerns samples with a high CMOD or a low AE signal amplitude. Sample 126, 180, 217 and 339 was investigated in spite of having a low amplitude or high CMOD, in order to have some investigation on interrupted samples. Table 8 show the AE results, with all values being at the amplitude in which the test was stopped. The CTOD value are calculated by Larsen, more information about CTOD is given in his thesis.

Table 8 – AE results interrupted samples

Sample	Test temp. (°C)	Load (kN)	CMOD (mm)	CTOD (mm)	Amp (dB)
<b>126 (CGHAZ 15)</b>	- 30	6.24	2.02	0.58	87
<b>167 (CGHAZ 5)</b>	- 30	2.89	0.06	0.01	112
<b>180 (CGHAZ 15)</b>	- 60	6.30	0.48	0.14	64
<b>217 (ICCGHAZ 5)</b>	- 60	3.46	0.09	0.01	66
<b>339 (ICCGHAZ 15)</b>	- 45	4.10	0.09	0.02	64

A difficulty appeared when investigating these fracture surfaces. Only sample 167 had the characteristic cleavage facet, and for all samples, a varying amount of flat areas was observed on the fracture surface, both in the pre-test fatigue notch and after. Figure 52 shows a great

amount of these flat areas closely spaced just after the pre-test fatigue notch. This is from sample 180 (CGHAZ 15), which contained around ten to fifteen flat areas after the notch. This seemed to be more than for the other samples. The flat areas varied from around 10  $\mu\text{m}$  to 150  $\mu\text{m}$  in size for all samples, and were usually less densely spaced than seen in Figure 52. There were also found a flat area on sample 138, 139 and 91, which are non-interrupted samples. SEM fractograph of the flat are in sample 139 are found in the appendix.

The fracture surface on sample 180 (CGHAZ 15) got etched with nital to investigate any possible underlying microstructural features of the flat areas.

Figure 53 shows the area investigated after nital etching (picture is before etching). The nital etched sample in Figure 55 indicate that the microstructure under the flat area is bainite.

The reason for the flat areas will be discussed later. For now, they are taken as brittle cracks along slip-planes, thus would possibly give an AE signal as long as the crack is big enough. However, it is not possible to say with any certainty which flat area that was the source of the AE signal. To have a discussion about the flat areas related to AE amplitude, the first flat area of a sufficient size was taken as the source to the AE signals, and as the input to Østby et al. (2012) model. However, the stress and strain distribution in front of the pre-test fatigue notch is not homogeneous due to local stress and strain concentration, so the first initiating flat area could easily not have been the first after the notch.

Following is list of the first found flat areas, with corresponding fractographs in following:

- Sample 180: As this sample had a lot of flat areas, with many of them laying close to the notch, the uncertainty for this sample is very high. The flat area in Figure 56 is taken as the first flat area with a sufficient size. This is approx. 120  $\mu\text{m}$  from the notch.
- Sample 126: The first found flat area was found approx. 500  $\mu\text{m}$  from the notch, after lots of dimples, seen in Figure 58.
- Sample 167: In addition to the characteristic cleavage facet, a few flat areas of around 50  $\mu\text{m}$  were found close to the pre-test fatigue notch. Figure 59 and Figure 60 shows the cleavage facet, while Figure 61 shows some flat areas, just over the initiation in Figure 60.
- Sample 217: The flat area marked in Figure 62 seems to be the first area after the fatigue notch, and taken as the relation to the AE signal. This sample did however, have a big flat area on the fatigue notch tip which was not appearing on the opposite fracture surface, seen in Figure 91 in the appendix. The reason for this is not clear, thus



this is not regarded as a cleavage slip-plane and will not be taken in to account in relating to the AE signal.

- Sample 339: This sample had many flat areas at the notch tip or a few microns away. Figure 63 show some of these closely spaced. The biggest one in this figure is taken as the source to the AE signal, while noting that this is highly uncertain.

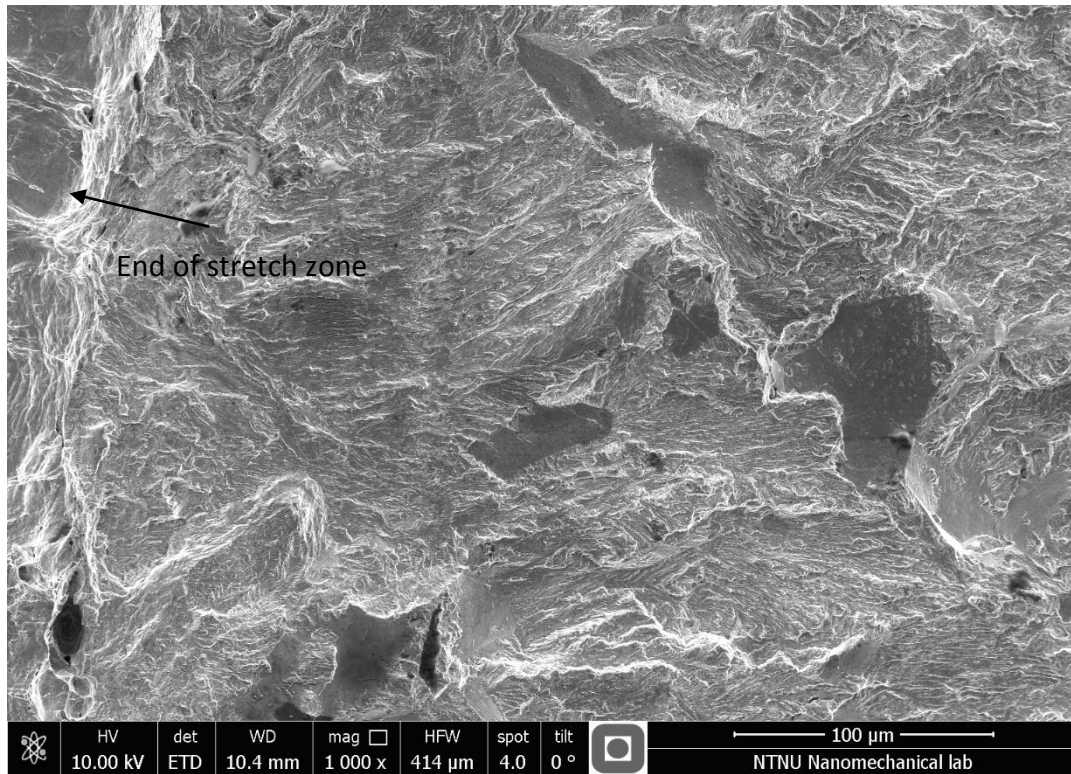


*Figure 52 – SEM fractograph of sample 180 (CGHAZ 15), showing flat areas just after the pre-test fatigue notch.*

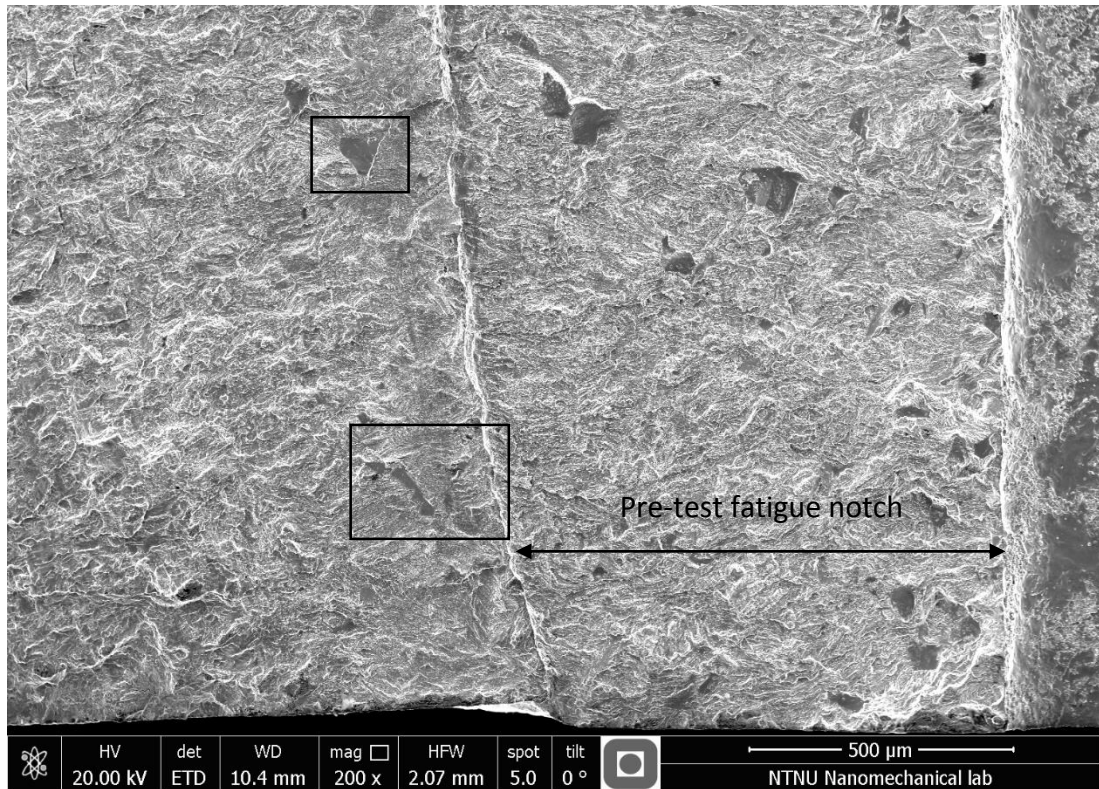


Figure 53 – SEM fractograph of sample 180 (CGHAZ 15), showing flat areas in both the pre-test fatigue notch and after. The rectangles are magnified in Figure 54 and Figure 56.

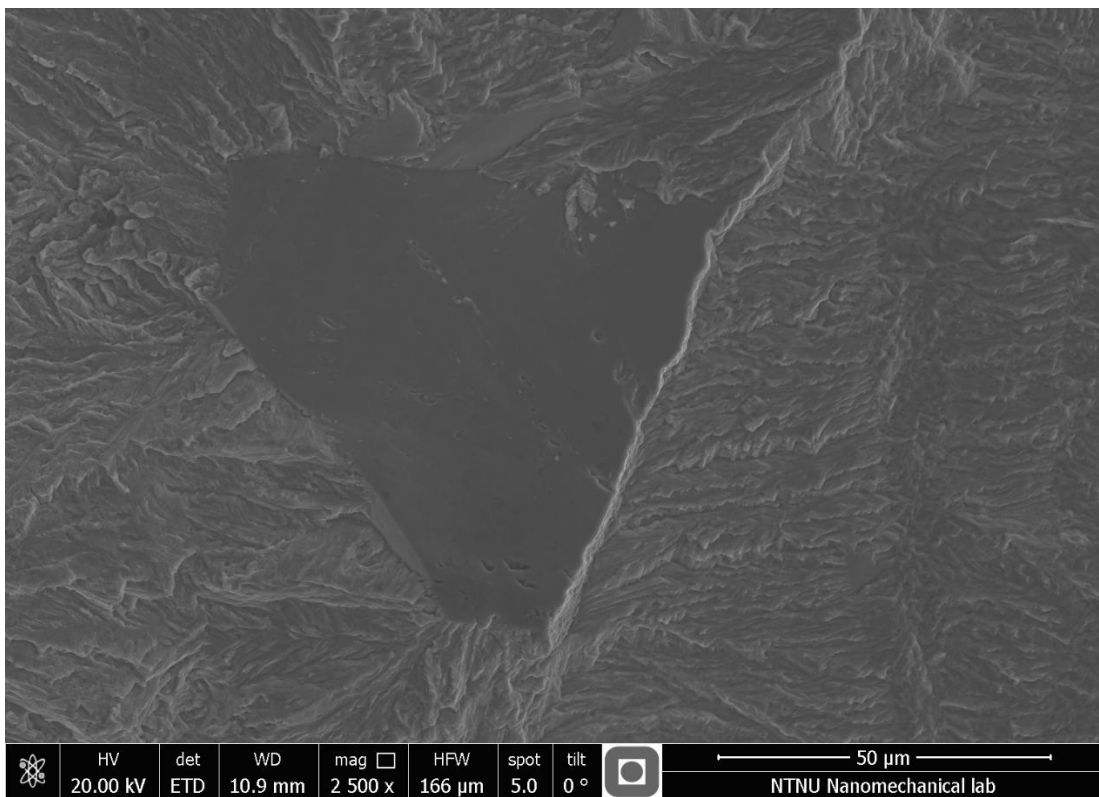


Figure 54 – SEM fractograph of sample 180 (CGHAZ 15), close-up of rectangle in Figure 53.

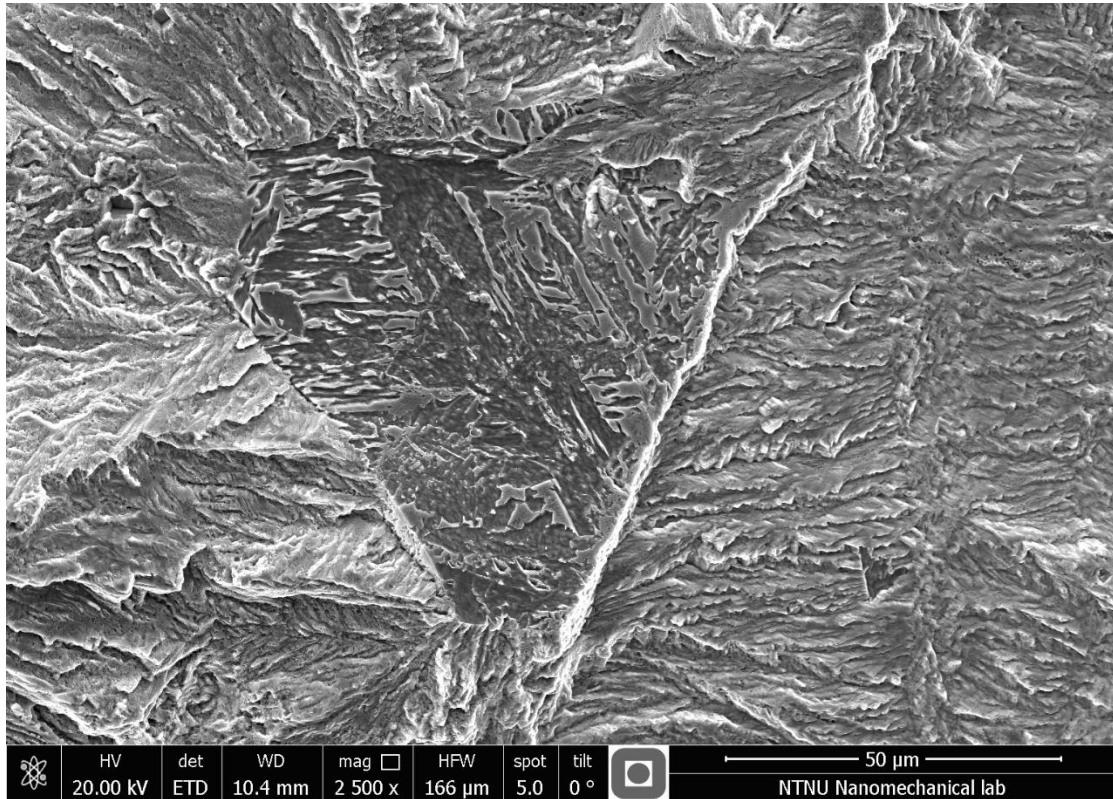


Figure 55- SEM fractograph of sample 180 (CGHAZ 15), same area as in Figure 55 etched with 2 % nital for approx. 10 seconds.

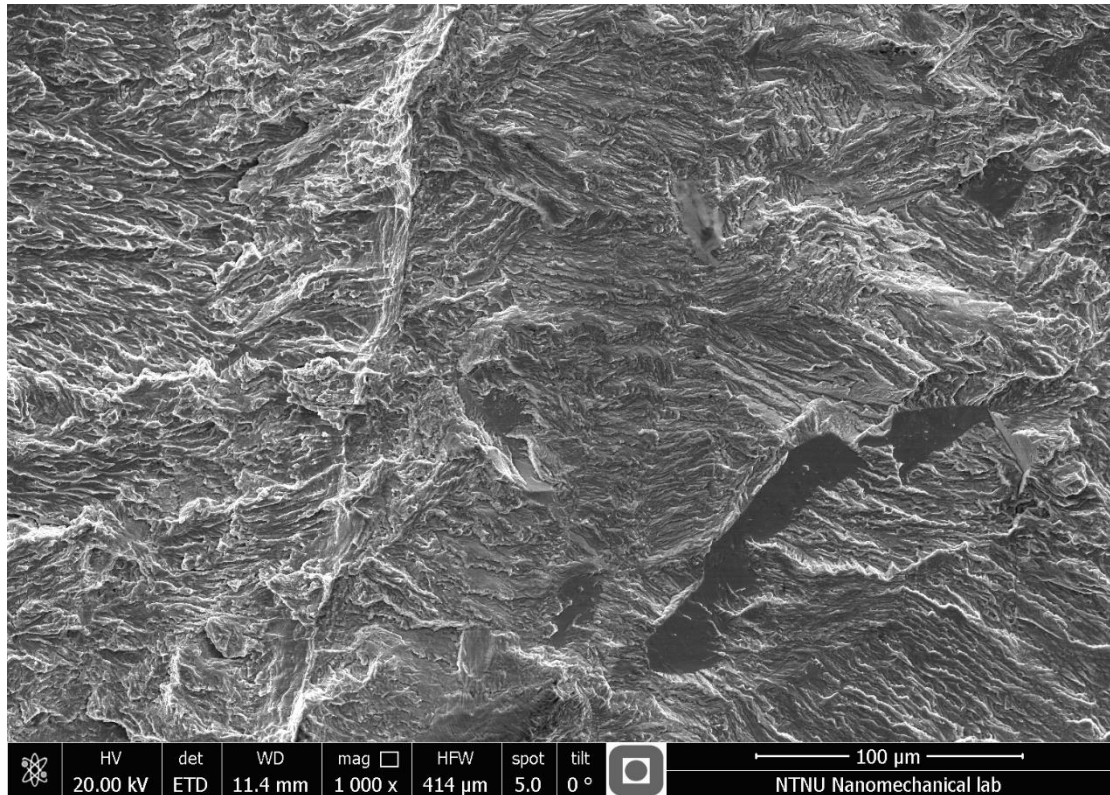


Figure 56 – SEM fractograph of flat areas in sample 180 (CGHAZ 15), the biggest is taken as the first sufficient size flat area after the notch. Close up of Figure 53.

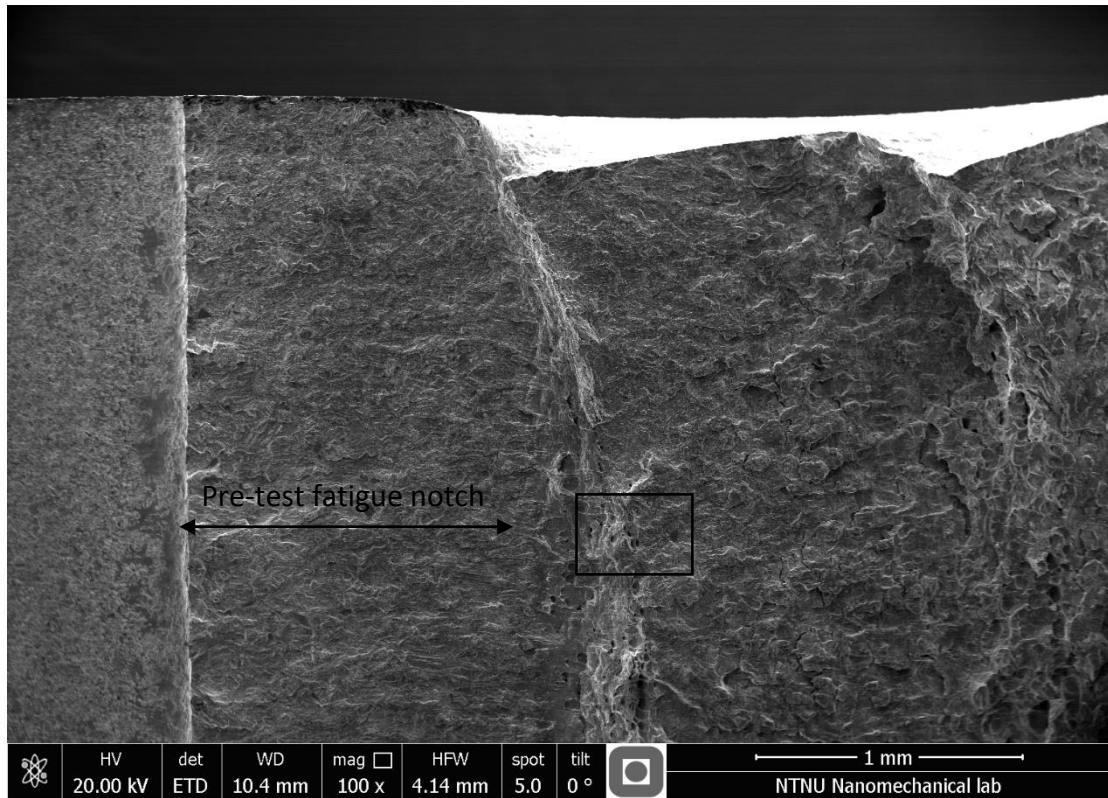


Figure 57 – SEM fractograph of edge of sample 126 (CGHAZ 15), overview

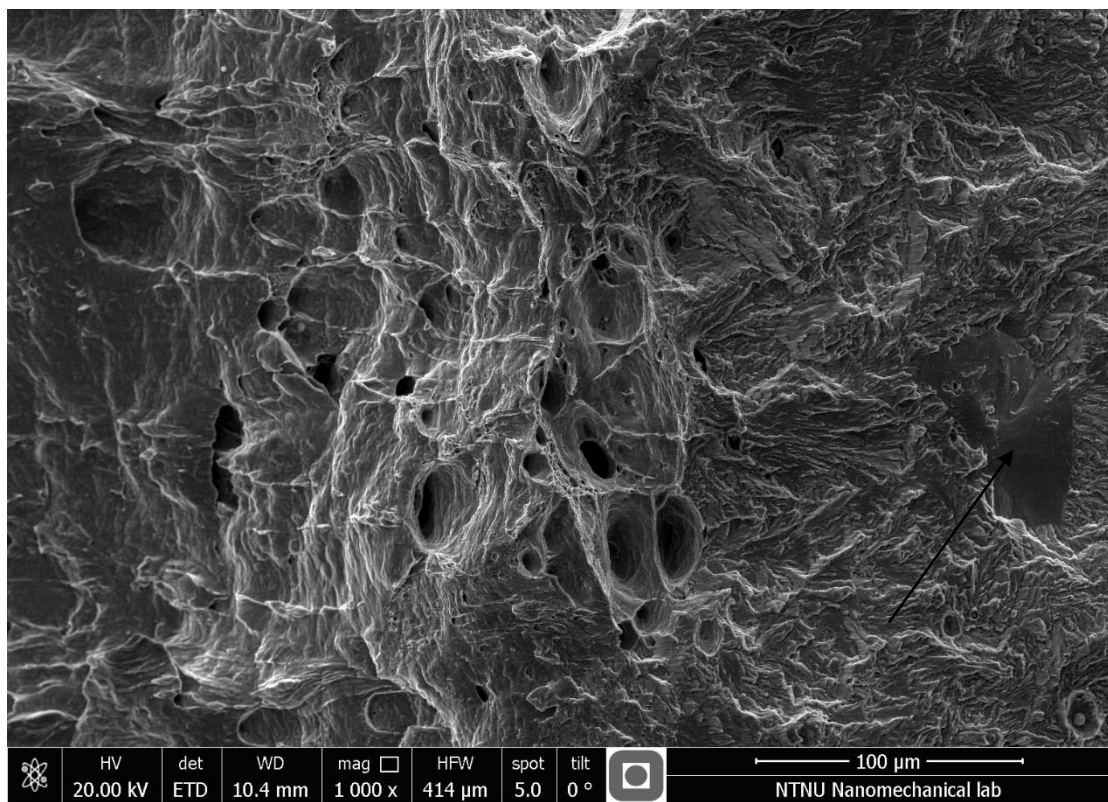


Figure 58 – SEM fractograph sample 126 (CGHAZ 15), close-up of rectangle in Figure 57, arrow indicating flat area



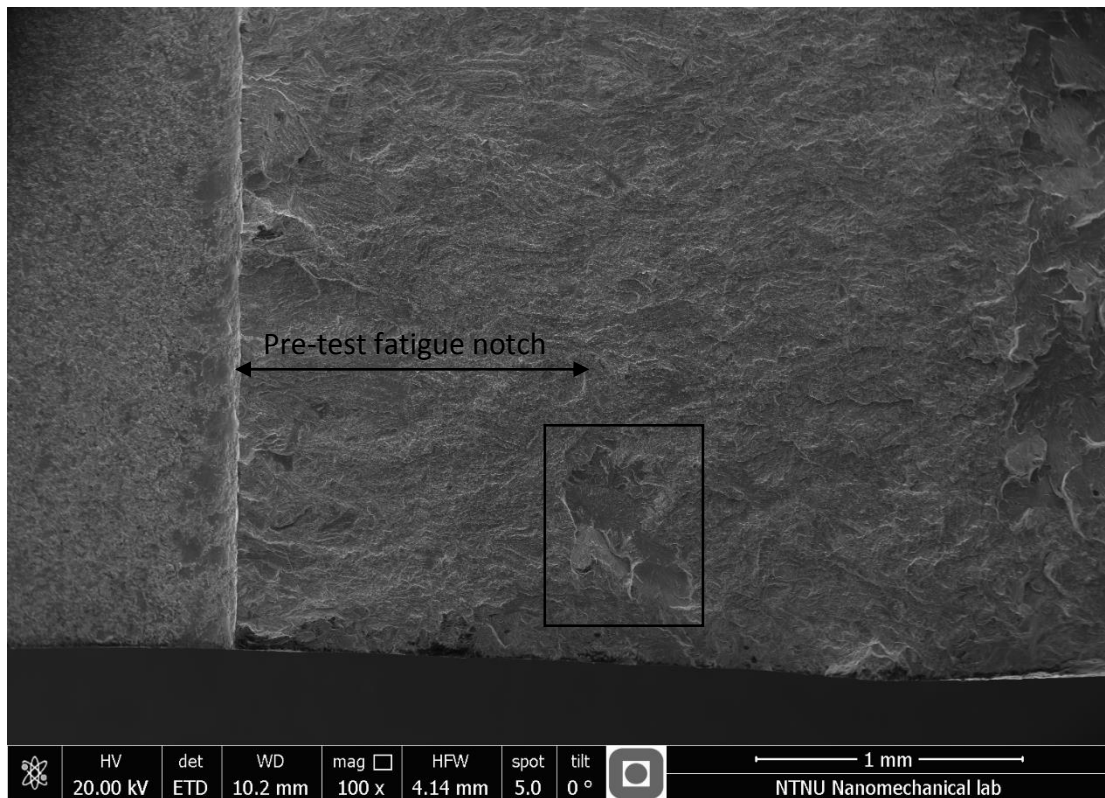


Figure 59 – SEM fractograph of crack initiation in sample 167 (CGHAZ 5), overview.

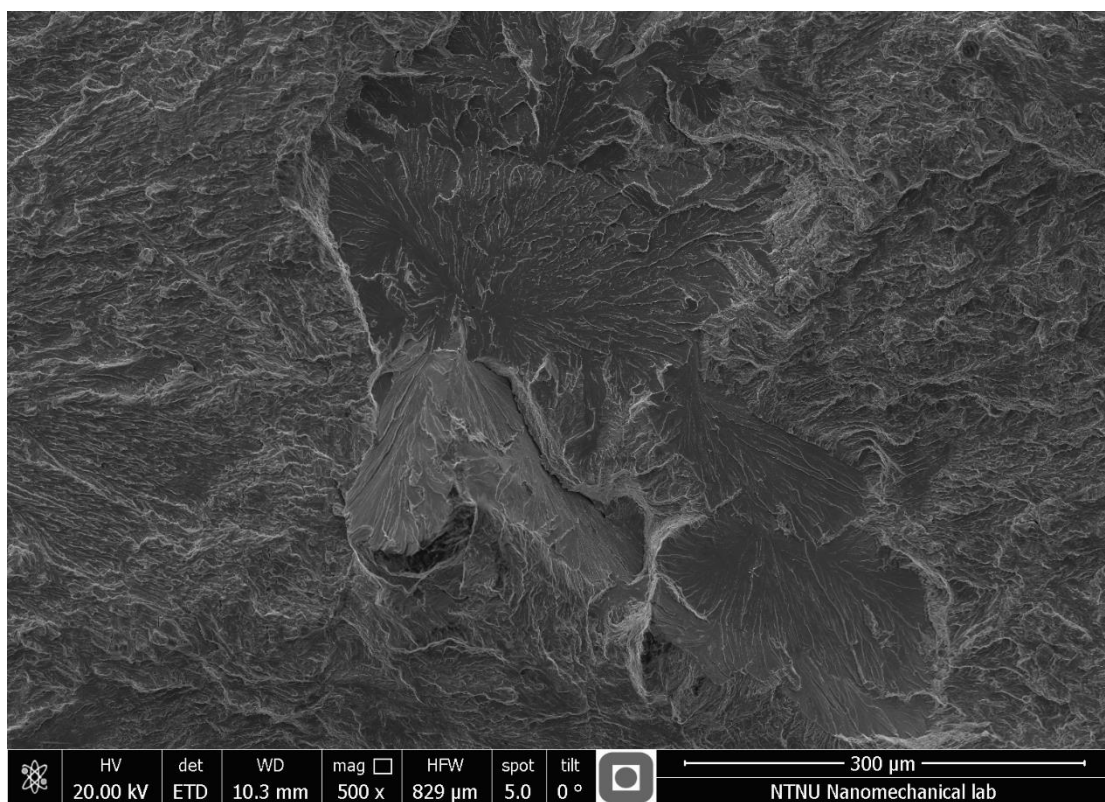


Figure 60 – SEM fractograph of crack initiation in sample 167, close-up of Figure 59

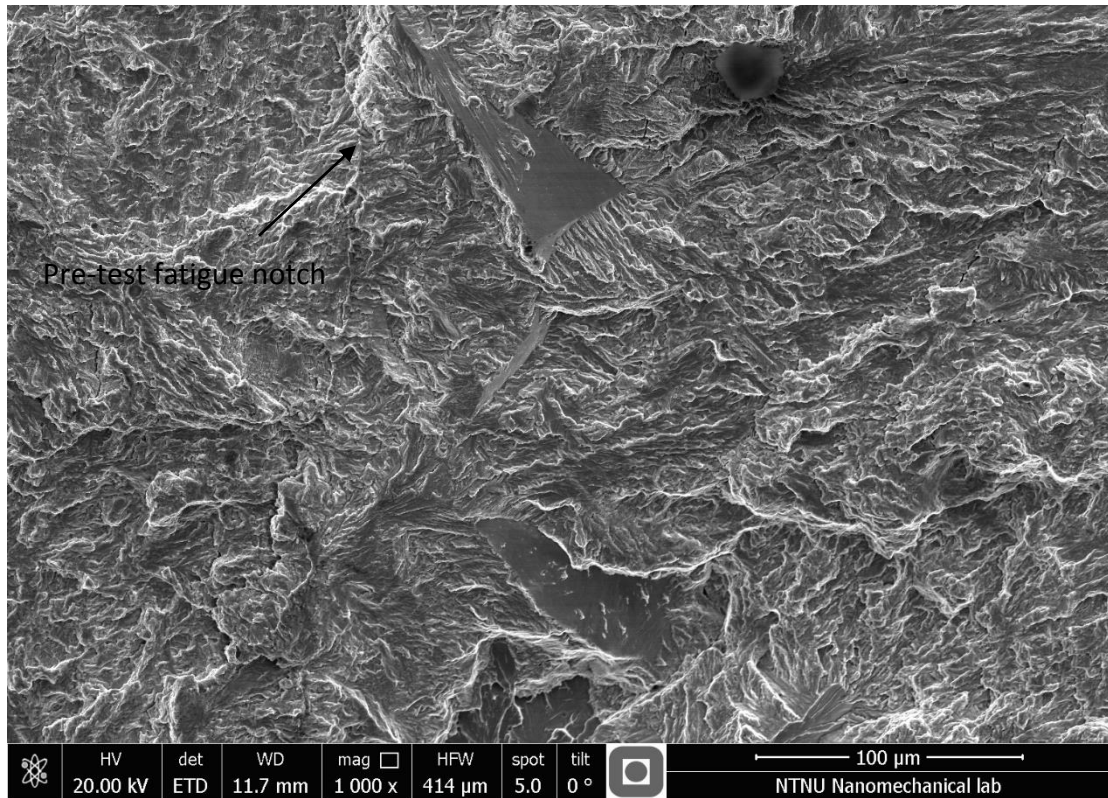


Figure 61 –SEM fractograph of flat areas in sample 167 (CGHAZ 5), just over the initiation in Figure 60.

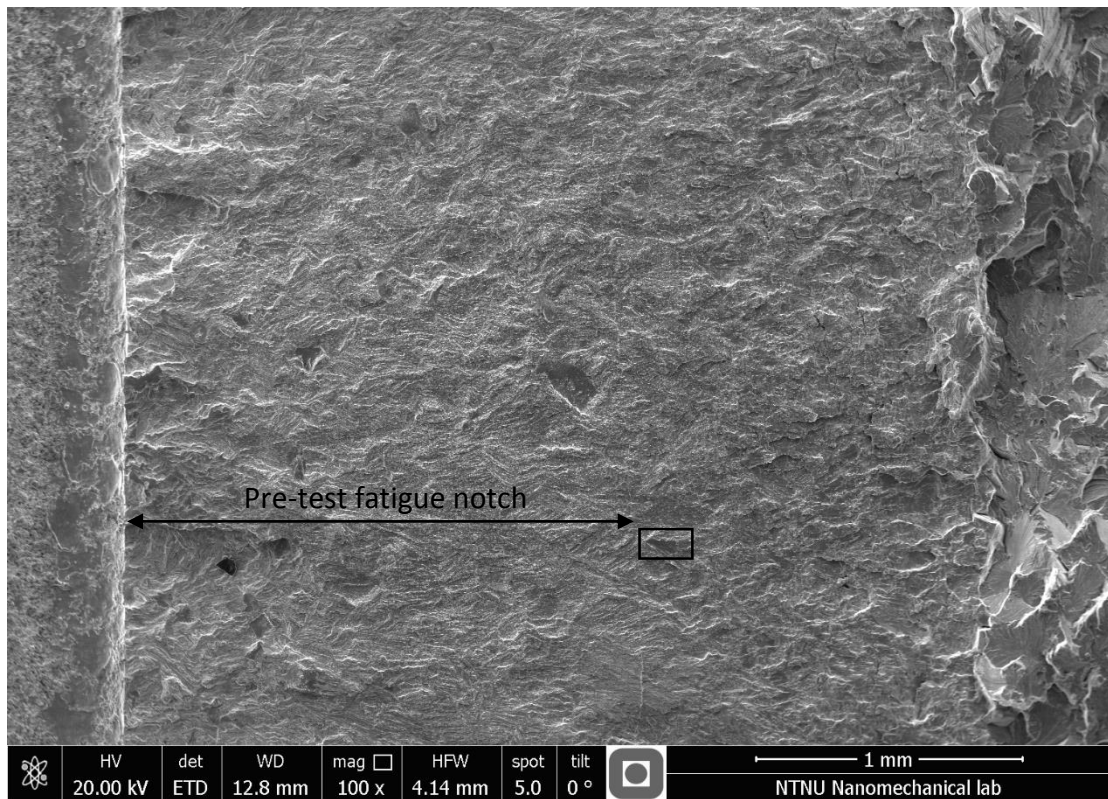
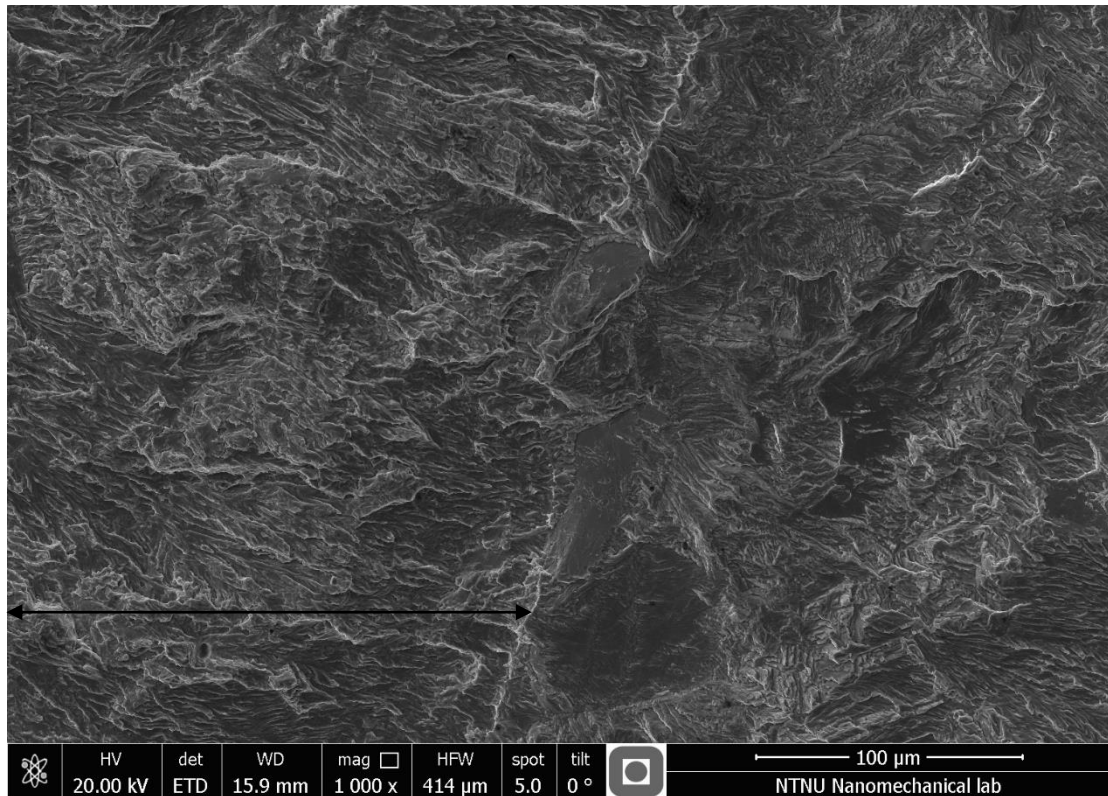


Figure 62 – SEM fractograph of sample 217 (CGHAZ 5), with rectangle indicating flat area related to AE signal.



*Figure 63 – SEM fractograph of flat areas in sample 339 (ICCGHAZ 15) at the pre-test fatigue notch. The biggest area is taken as the source to the AE signal. Arrow indication fatigue notch area.*

#### 5.4.1 CORRELATION BETWEEN AE AMPLITUDE AND ARRESTED MICROCRACK

The above flat areas and the characteristic cleavage facet in sample 167 are plotted in Østby et al. (2012) graph, seen in Figure 64. As seen, the flat areas scatter a bit from the curve, except from in sample 126, which have a higher certainty than the other samples in the correlation to the AE signal. Sample 167 show a very good correlation if only the first facet where the microcrack is believed to initiate is taken for sample 167. If the whole facet is taken, the deviation to the curve is large. The crack initiation site for sample 167 is believed to initiate at, or a few microns away from the pre-test fatigue notch.

Larsen had a different approach to the facet area for sample 167, in dividing the whole facet into the different grain orientations and adding the rectangular area of each. This showed also a good correlation to the graph.

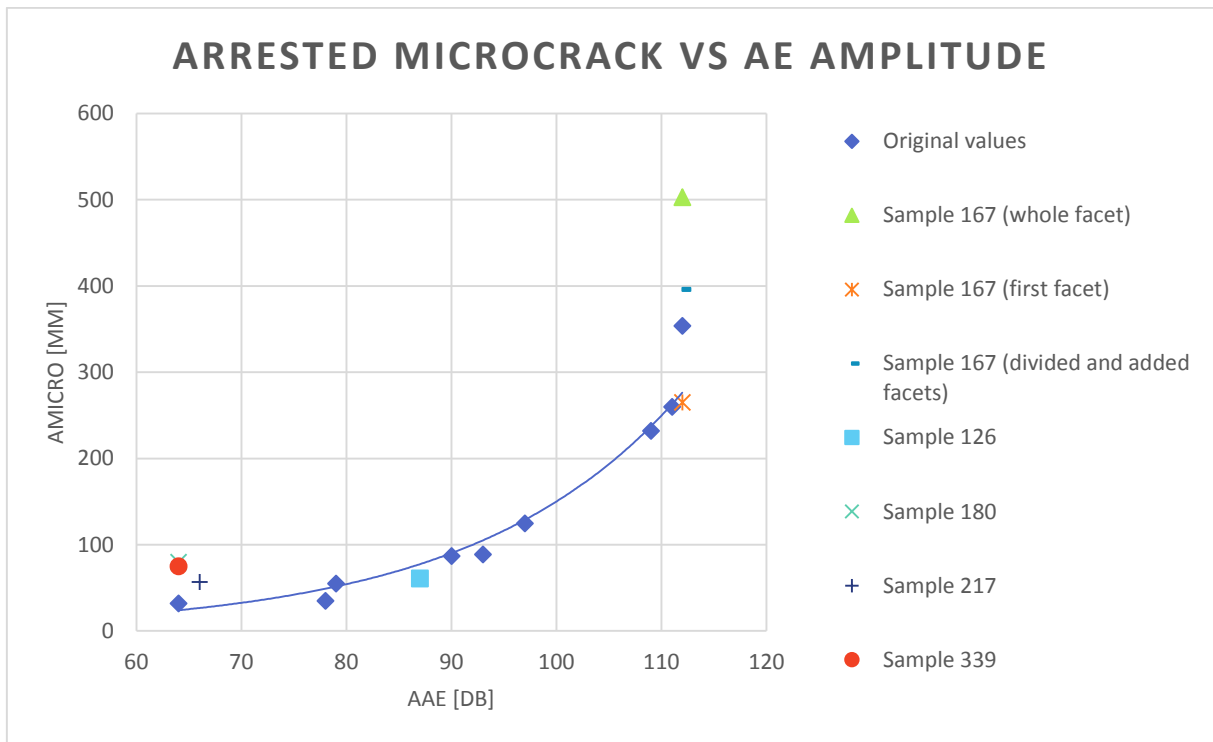


Figure 64 – Arrested microcrack vs AE signal amplitude

#### 5.4.2 CRACK INITIATION

Only for sample 167 (CGHAZ 5), which had the characteristic cleavage facet is it possible to say something regarding crack initiation. As the flat areas are very small relative to this facet, it is taken as the most likely initiation site of the sample. A high magnification fractograph of the believed initiation site on the facet are shown in Figure 65, with the opposite fracture surface of the same are shown in Figure 66. The figures show corresponding cracked particles, which are magnified in Figure 67. The believed initiation mechanism is discussed later.



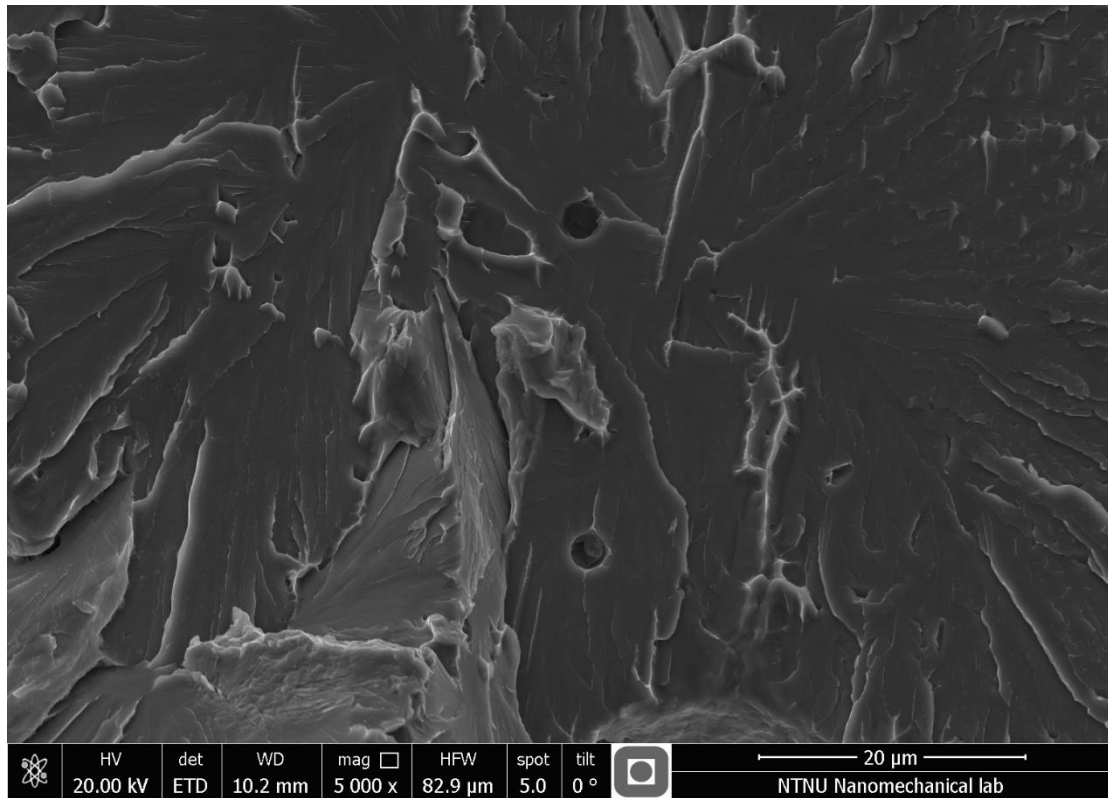


Figure 65 - SEM fractograph of crack initiation in sample 167, close-up of Figure 60

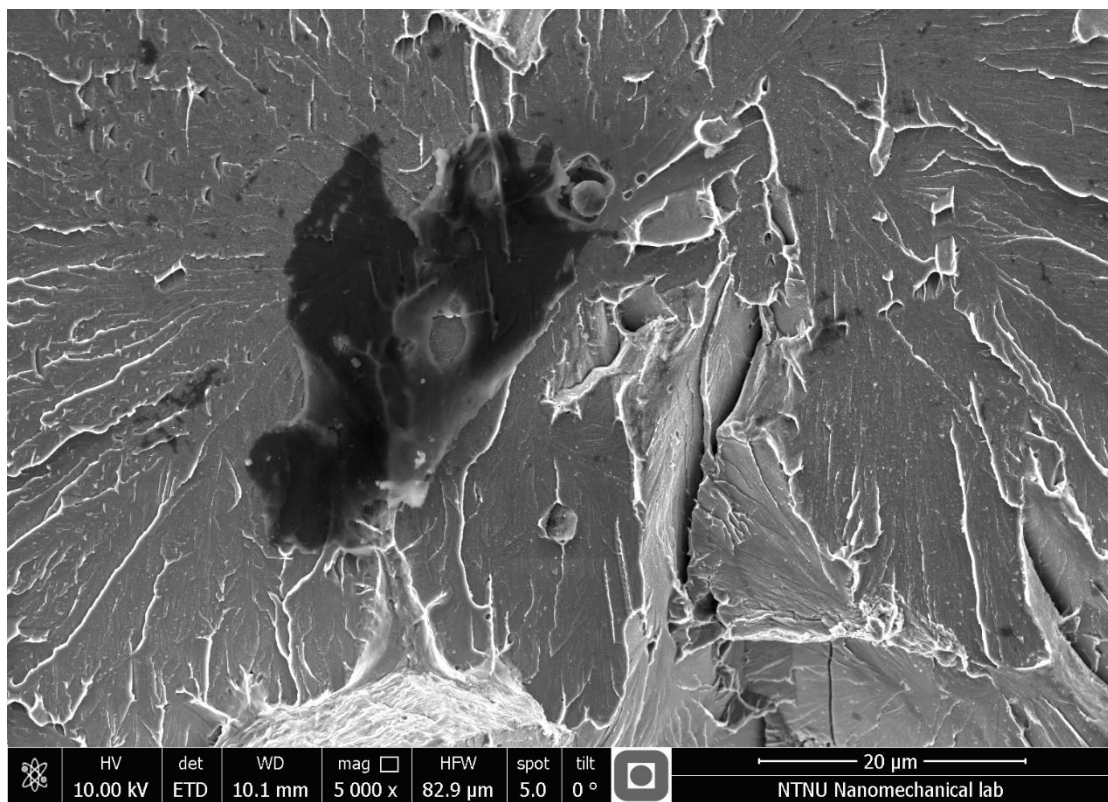


Figure 66 – SEM fractograph of the same crack initiation from the opposite fracture surface of Figure 65.

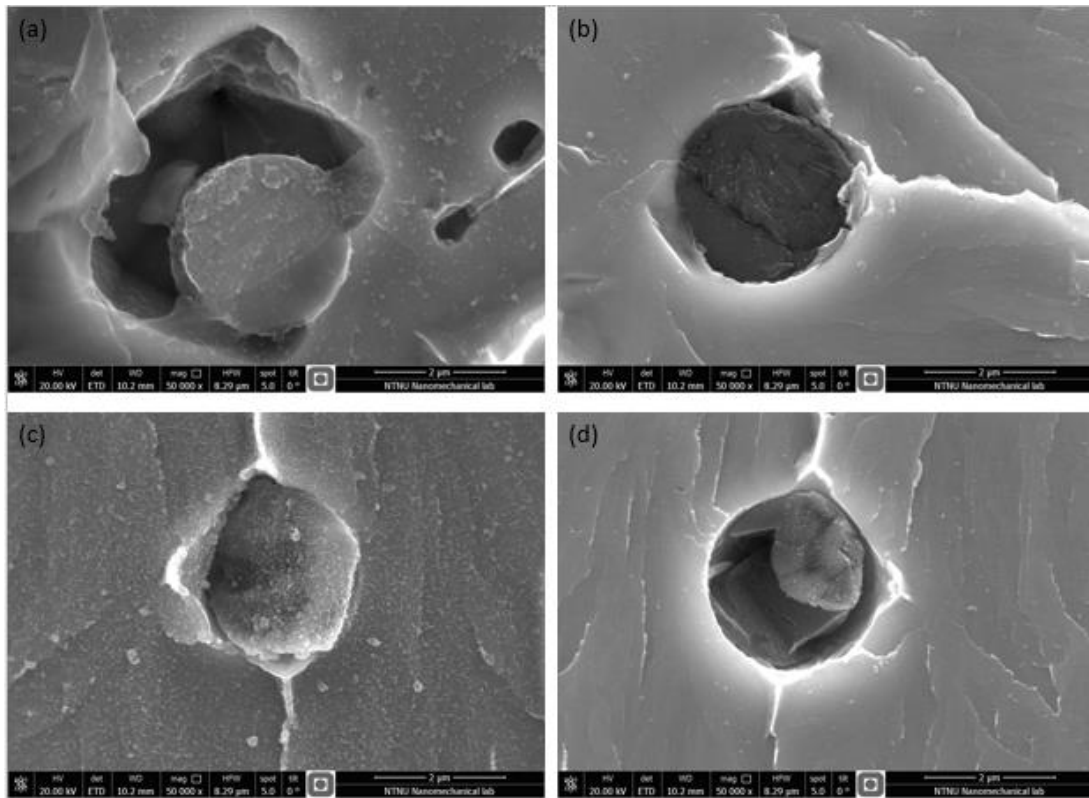


Figure 67 – SEM fractographs of the fractured particles in Figure 65 (b, d) and Figure 66 (a, c). The cracked particles are the opposite part of each other. The pairs are (a) and (b), and (c) and (d).

#### 5.4.3 INCLUSIONS

Several inclusion, both whole and cracked were found in all of the interrupted samples. These were also observed in the sample run to final fracture. An example are found in Figure 68 for sample 167, with the close-up of the particle shown in Figure 69. It seemed to have first cracked in the direction of the macro-crack, and then a secondary crack has gone straight through it without any difficulties. It was found 114 µm from the pre-test fatigue notch. Figure 70 show a cracked inclusion in an isolated dimple in sample 180 (CGHAZ 15) and Figure 71 show a cracked inclusion in sample 339 (ICCGHAZ), 80 µm and 20 µm after the pre-test fatigue notch, respectively. All of the identified cracked inclusions had crack arrest in the particle, except for the initiation site for sample 167. More examples of cracked inclusions can be found in the appendix.

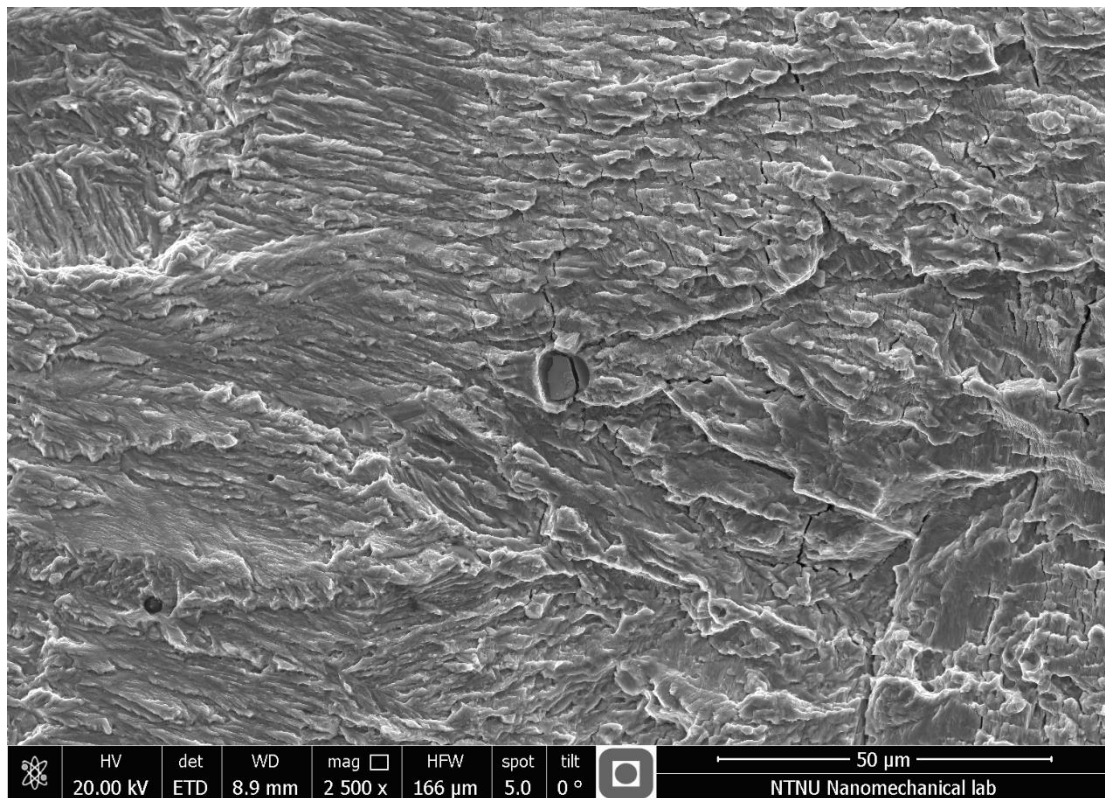


Figure 68 – SEM fractograph of cracked particle in sample 167 (CGHAZ 5)

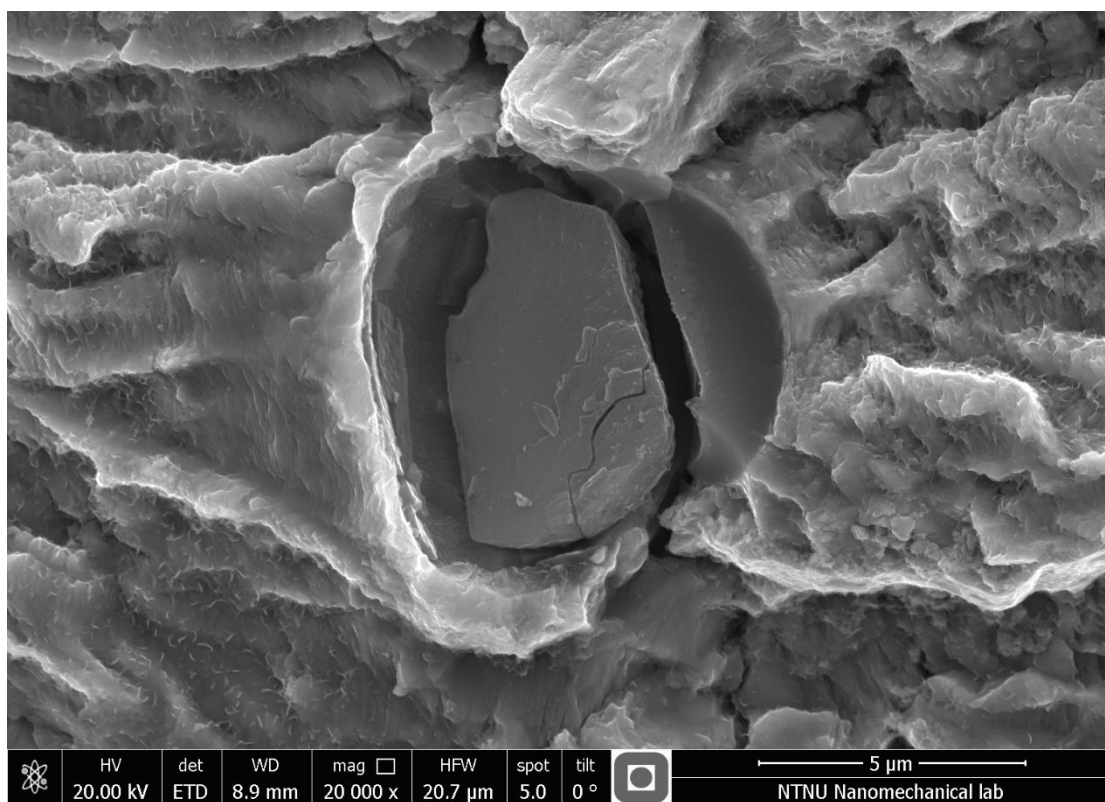


Figure 69 – SEM fractograph of cracked particle in sample 167 (CGHAZ 5), close-up of Figure 68

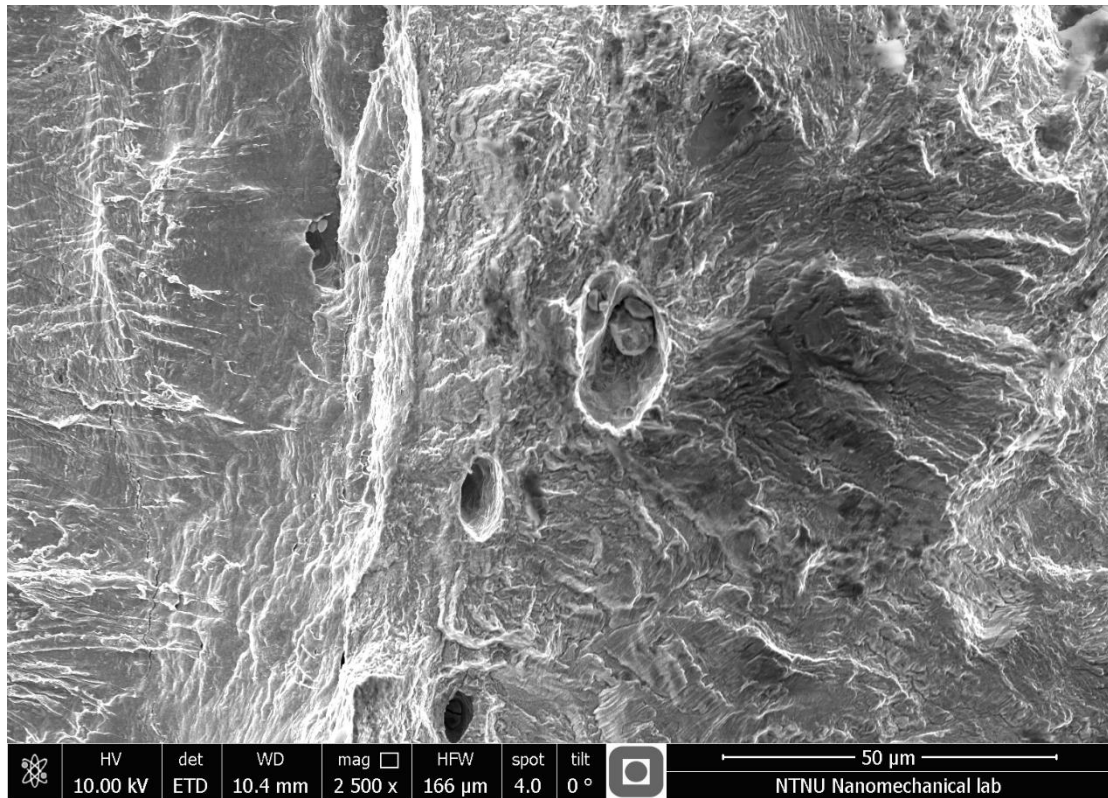


Figure 70 – SEM fractograph of cracked inclusions in sample 180 (CGHAZ 15)

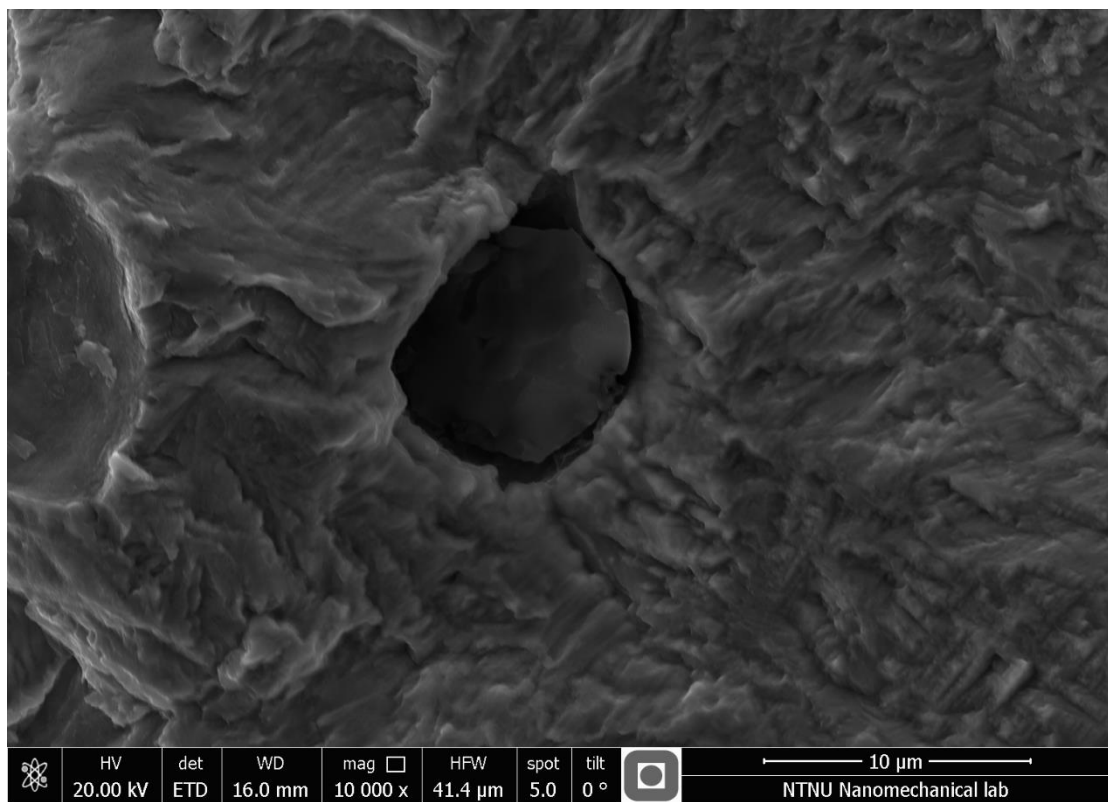


Figure 71 – SEM fractograph of cracked inclusion in sample 339 (ICCGHAZ 15)

#### 5.4.4 EDS ANALYSIS

The EDS analysis of the matrix and the flat areas showed very similar results. All samples showed more or less the result given in Figure 72 for both the matrix and the flat areas. The intensity, or number of X-rays, are plotted on the vertical axis, and the X-ray energy is plotted on the horizontal axis. As mentioned, the X-rays energy is characteristic for the particular atom. E.g. iron which got an electron in the K-shell replaced by an L shell electron emits 6.4 keV  $K\alpha$  X-rays as seen in the figure. Also seen in the figure, there is a small peak of carbon. This was found to vary a lot for all the EDS measurements, both within (different spots) and between the sample areas. Carbon content is, however, difficult to measure by EDS (Brandt et al., 2012).

EDS analysis of the particle in Figure 67 (a) are shown in Figure 73 (particle from cleavage facet initiation on sample 167). As seen, there is high peaks of sulfur and calcium in addition to iron. There also seem to be some oxygen and aluminum present in the particle. The other part of the particle on the opposite fracture surface Figure 67 (b), and the other cracked particle in the figure ((c) and (d)) have a similar result from the EDS measurement, with somewhat varying amount of the elements mentioned. This indicate that this particle is some kind of inclusion.

EDS analysis of the particle in Figure 69 are showing the same results as the above described particles, as seen in Figure 74. All the elements in the figure are the one investigated for all spots and samples. Except for iron, oxygen, aluminum, sulfur, carbon and calcium, the values for these were found to be very small, although some higher than the ones given in the chemical composition for the steel. The general results from the particle in all of the samples indicates that they are inclusions, with varying amount of oxygen, aluminum, calcium and sulfur.

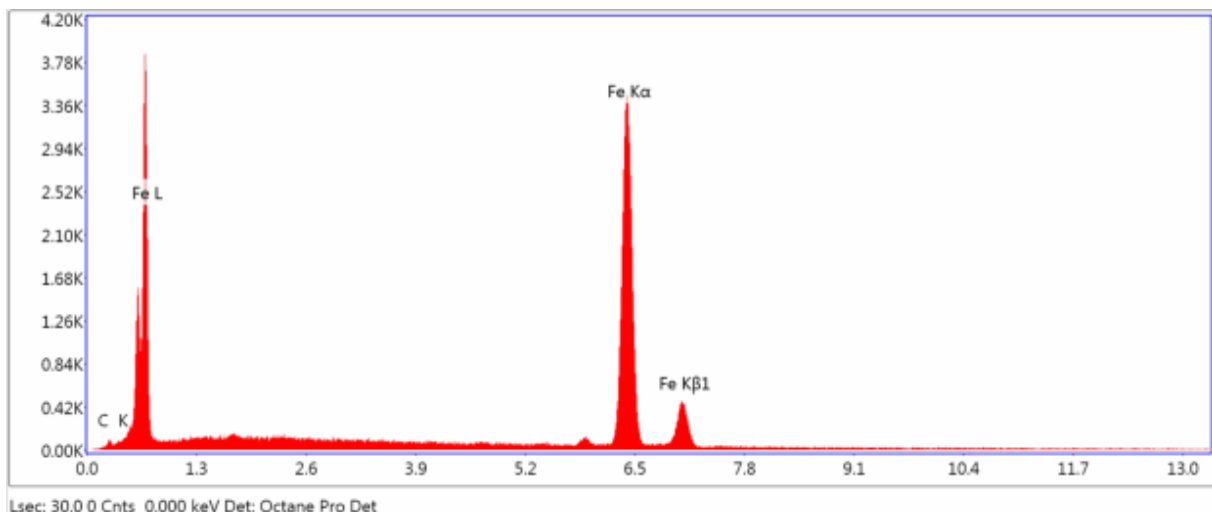


Figure 72 – EDS analysis of a flat area in sample 167, shown in Figure 31.

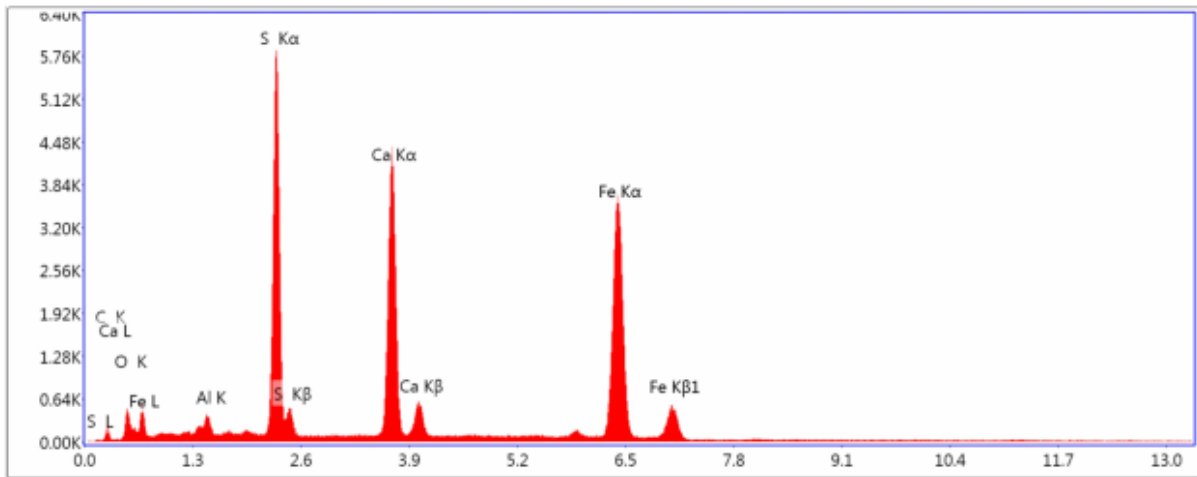


Figure 73 – EDS analysis of the particle in Figure 67 (a)

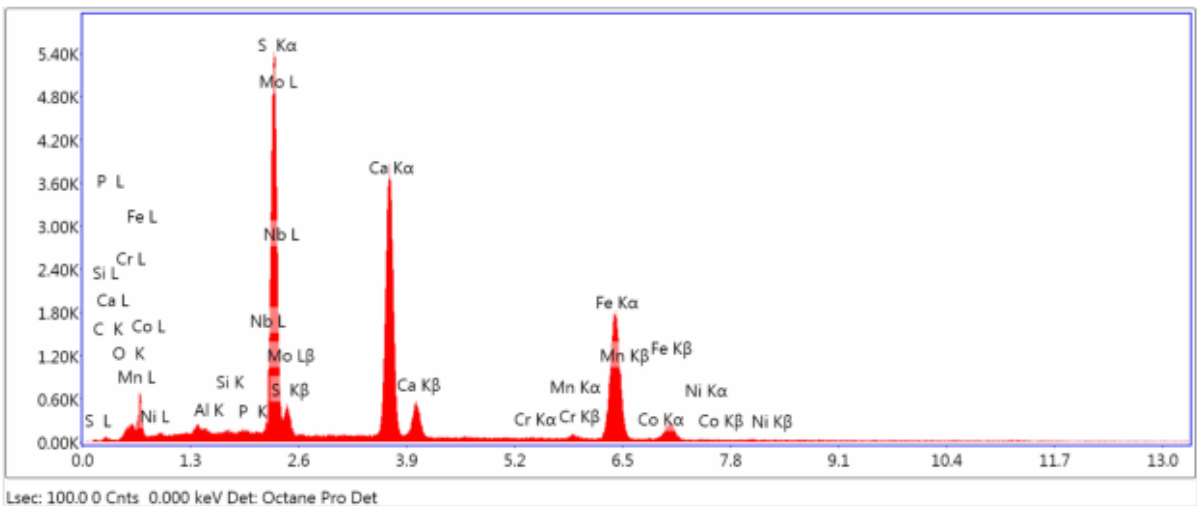
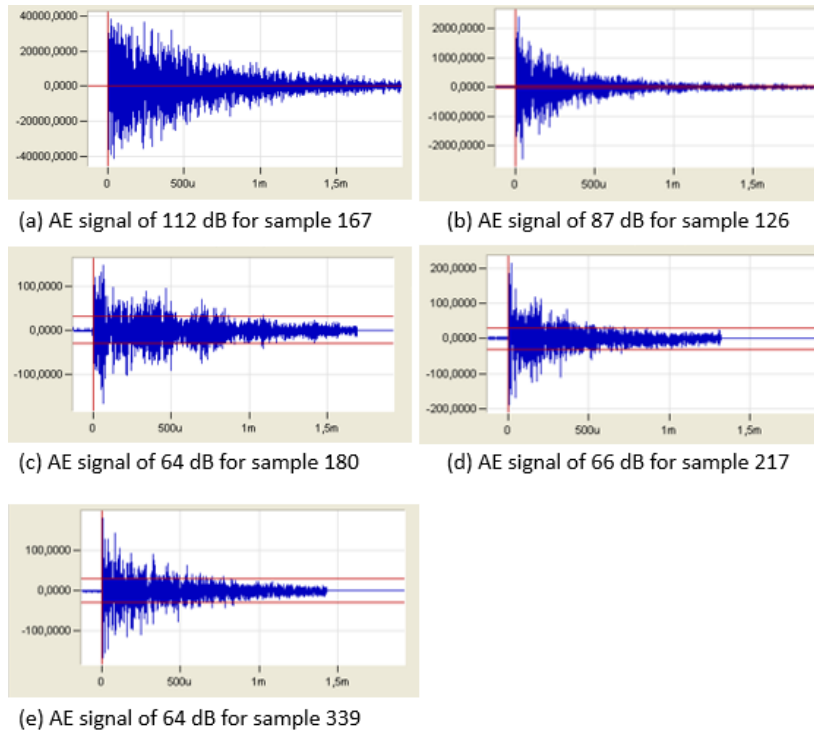


Figure 74 – EDS analysis of the particle in Figure 69

#### 5.4.5 SHAPE OF AE SIGNALS

The shape of the AE signals for the interrupted samples are given in Figure 75. As seen, they all have more or less the characteristic “burst” shape associated with a cleavage microcrack (Østby et al., 2013). Sample 180 seems to deviate the most from this.





*Figure 75 – Shape of AE signals for interrupted sample*

## 6. DISCUSSION

*This chapter discusses the believed initiation and propagation micromechanisms for the Ruukki steel and its relation to Østby et al. (2012) model and the multiple-barrier model. Other relevant topics from the result section will also be discussed, starting the microstructure and its relation to fracture toughness.*

### 6.1 MICROSTRUCTURE

The microstructural analysis conducted in this thesis show similar result to the screening report (Akselsen, 2014a), which give an indication that there is no big differences between the samples within the same weld simulation. Although, as mention, the material is highly inhomogeneous, which could lead to scatter in fracture toughness. As the microstructure seem to be a mix of upper bainite with varying degree of auto-tempering, this could lead to scatter in the fracture toughness results in regards to which microstructure the crack first initiates in, according to Zhang and Knott (1999).

The microstructure for the CGHAZ 25 weld simulated samples were not investigated. However, as the trend is an increase in coarse upper bainite with increasing cooling time, it is believed that the CGHAZ 25 microstructure consist of mostly coarse upper bainite. As the austenite grain size for the other weld simulated samples are around 100  $\mu\text{m}$ , this is believed to be the case for CGHAZ 25 as well. This coarse bainitic structure with large prior austenite grains is believed to be a contribution to the poor fracture toughness, as this microstructure has a poor crack propagation resistance. (Yokoyama and Nagumo, 1998, Lambert-Perlade et al., 2004b)

It is uncertain if ferrite found in the microstructure, as it had to be studied with a higher magnification to detect. It is also difficult to detect it in this steel, as the microstructure is not as distinct with clear different phases as found for other steels. There was however, indications that it could be present, especially for the ICCGAZ 15. This would comply with theory, as reheating bainitic CGHAZ in the two phase area would transform some of the coarse bainite into fine-grained ferrite and bainite (Yokoyama and Nagumo, 1998).

If the areas with small circles indicated in Figure 35 are fine-grained bainite and ferrite, this could possible lead to a lower fracture toughness and explain why there is a tendency for the fracture toughness to increase with increasing cooling rates. There is more of these areas with decreasing cooling times, and as explained by Yokoyama and Nagumo (1998), this could give rise to intense strain concentrations and induce a high defect density and create microcracks.

Comparing the obtained hardness values for the Ruukki steel with the ones investigated by Fairchild et al. (2000), indicates that the microstructure is mainly upper bainite, as this was the microstructure that had similar hardness values. There could still be auto-tempered martensite present, as the hardness value for this and upper bainite is believed to be similar. Martensite had a notably higher hardness value, thus it is believed to be almost no martensite in the microstructure for the Ruukki steel as all the values for this steel was more or less the



same (also to the values obtained in the screening report). Thus, the small circles indicated in Figure 35 could be fine bainite and ferrite instead of martensite, making the above described initiation possibility more likely. However, even though the steels in Fairchild et al. (2000) has similar chemical composition and low carbon content, the carbon content is still notably higher than for the Ruukki steel. Thus, the comparison can not be completely trusted, as carbon content affect the hardness. The hardness measurement further away from the fracture surface show lower values as expected.

#### 6.1.1 BASE MATERIAL AND INTERGRANULAR FRACTURE

The low carbon amount would give a lower strength than the one obtained for this steel on the base material. The reason for this seems to be the fine grain size and a mostly bainitic microstructure. The microstructure indicated that the rolling process is similar to case D in Figure 6, i.e. rolling in the mixed austenite and ferrite phase area. The reason for investigating the base microstructure was to see if it could give an explanation in why the flat areas on the fracture surface appeared. The theory was that the controlled rolling would somehow weaken the prior austenite grain boundaries, leading to partially intergranular fracture, which would give an appearance similar to the flat areas (same size range as austenite grains as well). However, no results from the microstructure analysis or literature was found to support this theory.

As mention in the theory section, only segregation of brittle phases on the grain boundaries could be a possible reason for intergranular fracture, given the environment and temperature for the testing of this steel. However, there are a very little amount of phosphorus and sulfur in the steel, the chemicals that normally cause intergranular fracture, according to Anderson (2005). In addition, the flat areas have sharp angles within, which could possibly be from a crack crossing a bainite packet boundary or an austenite grain boundary. Hence, it is no found reasoning for the flat areas being intergranular fracture.

#### 6.1.2 M-A PHASES

Both CGHAZ 15 and ICCGHAZ 15 simulated samples contained approximately the same M-A amounts and morphology. This could be due to the low carbon content, which is lower than the solubility of carbon in ferrite (Callister and Rethwisch, 2011). The second thermal cycle temperature of 780 °C might be just below the phase transformation temperature, as seen in Figure 1. Thus, austenite will not be formed followed by M-A constituents upon cooling. In this case, the M-A phases in the ICCGHAZ was formed in the first weld cycle. As M-A phases are usually found more frequently, and with a bigger size in ICCGHAZ (Bonnevie et al., 2004), this supports the assumption that the second weld simulation might be under the phase transformation temperature for the investigated samples. However, it could also be just because the little amount of carbon is not enough to form more M-A phases in the ICCGHAZ, which seems more likely.

As the most of the M-A phases found on the samples are around or less than 1 µm, these could be retained austenite containing little or none martensite, according to Davis and King (1994).

These are most likely not to initiate fracture and could even be a contribution to increase in toughness as explained by Cuixin et al. (2008).

The bigger M-A particle could initiate fracture, especially when located close to each other (Mohseni et al., 2014). These are scattered widely in both CGHAZ 15 and ICCGHAZ 15, thus could contribute to the scatter in fracture toughness. As it is assumed not to be more M-A phases in ICCGHAZ, this explain why there is approximately the same amount of scatter in both weld simulations (Østby et al., 2011).

## 6.2 FLAT AREAS ON THE FRACTURE SURFACE

As discussed in the microstructure section, the flat areas has the appearance of partly intergranular fracture, however, there was not found any literature to support the occurrence of this fracture mode. Another theory, as stated in the result section, is that they are brittle cracks along slip-planes, leaving smooth surfaces instead of the characteristic river lines. This would indicate good micro-crack arrest properties, as most of these flat areas are quite small, i.e. less than 50  $\mu\text{m}$ . The nital etched fracture surface in Figure 55 indicate that the micro crack propagated over bainite packets, and arrested at prior austenite grain boundaries. However, other etched flat areas showed different features than this, so it is difficult to say anything certain about the propagation and arrest mechanism of the flat areas.

The EDS analysis conducted on the flat areas indicated that they had the same composition as the matrix, i.e. there were not found any impurities of any kind that could explain the flat areas. The carbon content was varying and sometimes high, but there was no consistency in a possible carbon accumulation as in M-A constituents to explain the initiation of the flat areas, especially with carbon being difficult to measure with EDS (Brandt et al., 2012).

The flat areas seems to initiate easily with no need for high stresses, as they were found in the pre-test fatigue notch as well as after, i.e. initiated from the low stresses from the fatigue loading. There could be local stress concentrations around the flat areas, but it is believed that these are not high enough to raise the stresses up to the same level as the test loading. It is therefore not certain that they released enough energy to emit an AE signal over 50 dB. As the flat areas initiates and arrest easily, they are believed to not affect the fracture toughness considerably.

In addition to the uncertainty in what the flat area actually is and the AE signal it emits if it is assumed to be brittle cracks, there is a possible different correlation of this area and the characteristic cleavage facet area to the AE signal amplitude. Another problem is the correlating of the right flat area to the corresponding AE signal, as multiple of these appears on the fracture surface. To take the first flat area as the believed source of the AE signal, as done in the result section, have several possible source of errors. The biggest one is that as the crack initiates and propagate as a flat area before arresting, the macro-crack does not “join-up” with this microcrack before the post-test fatigue loading reaches this flat area. Thus, it is not necessarily the flat area closest to the pre-test fatigue notch who initiates first. This

depends on the local stress and strain concentration. The highest stress values is at the double CTOD (Anderson, 2005), thus this give an indication in where the flat area could initiate, but this is not certain enough to relate the flat area to the CTOD value.

### 6.3 CRACK INITIATION

The crack initiation mechanism for sample 167 (CGHAZ 5), seemed to be due to cracking of the two particles at the initiation site. The EDS analysis of the particles indicates that they are some kind of inclusion, as both sides of the two particle gave varying amounts of sulfur, calcium, oxygen and aluminum on the EDS measurements. This was similar to the results for initiation in CGHAZ obtained by Brandt et al. (2012), which had the same EDS analysis result and concluded that it was oxide and sulphide slag particles that initiated the crack. The small cavity around the particle in Figure 67 (a) could indicate that this is manly a sulfide particle according to Agboola (2010).

The cavity and it being two particles at the initiation site could trigger the initiation more than a single particle. Microcracks form more easily at cavities and the two micro-cracking events from the particles could be connected upon loading causing a bigger microcrack. The low fracture toughness for this sample seem to be due to the fracture triggering particles being located close to the pre-test fatigue notch (Anderson, 2005). For other samples, these inclusions may be located far away from the notch, causing the scatter in fracture toughness.

Only one example of fracture initiation is not enough to say anything certain about the crack initiation mechanism. Comparing to the samples run to fracture is difficult as these had to be studied more thoroughly. The initiation mechanism is, however, not believed to be associated with cracking of TiN inclusion since none of the inclusions showed signs of containing TiN in the EDS analysis. This most likely due to the small amount of Ti in the steel (Fairchild et al., 2000).

### 6.4 CRACK PROPAGATION

#### 6.4.1 AE SIGNALS AND BARRIERS TO CRACK PROPAGATION

There is not many AE signals for the steel, which indicate that there is not much arrest of microcracks (Østby et al., 2013). The samples without any AE signals are believed to be nucleation controlled (Lambert-Perlade et al., 2004a), which is the case for most of the samples with a low CMOD. The AE signals for the samples that had signals at low CMOD values was investigated to see if these could possibly be emitted from something else, leaving all sample at low CMOD nucleation controlled. However, there was nothing in the findings that could suggest this with any certainty, as all the AE signals had more or less the characteristic “burst” shape. In addition, some of the AE signals was around 70 dB, hence not low enough to assume it coming from noise. One of the AE signal for sample 138 did however deviated from this slightly (Figure 46 (b)).

Thus, it is believed that the samples have some microstructural barriers to propagation, even for the ones with a low CMOD value. According to literature, this could be dislocation

structure, grain boundary misorientation and the amount of intergranular ferrite (Lan et al., 2011). It could also be possible from a microcrack arrested in a particle (Lambert-Perlade et al., 2004a), hence the AE signal was emitted from particle cracking. From the research conducted in this thesis, it is not possible to say what the barriers to propagation could be. The grain boundary misorientation can not be measured from a light microscope. It has to be measured with electron backscatter diffraction (EBSD) (Lambert-Perlade et al., 2004b). The inhomogeneous microstructure could, however, explain the scatter in crack arrest. If the microcrack initiate close to for example a high angled grain boundary, it could be arrested easily (Lambert-Perlade et al., 2004b). If it initiate at a coarse bainite packet, there would be less obstacles for the crack propagation, and the crack could more easily propagate to final fracture or to a large arrested microcrack giving a high AE signal amplitude (Yokoyama and Nagumo, 1998, Østby et al., 2012). This seem to be the case for the initiation in sample 167, as the cleavage facets are large (Lan et al., 2011).

#### 6.4.2 ARRESTED MICROCRACK SIZE

Most of the AE signals has a quite low amplitude which would indicate that the corresponding arrested cleavage microcrack is small, according to Østby et al. (2012). As seen in Figure 45, only a few samples have an AE signal amplitude over 80 dB, i.e. a cleavage microcrack size of more than 50  $\mu\text{m}$  (when predicting the microcrack size from the trend line generated by excel from the original AE values from Østby et al. (2012) model). This could indicate that cracks with a low AE signal amplitude initiated far from a coarse bainite packet facet and close to a high angle grain boundary. As it is observed coarse bainite packet in the microstructure, assuming propagation arrest due to a high amount of fine-grained packets with high angle boundaries seems unlikely. In addition, this would indicate much more crack arrest and it has been observed large facets on the fracture surfaces corresponding to coarse grains.

#### 6.4.3 SOURCE OF AE SIGNAL

It is not certain that all of the valid AE signals came from arrested cleavage microcracks. Another possible source is from dimples detaching from the matrix, especially if the dimple is large and the particle inside cracks. This could explain why the samples with a high CMOD has more AE signals, as most of the AE signals are at and around the peak of the load-displacement curve. In addition, for sample 129, 24 and 18, all of the AE signals was emitted within the ductile area of the fracture surface, indicating that the AE signals didn't got emitted from arrested cleavage microcracks. However, this could also be due to them initiating and arresting in a different plane.

The small secondary crack seen in Figure 51 could possible emit a small AE signal if it appeared before the main crack, i.e. if it is not actually a secondary crack. The larger secondary cracks seen in Figure 48 are assumed to give AE signal amplitudes over 113 dB due to the crack propagating to final fracture.

#### 6.4.4 MULTIPLE BARRIER MODEL

As the microcrack in sample 167 grew large and through inclusions before arresting, the temperature in which it got tested, - 30 °C seems to be controlled by the strength of the matrix/matrix interface. I.e. belong to temperature range III in the multiple barrier model according to Lambert-Perlade et al. (2004a). The other CGHAZ 5 samples tested at - 30 °C had no AE signals before fracture, which would correspond to temperature range I according to Lambert-Perlade et al. (2004a). Thus, relating different temperatures to the multiple barrier model based on the results obtained in this thesis governs high uncertainty. A possibility is that all the test temperatures, i.e. - 75 °C to room temperature correspond to temperature range III, although the amount of the matrix/matrix interfaces arresting microcrack, i.e. amount of high angled boundaries, is limited resulting in some microcracks causing final fracture.

However, some microcracks seemed to have been arrested at particle/matrix interfaces, corresponding to temperature range II in the multiple barrier model (Lambert-Perlade et al., 2004a). Perhaps the lowest AE signals could have been emitted from these. An explanation for the difference in microcrack arrest could be a higher local stress and strain concentration at the particles that had the microcrack propagating through the matrix.

#### 6.5 COMPARING THE RESULTS TO AM I

The 420 MPa steel plate used in the AM I project had much more carbon and thus more and larger M-A constituents in the ICCGAZ microstructure (Brandt et al., 2012). The AE activity for this steel was therefore much higher, as the M-A constituents easily initiated cleavage microcracks (Brandt et al., 2012, Østby et al., 2013). The maximum AE signals in Østby et al. (2013) paper was around 500 and for the Ruukki steel it was 13. This also indicate that the crack arrest properties is better for the steel used in the AM I project, as the fracture toughness was somewhat similar to the Ruukki steel. Although, the Ruukki steel seem to have a slightly higher fracture toughness, most likely due to the lack of large fracture triggering M-A constituents.

#### 6.6 AE SIGNAL AMPLITUDE VS ARRESTED CLEAVAGE MICROCRACK SIZE

As the interrupted AE testing in this thesis only had one characteristic arrested microcrack facet (sample 167), it is not possible to say how the Ruukki steel behaves regarding Østby et al. (2012) model. The correlation from sample 167 did indicate that the correlation is valid for the Ruukki steel as well. As the correlation by Østby et al. (2012) is exponential and rapidly increasing in the area for the emitted AE signal amplitude, the arrested microcrack could correlate to the amplitude in a large size range. Thus, all of the proposed method in determining the facet area from the result section could be a possibility.

Regarding the flat areas, there is no way of relating this to Østby et al. (2012) with any certainty as discussed earlier. In addition to the flat areas problem for the interrupted samples, it is also difficult to conduct interrupted testing on the Ruukki steel due to it emitting only a few AE

signals during testing. All of the highest AE signal amplitudes, i.e. over 80 dB, came after a lot of plastic deformation, and often with some AE signals with a lower amplitude before this. Both low AE signal amplitudes and samples with a lot of plastic deformation is difficult to detect on the fracture surface.

## 6.7 SUGGESTION FOR FURTHER WORK

The low carbon content in the Ruukki steel seem to reduce the formation of M-A constituent. However, it would be interesting to further confirm this by investigating more sample with LePera etchant and to investigate the effect of different peak temperatures for the second weld cycle. A higher second peak temperature could confirm that there is less M-A constituents formed, and not just because the temperature is not high enough to reach the two phase area.

To better understand the propagation and arrest properties for the steel, an EBSD analysis on the microstructure could confirm the assumption that the steel has few high angle grain/packet boundaries. An EBSD analysis could also be used on the fracture surface, to investigate the misorientation where the cleavage micro crack for the interrupted test and the flat areas arrested.

The initiation mechanism should also be further studied. As interrupted testing for this steel is difficult, this could be done on samples run to final fracture by studying the origin of the river marks with etchants that can revile M-A constituents. Another possibility is to cut the steel at the initiation site on the fracture surface, and investigate the microstructure on the perpendicular side of the initiation.

More data is needed to say anything in regards to Østby et al. (2012) model for this steel. It would be interesting to investigate further, however a lot of interrupted testing would have to be conducted, as the steel do not emit much AE signals. For more data input for the model, it is beneficial to use another steel that is more propagation controlled, i.e. emits more AE signals.

## 7. CONCLUSION

The steel investigated in this thesis had a very low carbon content in order to decrease the formation of the fracture triggering M-A constituents formed during welding. As the M-A constituents identified in SEM for both CGHAZ and ICCGHAZ using LePera etchant was relatively small compared to the M-A constituents that usually triggers fracture, it is believed that the reduction in carbon content did decrease the crack initiation for the steel.

This assumption was supported due to a low amount of AE signals, associated with cleavage microcrack nucleation and arrest. However, the steel still had a low fracture toughness for all the weld-simulated samples for most test temperatures. This seems to be due to a coarse upper bainite microstructure and a large prior austenite grain size which was found in the HAZ for all samples. This microstructure is known to decrease the fracture toughness due to an easy crack propagation path.

The initiation mechanism is believed to be due to inclusions and large M-A constituents. These are randomly located in the steel, thus explaining the found scatter in fracture toughness. Some particles were found to have crack arrest at the particle/matrix interface. For further propagation of the microcrack, it is assumed the need for high local stress and strain concentrations.

The microstructure is highly inhomogeneous, with areas of upper bainite and auto-tempered martensite, which are believed to further increase the fracture toughness scatter. This is in regards to which microstructure the crack first initiates. In addition, it is believed to be only a few widely scattered barriers to crack propagation. Thus, it is assumed that if a microcrack initiates close to a crack propagation barrier, it will arrest more easily than if it initiates at a coarse upper bainite packet. This could explain why some samples have a higher toughness and more AE signals than others do.

It is not certain that all of the AE signals came from cleavage micro cracking and arrest. Most of the AE signals came after a lot of plastic deformation, and by investigating the fracture surface for these, it was noted that many AE signals came in the ductile area. This could indicate that some AE signals were emitted from dimples detaching from the matrix, especially if the dimple is large and the particle inside cracks.

Relating the results to Østby et al. (2012) model and the multiple barrier model is difficult, as there was only one valid result from the interrupted testing. More data is needed to say anything certain. The problem with interrupted testing on this steel is that it is mostly nucleation controlled, and when an AE signal is emitted, it is mostly after a lot of plastic deformation. To relate Østby et al. (2012) model with this steel, there is a need for a lot of testing. There is also a need for figuring out what the flat areas appearing on the fracture surface is, and the AE signal they would emit. However, using acoustic emission in fracture mechanic testing for samples running to final fracture, give a good indication if the steel is mostly nucleation or propagation controlled.

## 8. REFERENCES

- Agboola, O. (2010) 'The role of non-metallic inclusions in steel failure', *Am. Eurasian. J. Sci. Res*, vol. 5, pp. 130-133.
- Akselsen, O. M. 2014a. Evaluation of 420 MPa steel welds. Trondheim: SINTEF Materials and Chemistry.
- Akselsen, O. M. (2014b) *Seige materialer for Arktis*. Available at: <http://www.sintef.no/nyheter-fra-gemini.no/seige-materialer-for-arktis/> (Accessed: 02.06.2015).
- Akselsen, O. M. (2014c) *SMACC – Studier av materialoppførsel ved lave temperaturer*. Available at: <http://www.sintef.no/prosjekter/sintef-materialer-og-kjemi/2013/smacc--studier-av-materialoppforsel-ved-lave-temperaturer/> (Accessed: 02.06.2015).
- Anderson, T. L. (2005) *Fracture mechanics: fundamentals and applications*. 3rd edn. Boca Raton, Fla.: Taylor & Francis.
- Arntsen, G. R. (2000) *Stålboka*. Trondheim: Tapir.
- Bhadeshia, H. K. D. H. and Honeycombe, R. W. K. (2006) *Steels: microstructure and properties*. 3rd edn. Amsterdam: Elsevier, Butterworth-Heinemann.
- Bonnevie, E., Ferrière, G., Ikhlef, A., Kaplan, D. and Orain, J. M. (2004) 'Morphological aspects of martensite–austenite constituents in intercritical and coarse grain heat affected zones of structural steels', *Materials Science and Engineering: A*, vol. 385(1–2), pp. 352-358.
- Bramfitt, B. L. and Benschoter, A. O. (2001) *Metallographer's guide: practice and procedures for irons and steels*. Materials Park, OH: ASM International.
- Brandt, K., Solberg, J. K., Akselsen, O. M. and Østby, E. 'Initiation of Cleavage Fracture in a Weld Simulated Low Carbon Low Alloy Arctic Steel', *Proceedings of the Twenty-second (2012) International Offshore and Polar Engineering Conference*: International Society of Offshore & Polar Engineers, 323-328.
- Callister, W. D. and Rethwisch, D. G. (2011) *Materials Science and Engineering*. 8th edn. Asia: John Wiley & Sons.
- Cuixin, C., Li, W. and Huifen, P. (2008) 'Investigation on M-A Constituent in Weld CGHAZ of High-strength Microalloyed Steel', *Materials Science Forum*, vol. 575, pp. 690–695.
- Davis, C. L. and King, J. E. (1994) 'Cleavage Initiation in the Intercritically Reheated Coarse-Grained Heat-Affected Zone: Part I. Fractographic Evidence ', *Metallurgical and materials transactions A* vol. 25A.
- Fairchild, D., Howden, D. and Clark, W. (2000) 'The mechanism of brittle fracture in a microalloyed steel: Part I. Inclusion-induced cleavage', *Metallurgical and Materials Transactions A*, vol. 31(3), pp. 641-652.
- International, A. (2014) 'Standard Test Methods for Determining Average Grain Size', *ASTM International*.
- Lambert-Perlade, A., Gourgues, A. F., Besson, J., Sturel, T. and Pineau, A. (2004a) 'Mechanisms and Modeling of Cleavage Fracture in Simulated Heat-Affected Zone Microstructures of a High-Strength Low Alloy Steel', *Metallurgical and materials transactions A*, vol. 35 A.
- Lambert-Perlade, A., Gourgues, A. F. and Pineau, A. (2004b) 'Austenite to bainite phase transformation in the heat-affected zone of a high strength low alloy steel', *Acta Materialia*, vol. 52(8), pp. 2337-2348.



- Lan, L., Qiu, C., Zhao, D., Gao, X. and Du, L. (2011) 'Microstructural characteristics and toughness of the simulated coarse grained heat affected zone of high strength low carbon bainitic steel', *Materials Science and Engineering: A*, vol. 529(0), pp. 192-200.
- Larsen, A. V. 2014. Acoustic emission from brittle fracture. Trondheim: Norwegian University of Science and Technology.
- LePera, F. S. (1979) 'Improved etching technique for the determination of percent martensite in high-strength dual-phase steels', *Metallography*, vol. 12(3), pp. 263-268.
- Moeinifar, S., Kokabi, A. H. and Madaah Hosseini, H. R. (2010) 'Influence of peak temperature during simulation and real thermal cycles on microstructure and fracture properties of the reheated zones', *Materials & Design*, vol. 31(6), pp. 2948-2955.
- Mohseni, P., Solberg, J. K., Karlsen, M., Akselsen, O. M. and Østby, E. (2014) 'Cleavage Fracture Initiation at M–A Constituents in Intercritically Coarse-Grained Heat-Affected Zone of a HSLA Steel', *Metallurgical and materials transactions A*, vol. 45A, pp. 384-394.
- Ortner, S. R. (2006) 'The ductile-to-brittle transition in steels controlled by particle cracking', *Fatigue & Fracture of Engineering Materials & Structures*, vol. 29(9-10), pp. 752-769.
- Pineau, A. (2007) 'Development of the local approach to fracture over the past 25 years : Theory and applications', *Anales de la Mecánica de Fractura*, vol. 1.
- SINTEF (2010) *Arctic materials, project objectives*. Available at: <http://www.sintef.no/projectweb/arctic-materials/project-objectives/> (Accessed: 02.06.2015).
- Solberg, J. K. (2007) *Teknologiske metaller og legeringer*. Trondheim: Institutt for materialteknologi, Norges teknisk-naturvitenskapelige universitet.
- Vander Voort, G. F. (2004) *ASM handbook, Volume 9, Metallography and microstructures*. Materials Park, OH: ASM International.
- Wadley, R. N. G., Scruby, C. B. and Shrimpton, G. (1981) 'Quantitative acoustic emission source characterisation during low temperature cleavage and intergranular fracture', *Acta Metallurgica*, vol. 29(2), pp. 399-414.
- Weidner, A., Mottitschka, T., Biermann, H. and Henkel, S. (2013) 'Determination of stretch zone width and height by powerful 3D SEM imaging technology', *Engineering Fracture Mechanics*, vol. 108(0), pp. 294-304.
- Yokoyama, K. i. and Nagumo, M. (1998) 'Brittle fracture initiation associated with the strain localization in a heat-affected zone of a low carbon steel', *Metallurgical and Materials Transactions A*, vol. 29(2), pp. 551-558.
- Zhang, X. Z. and Knott, J. F. (1999) 'Cleavage fracture in bainitic and martensitic microstructures', *Acta Materialia*, vol. 47(12), pp. 3483-3495.
- Østby, E., Akselsen, O. and Kristensen, T. A. 'Monitoring of cleavage microcrack arrest in weld thermal simulated microstructures by means of acoustic emission', *The International Society of Offshore and Polar Engineers (ISOPE): SINTEF Materials and Chemistry*.
- Østby, E., Thaulow, C. and Akselsen, O. (2012) 'Quantitative Relation Between Acoustic Emission Signal Amplitude and Arrested Cleavage Microcrack Size', *International Journal of Fracture*, vol. 177(1), pp. 73-80.

Østby, E., Thaulow, C. and Odd Magne, A. 'Fracture Toughness Scatter and Effect of Constraint in Weld Thermal Simulated HAZ Microstructures at -60°C ', *ISOPE 2011*, Maui, Hawaii: ISOPE, The Int. Soc. of Offshore and Polar Eng., 443-448.

## 9. APPENDICES

### 9.1 TABLES FROM TESTING

Table 9 – Test results from 2014, SENB05 (Tested at - 60°C)

Sample	Type	Load (kN)	CMOD (mm)	Valid AE signals
5	CGHAZ 15	6.4803	0.828	0
6	CGHAZ 15	5.0896	0.1641	0
7	CGHAZ 15	6.689	1.8316	2
11	ICCGHAZ 15	6.6991	0.9013	0
12	ICCGHAZ 15	5.7936	0.2542	2
13	ICCGHAZ 15	6.8401	1.0097	0
17	CGHAZ 10	5.2855	0.188	0
18	CGHAZ 10	5.9072	3.1404	9
19	CGHAZ 10	4.4954	0.1069	0
23	ICCGHAZ 10	6.2917	0.4694	0
24	ICCGHAZ 10	6.5957	3.1709	13
25	ICCGHAZ 10	7.0067	1.1346	1
30	CGHAZ 5	6.3924	0.5733	0
31	CGHAZ 5	6.614	0.7515	0
32	CGHAZ 5	6.2276	0.4475	0
36	ICCGHAZ 5	5.2873	0.1337	0
37	ICCGHAZ 5	5.0172	0.1141	0
38	ICCGHAZ 5	5.258	0.1325	0

Table 10 – Test results from 2015 on SENB05

Sample	$\Delta t_{8-5}$	Test temperature (°C)	Load (kN)	CMOD (mm)	Valid AE signals
49	5	-30	6.798	0.8241	0
51	5	-30	4.9678	0.1365	0
52	5	-30	5.6929	0.2103	0
54	5	0	3.8911	3.7637	2
55	5	0	2.1223	3.9393	5
57	5	0	6.5993	0.9014	4
59	5	22	6.3933	2.4422	1
60	5	22	6.2047	2.833	1
88	15	-30	4.7975	0.1221	0
89	15	-30	6.0894	3.3846	2
90	15	-30	5.7469	3.8097	8
91	15	0	4.9586	0.2091	0
93	15	0	1.3047	3.6836	1
94	15	22	4.8021	3.7218	1
95	15	22	6.3375	1.5644	1
129	25	-30	6.5874	2.2529	5
130	25	-30	6.7302	2.1461	1
131	25	-30	5.4018	3.9857	8

<b>132</b>	25	-60	5.6737	0.2835	0
<b>133</b>	25	-60	5.0401	0.1434	0
<b>134</b>	25	-60	5.5446	3.6816	12
<b>135</b>	25	-45	6.6707	2.4899	2
<b>136</b>	25	-45	5.9072	3.4792	8
<b>137</b>	25	-45	5.7451	3.5281	5
<b>138</b>	25	-75	5.4018	0.1981	2
<b>139</b>	25	-75	6.4711	0.6392	1
<b>140</b>	25	-75	3.8252	0.0752	0

Table 11 – Valid AE signals for test conducted in 2014, all tested at – 60 °C

<b>Samlpe</b>	<b>Type</b>	<b>Load (kN)</b>	<b>CMOD (mm)</b>	<b>AMP(dB)</b>
<b>7</b>	CGHAZ 15	6.6753	1.5657	79
<b>7</b>	CGHAZ 15	6.6808	1.6268	64
<b>12</b>	ICCGHAZ 15	0.1831	0.0021	53
<b>12</b>	ICCGHAZ 15	0.2179	0.0026	52
<b>18</b>	CGHAZ 10	6.7302	1.6911	61
<b>18</b>	CGHAZ 10	6.7037	1.8919	80
<b>18</b>	CGHAZ 10	6.6698	2.0003	71
<b>18</b>	CGHAZ 10	6.191	2.8426	54
<b>18</b>	CGHAZ 10	6.1791	2.8574	82
<b>18</b>	CGHAZ 10	6.1745	2.8623	82
<b>18</b>	CGHAZ 10	5.9749	3.0932	51
<b>18</b>	CGHAZ 10	5.9438	3.1093	61
<b>18</b>	CGHAZ 10	5.9218	3.1198	57
<b>24</b>	ICCGHAZ 10	7.1395	1.3544	64
<b>24</b>	ICCGHAZ 10	7.2292	1.7665	86
<b>24</b>	ICCGHAZ 10	7.2265	1.809	75
<b>24</b>	ICCGHAZ 10	7.2137	2.1328	70
<b>24</b>	ICCGHAZ 10	7.1322	2.3066	91
<b>24</b>	ICCGHAZ 10	7.1157	2.4039	65
<b>24</b>	ICCGHAZ 10	7.0406	2.5918	76
<b>24</b>	ICCGHAZ 10	7.036	2.5942	84
<b>24</b>	ICCGHAZ 10	7.0251	2.6118	59
<b>24</b>	ICCGHAZ 10	6.9179	2.7714	74
<b>24</b>	ICCGHAZ 10	6.6131	3.1494	73
<b>24</b>	ICCGHAZ 10	6.5947	3.1709	73
<b>24</b>	ICCGHAZ 10	6.5957	3.1709	93
<b>25</b>	ICCGHAZ 10	7.004	1.13	55

Table 12 – Valid AE signals for SENB05 tests conducted in 2015

$\Delta t_{8-5}$	Sample	Load (kN)	CMOD (mm)	AMP (dB)	Test temp. (°C)	
<b>5sec1cyc</b>	59	6.3933	2.4422	56	22	
	60	6.2047	2.833	106	22	
<b>15sec1cyc</b>	94	4.8021	3.7218	55	22	
<b>5sec1cyc</b>	54	6.5764	2.204	59	0	
	54	3.8911	3.7637	56	0	
	55	6.6936	1.5053	62	0	
	55	6.1837	2.9117	84	0	
	55	5.4109	3.4088	57	0	
	55	5.0063	3.793	76	0	
	55	2.1223	3.9393	60	0	
	57	6.0784	0.401	64	0	
	57	6.256	0.5145	65	0	
	57	6.4061	0.6437	65	0	
	57	6.4702	0.7119	74	0	
	<b>15sec1cyc</b>	93	6.0079	0.5784	67	0
	<b>15sec1cyc</b>	89	6.7302	1.8245	65	-30
89		6.57	2.6243	74	-30	
90		6.3979	0.8024	64	-30	
90		6.5517	1.0136	55	-30	
90		6.6817	2.4657	72	-30	
90		6.6332	2.5775	77	-30	
90		6.6231	2.6298	67	-30	
90		6.3869	3.2177	96	-30	
90		6.1901	3.4773	67	-30	
90		5.7469	3.8097	95	-30	
<b>25sec1cyc</b>	129	5.0603	0.2225	72	-30	
	129	5.1061	0.2295	60	-30	
	129	5.324	0.2688	64	-30	
	129	6.6671	2.1225	66	-30	
	129	6.5874	2.2529	75	-30	
	130	6.7302	2.1461	62	-30	
	131	5.6609	0.3084	73	-30	
	131	5.9978	0.4804	66	-30	
	131	6.6341	2.205	52	-30	
	131	6.614	2.2612	90	-30	
	131	6.516	2.5202	63	-30	
	131	6.484	2.5695	56	-30	
	131	6.2386	3.1502	66	-30	
131	5.4018	3.9857	61	-30		
<b>1cyc25sec</b>	135	6.7541	1.8096	69	-45	
	135	6.7513	1.9006	71	-45	
	136	5.4814	0.2655	58	-45	
	136	6.6543	1.7591	53	-45	

136	6.6451	1.8174	89	-45	
136	6.5508	2.2551	70	-45	
136	6.4977	2.3884	56	-45	
136	6.1809	3.0835	90	-45	
136	5.9529	3.4106	54	-45	
136	5.9072	3.4792	87	-45	
137	4.4459	0.1097	56	-45	
137	6.5078	2.4273	68	-45	
137	6.3164	2.773	60	-45	
137	6.0125	3.2124	52	-45	
137	5.7707	3.4678	63	-45	
<b>25sec1cyc</b>	134	6.8795	1.8267	59	-60
	134	6.8804	2.008	62	-60
	134	6.8657	2.1054	79	-60
	134	6.787	2.3314	87	-60
	134	6.7641	2.3874	69	-60
	134	6.7138	2.4858	80	-60
	134	6.5673	2.7401	66	-60
	134	6.5297	2.7909	85	-60
	134	5.6453	3.6139	54	-60
	134	5.5391	3.6484	52	-60
	134	5.5446	3.663	62	-60
	134	5.5446	3.6816	70	-60
<b>25sec1cyc</b>	138	2.0005	0.0321	71	-75
	138	2.3777	0.0377	75	-75
	139	3.3445	0.0595	66	-75



9.2 MICROGRAPHS

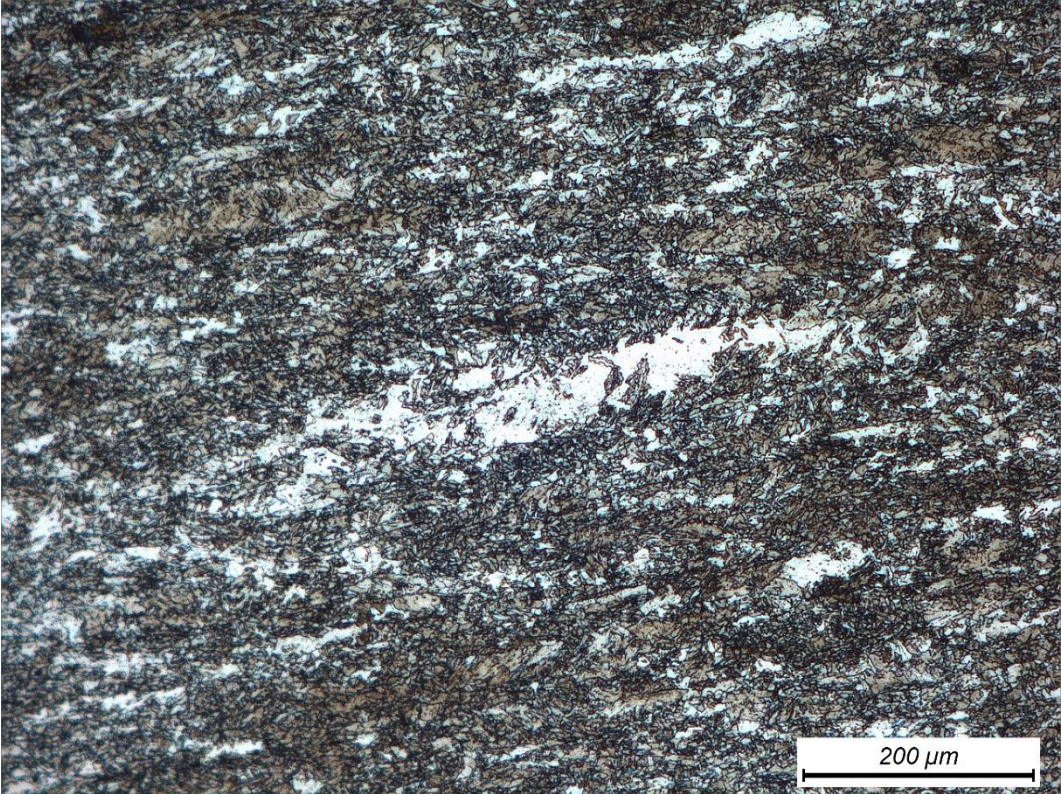


Figure 76 – Micrograph of the base material in sample 12

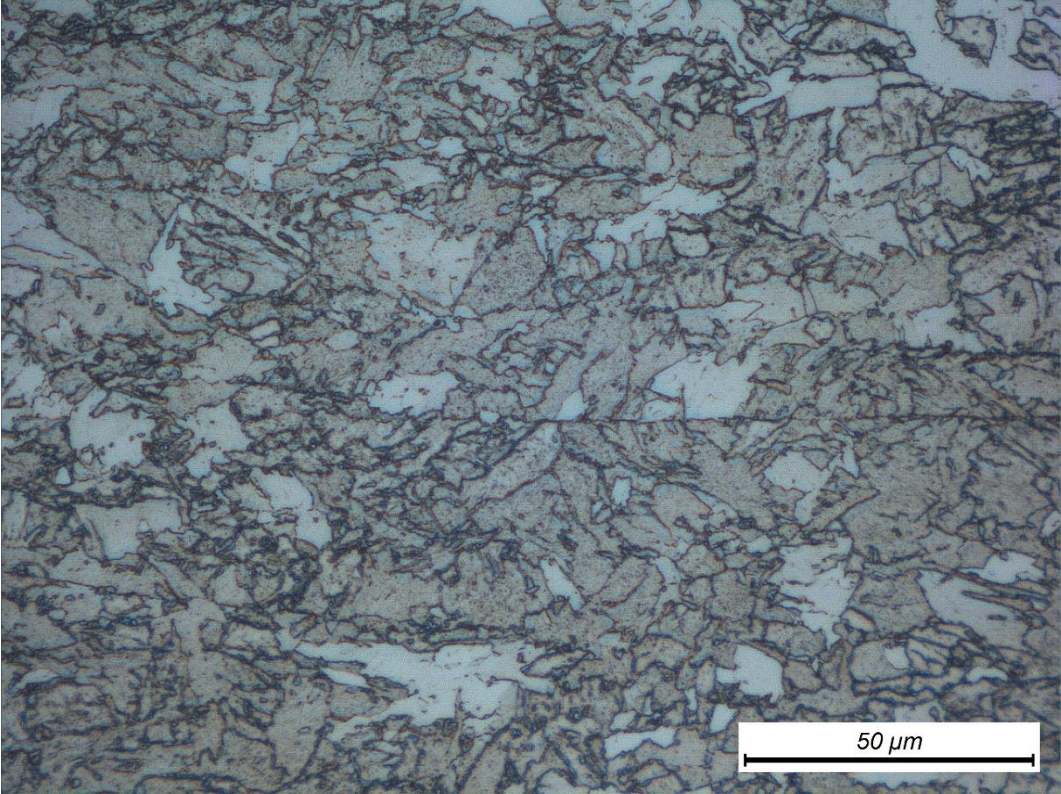
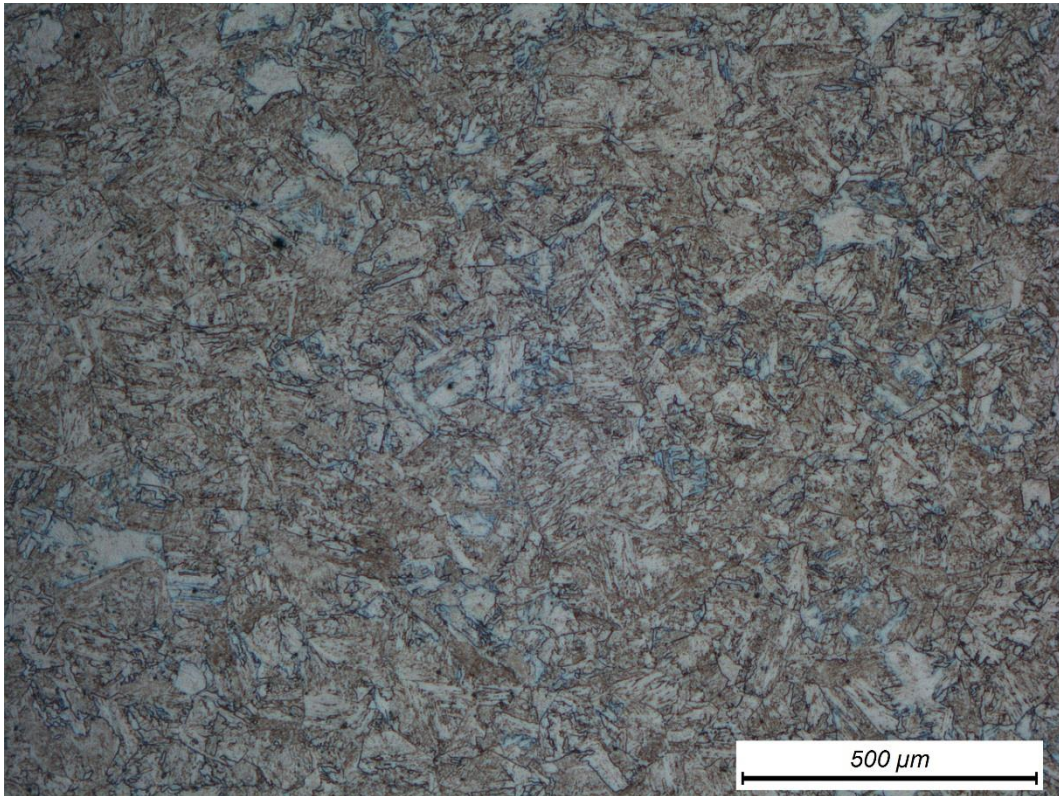
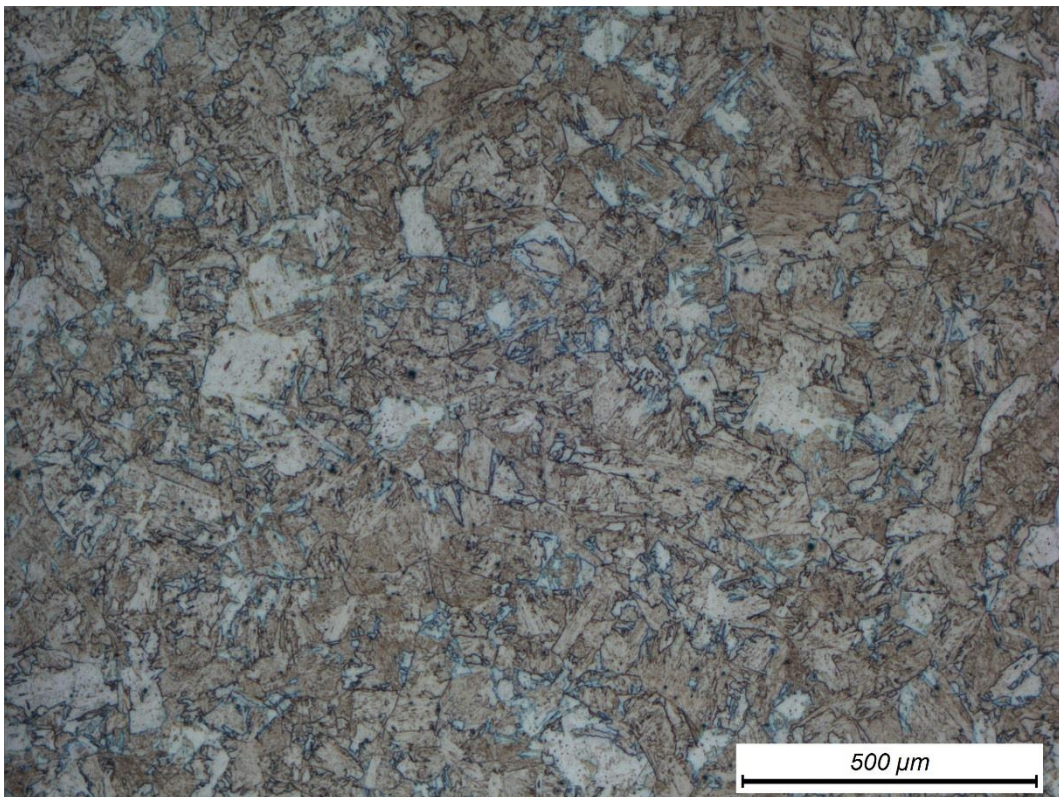


Figure 77 - Micrograph of the base material in sample 12





*Figure 78 – Micrograph of sample 7 (CGHAZ 15)*



*Figure 79 – Micrograph of sample 12 (ICCGHAZ 15)*



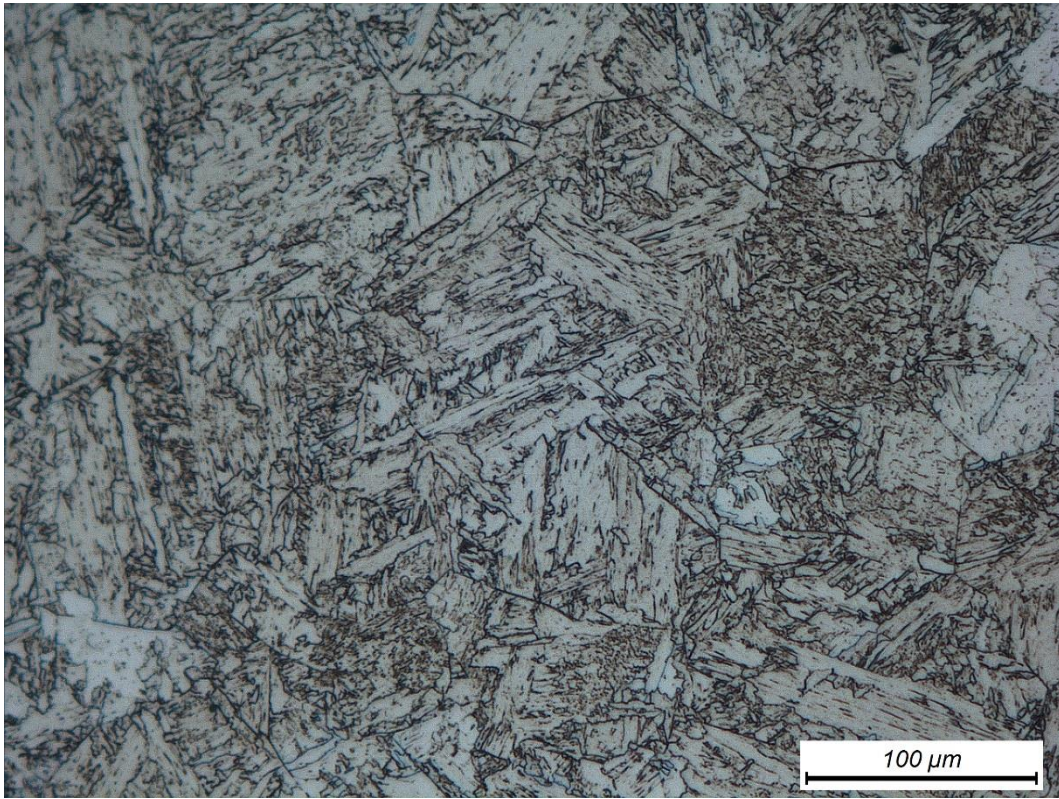


*Figure 80 – Micrograph of sample 17 (ICCGHAZ 10)*

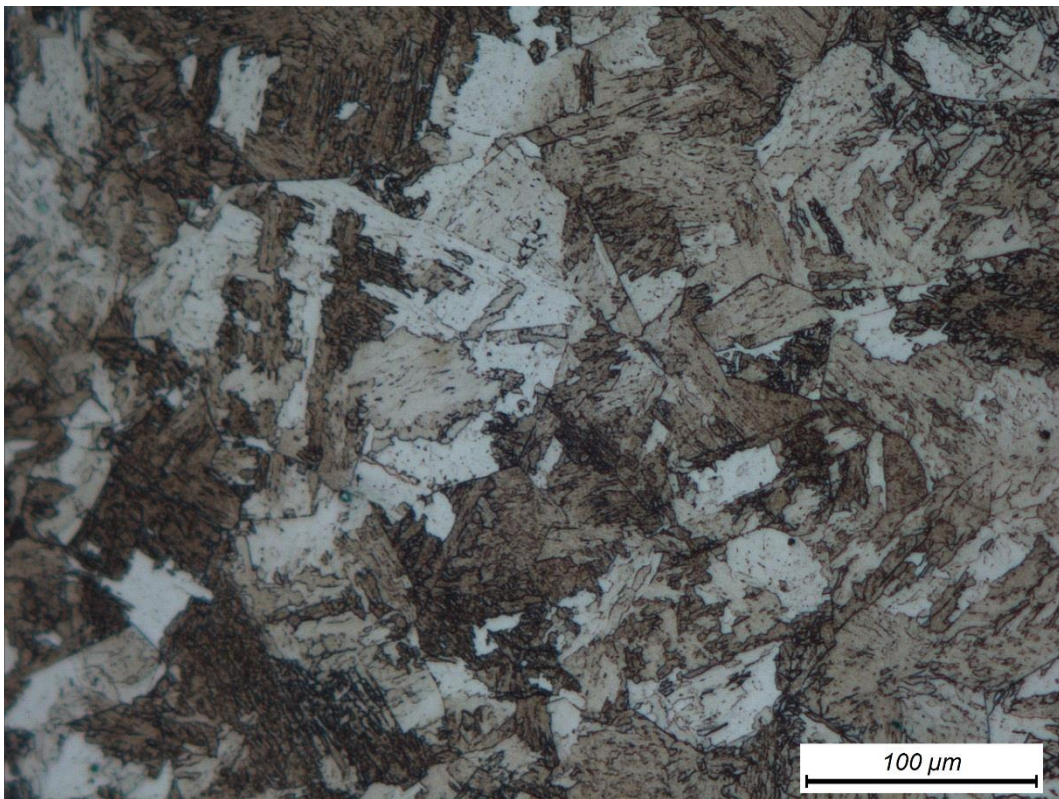


*Figure 81 – Micrograph of sample 18 (CGHAZ 10)*



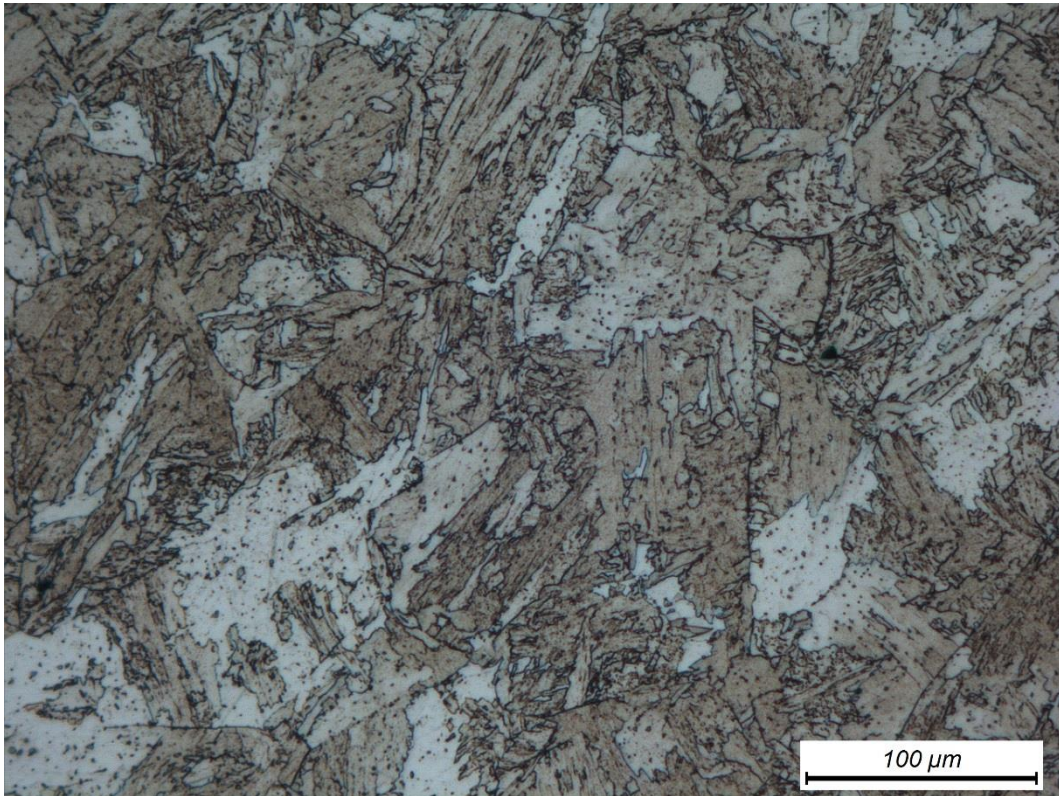


*Figure 82 – Micrograph of sample 24 (ICCGHAZ 10)*

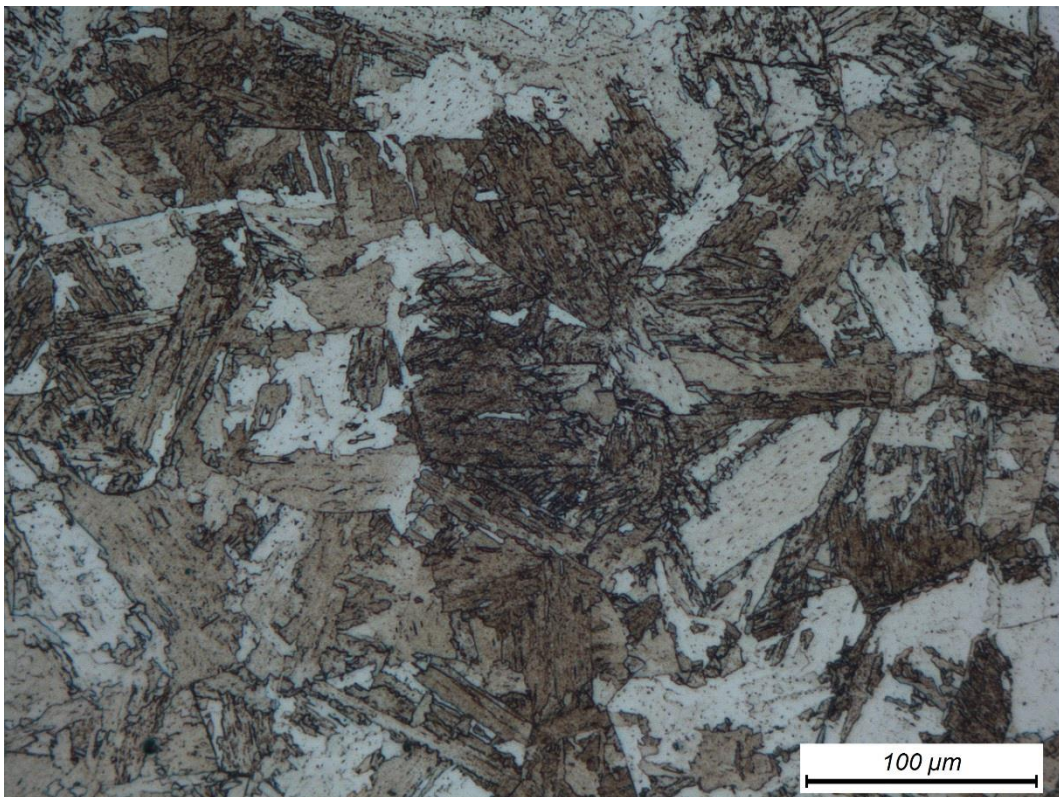


*Figure 83 – Micrograph of sample 36 (ICCGHAZ 5)*



9.3 FRACTOGRAPHS

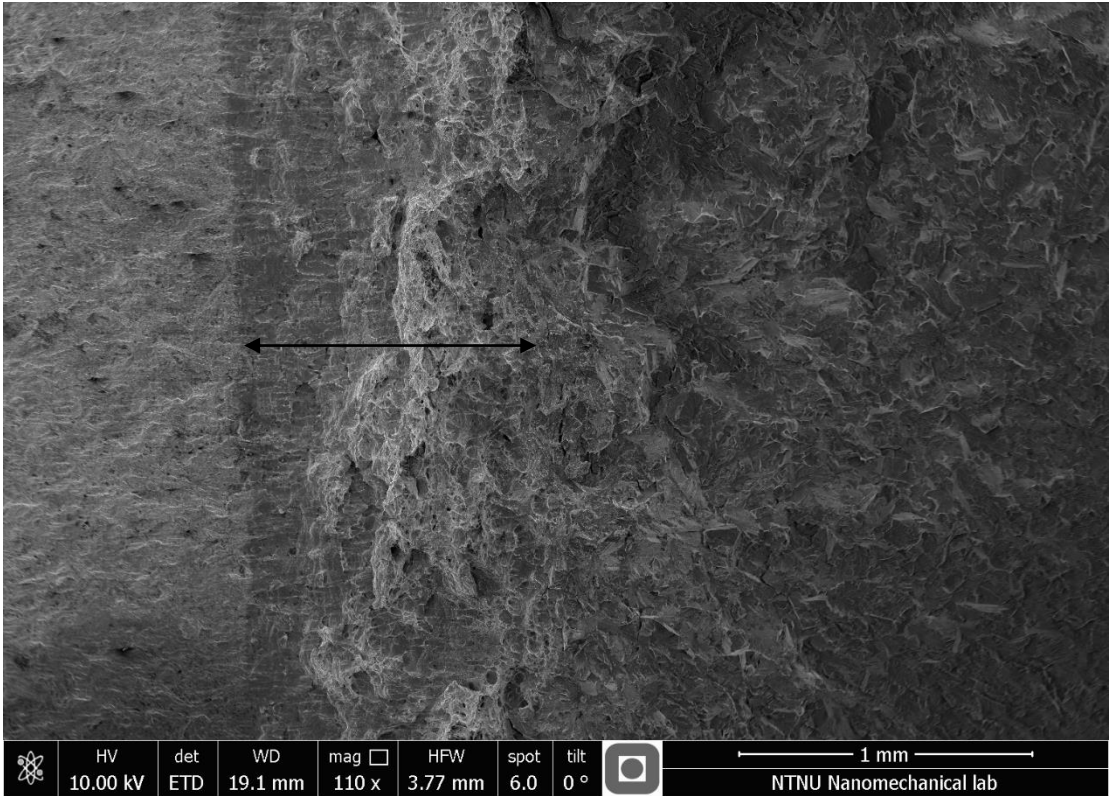


Figure 84 – SEM fractograph of sample 24 (ICCGHAZ 10), arrow indicating ductile area after the fatigue notch

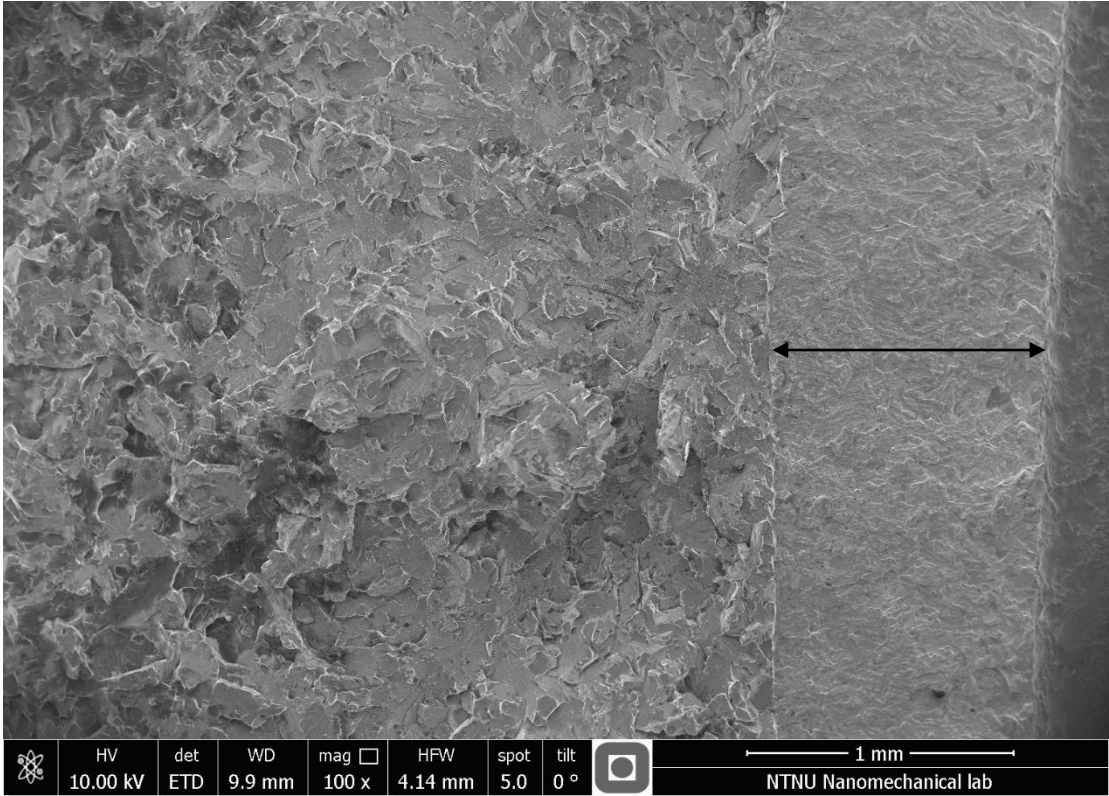


Figure 85 – SEM fractograph sample 138 (CGHAZ 15), arrow indicating fatigue notch

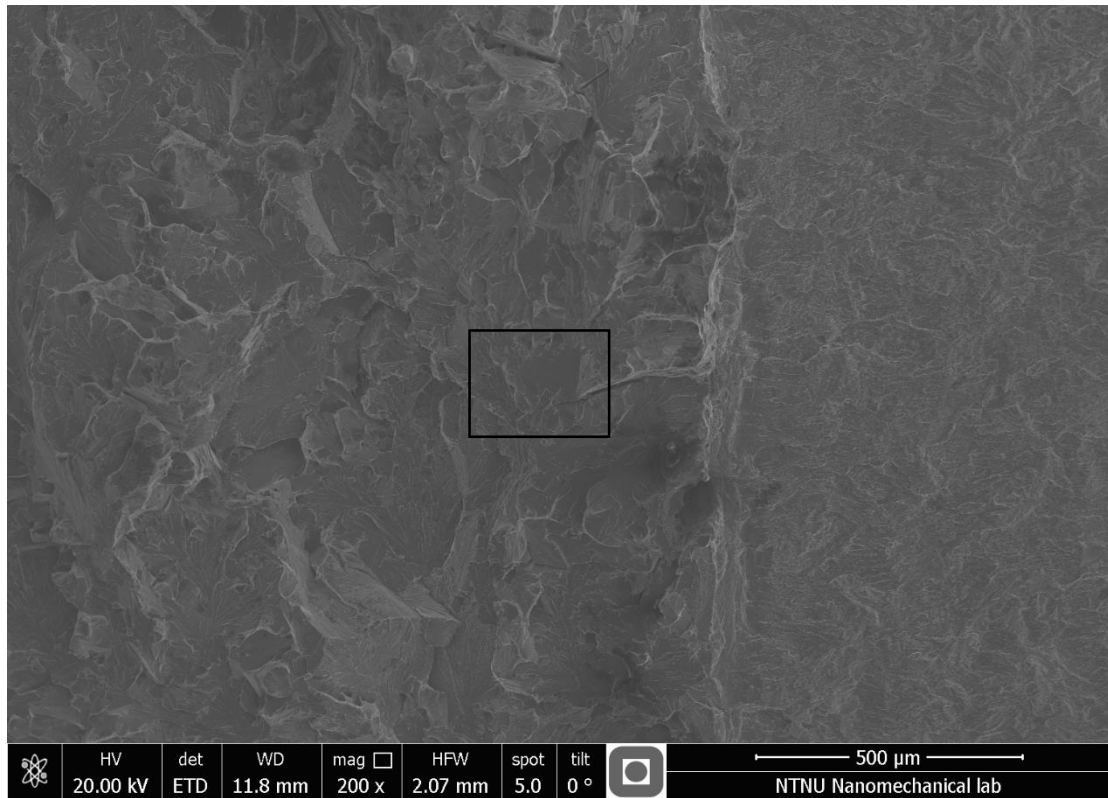


Figure 86 – SEM fractograph of sample 139 (CGHAZ 25), overview indicating flat area

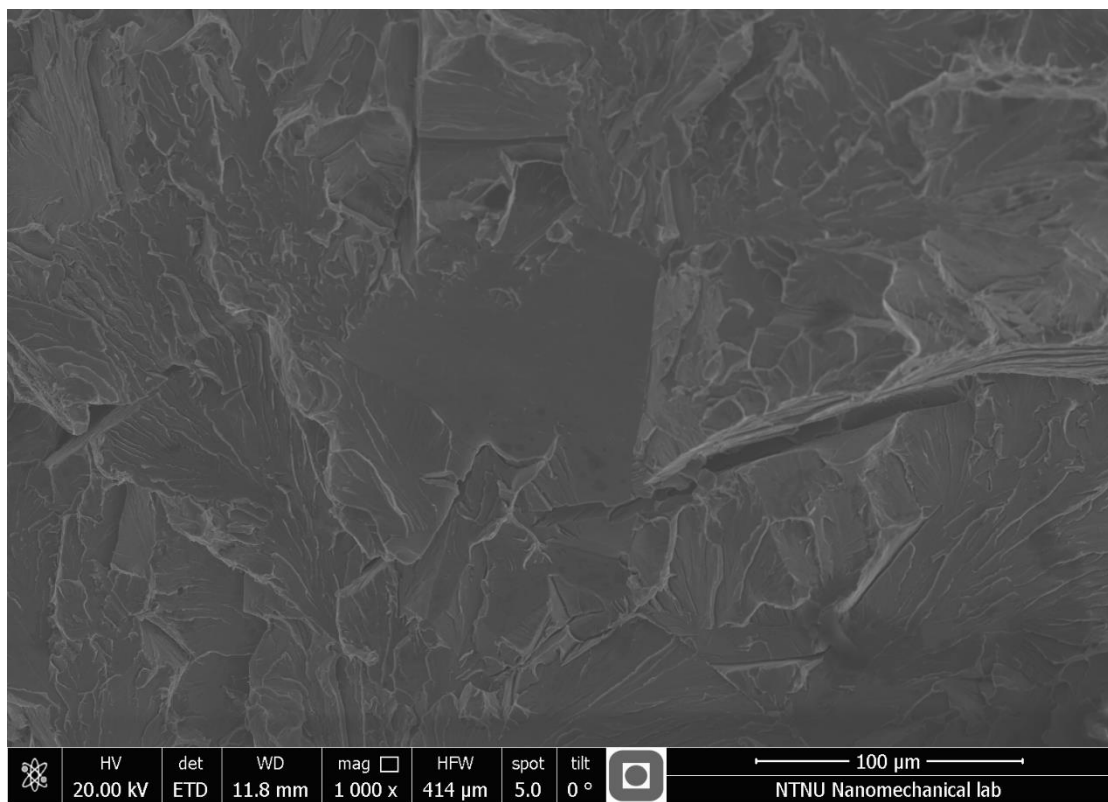


Figure 87 – SEM fractograph of sample 139 (CGHAZ 25), close-up of flat area

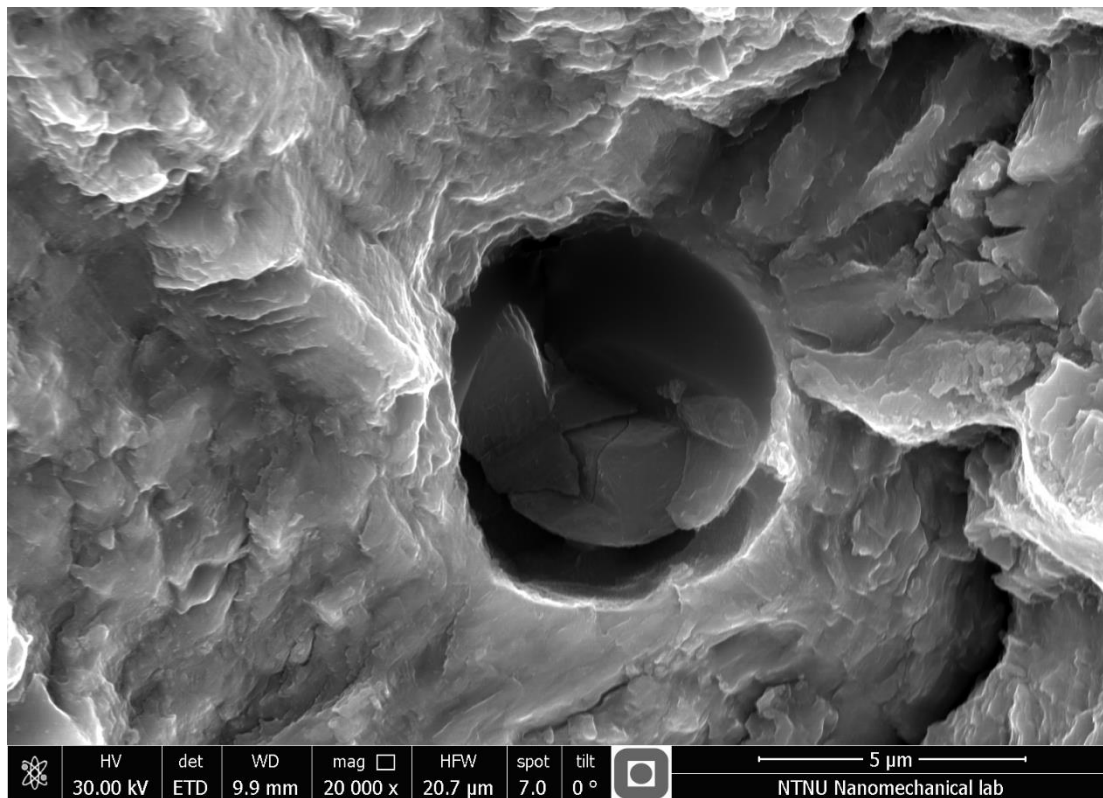


Figure 88 – SEM fractograph of fractured particle in sample 167 (CGHAZ 5), approx. 100 μm from the pre-test fatigue notch.

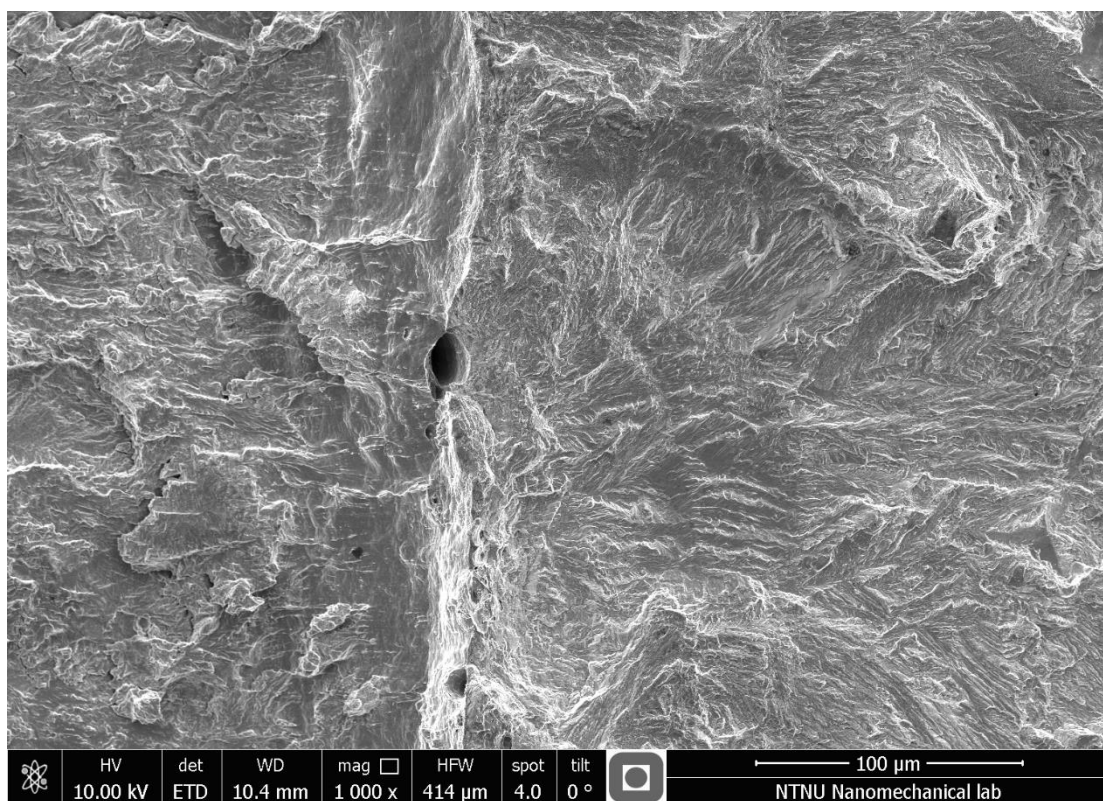


Figure 89 – SEM fractograph of a big isolated dimple just after the stretch zone in sample 180 (CGHAZ 15)

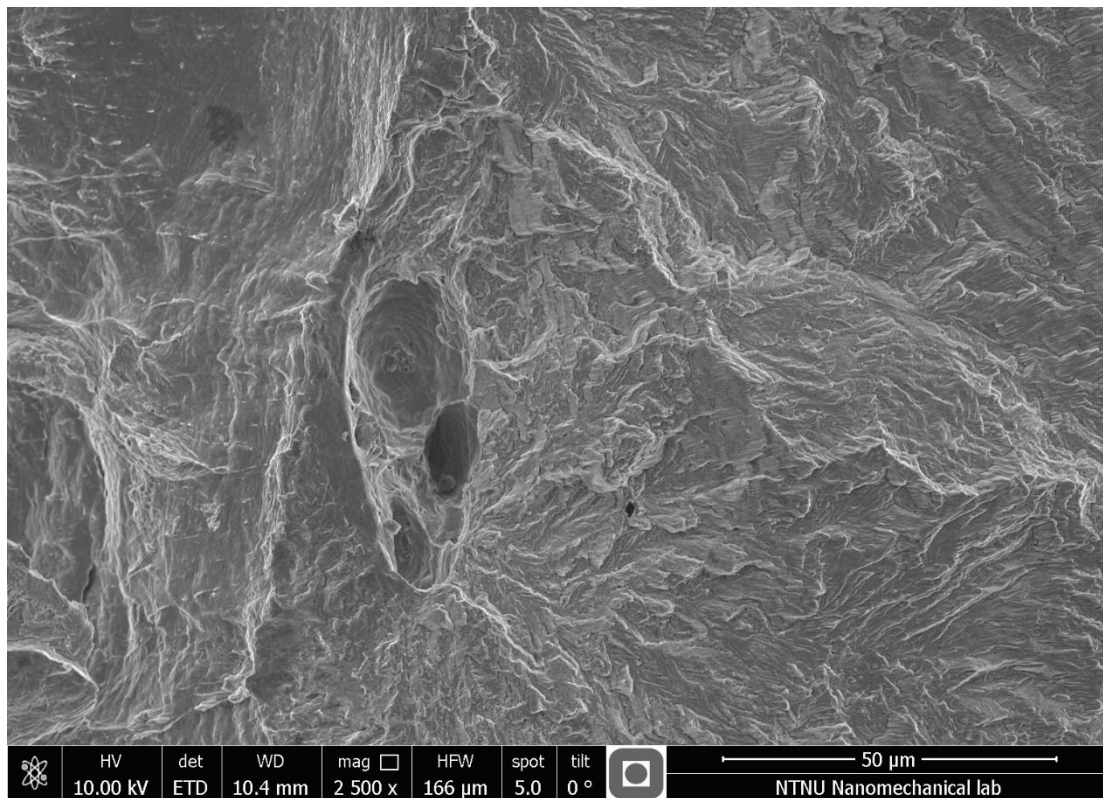


Figure 90 – SEM fractograph of a big dimple in sample 180 (CGHAZ 15), just after the fatigue notch

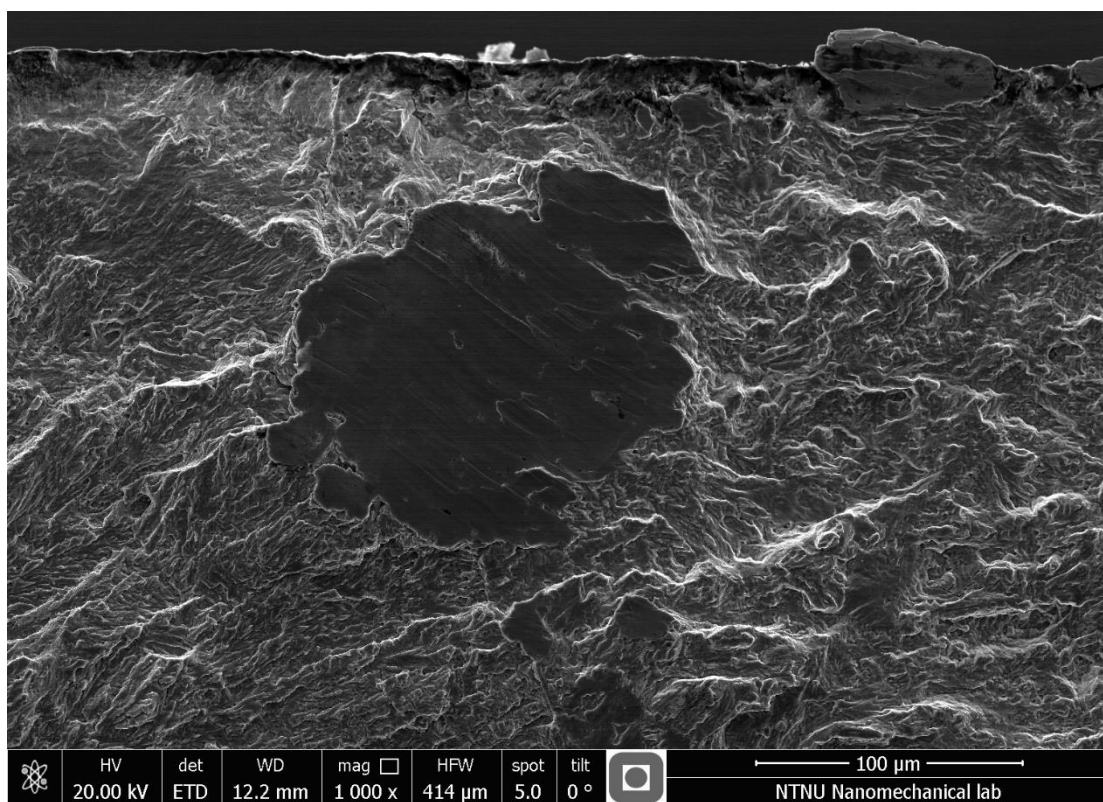


Figure 91 – SEM fractograph of flat area at the fatigue notch in sample 217 (CGHAZ 5), which didn't have a matching area on the opposite fracture surface



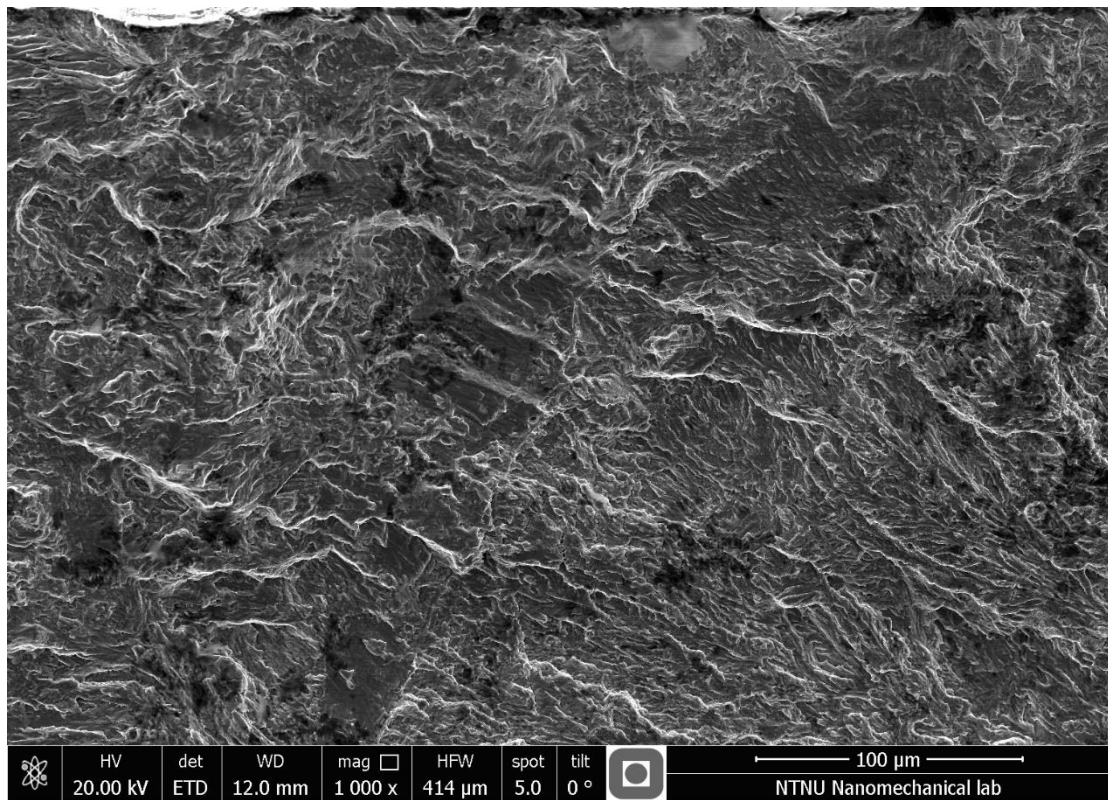


Figure 92 – SEM fractograph of the area in which the flat area in Figure 91 should have been.

## 9.4 RISK ASSESSMENT



### Detaljert Risik rapport (ny)

<b>ID</b>	220	<b>Status</b>	<b>Dato</b>
<b>Risikoområde</b>	Risikovurdering: Helse, miljø og sikkerhet (HMS)	Opprettet	19.02.2015
<b>Opprettet av</b>	Cathrine Gjerstad Hartwig	Vurdering startet	19.02.2015
<b>Ansvarlig</b>	Cathrine Gjerstad Hartwig	Tiltak besluttet	
		Avsluttet	

#### Metallography lab Cathrine Hartwig

##### gyldig i perioden:

2/19/2015 - 6/10/2015

##### Mål / hensikt

- .. Risk assessment on the activity in the metallurgy laboratory including cutting, grinding and polishing
- .. Proper use of fume-hood for cleaning, etching and electro-polishing

##### Bakgrunn

.. ensure safe working condition and avoiding accident.

##### Beskrivelse og avgrensninger

- .. Cutting samples with Struers Unitom
- .. Grinding and Polishing samples on rotary wheel using SiC paper, diamond pad and diamond paste
- .. Fume-hood activity (cleaning, etching, electro-polishing)

##### Forutsetninger, antakelser og forenklinger

[Ingen registreringer]

##### Redlegg

[Ingen registreringer]

##### Referanser

[Ingen registreringer]

*Dr. Ueland*

*Cathrine Hartwig*

*N. Klud*

NTNUs teknisk-naturvitenskapelige universitet (NTNU)

Regulert av offentlighetsloven § 14

Utskriftsdato:

19.02.2015

Utskrift foretatt av:

Cathrine Gjerstad Hartwig

Side:

1/9

**Oppsummering, resultat og endelig vurdering**

I oppsummeringen presenteres en oversikt over farer og uønskede hendelser, samt resultat for det enkelte konsekvensområdet.

**Farekilde:** Cutting activity

**Uønsket hendelse:** Broken cutting machine

**Konsekvensområde:** Ytre miljø  
Materielle verdier

Risiko før tiltak:  Risiko etter tiltak:

Risiko før tiltak:  Risiko etter tiltak:

**Uønsket hendelse:** Flying Debris

**Konsekvensområde:** Ytre miljø

Risiko før tiltak:  Risiko etter tiltak:

**Farekilde:** Grinding and Polishing

**Uønsket hendelse:** Wearing of finger tip and skin

**Konsekvensområde:** Helse

Risiko før tiltak:  Risiko etter tiltak:

**Farekilde:** Fume-hood activity (Etching)

**Uønsket hendelse:** Skin irritation

**Konsekvensområde:** Helse

Risiko før tiltak:  Risiko etter tiltak:

**Farekilde:** Fume-hood activity (Cleaning)

**Uønsket hendelse:** Splash of the solvent

**Konsekvensområde:** Helse

Risiko før tiltak:  Risiko etter tiltak:

**Farekilde:** Microscopy analysis

**Uønsket hendelse:** Scratching the optic of microscope

**Konsekvensområde:** Materielle verdier

Risiko før tiltak:  Risiko etter tiltak:

**Endelig vurdering**



### Oversikt involverte enheter og personell

En risikovurdering kan gjelde for en, eller flere enheter i organisasjonen. Denne oversikten presenterer involverte enheter og personell for gjeldende risikovurdering.

#### Enheter /-er risikovurderingen omfatter

- Norges teknisk-naturvitenskapelige universitet

#### Deltakere

[Ingen registreringer]

#### Lesere

[Ingen registreringer]

#### Andre involverte/interessenter

[Ingen registreringer]

Følgende akseptkriterier er besluttet for risikoområdet Risikovurdering: Helse, miljø og sikkerhet (HMS):

Helse	Materielle verdier	Omsømme	Ytre miljø

**Oversikt over eksisterende, relevante tiltak som er hensyntatt i risikovurderingen**

I tabellen under presenteres eksisterende tiltak som er hensyntatt ved vurdering av sannsynlighet og konsekvens for aktuelle uønskede hendelser.

Farekilde	Uønsket hendelse	Tiltak hensyntatt ved vurdering
Cutting activity	Broken cutting machine	
	Flying Debris	
Grinding and Polishing	Wearing of finger tip and skin	
Fume-hood activity (Etching)	Skin irritation	
Fume-hood activity (Cleaning)	Splash of the solvent	
Microscopy analysis	Scratching the optic of microscope	

**Eksisterende og relevante tiltak med beskrivelse:****Risikoanalyse med vurdering av sannsynlighet og konsekvens**

I denne delen av rapporten presenteres detaljer dokumentasjon av de farer, uønskede hendelser og årsaker som er vurdert. Innledningsvis oppsummeres farer med tilhørende uønskede hendelser som er tatt med i vurderingen.

**Følgende farer og uønskede hendelser er vurdert i denne risikovurderingen:**

- **Cutting activity**
  - Broken cutting machine
  - Flying Debris
- **Grinding and Polishing**
  - Wearing of finger tip and skin
- **Fume-hood activity (Etching)**
  - Skin irritation
- **Fume-hood activity (Cleaning)**
  - Splash of the solvent
- **Microscopy analysis**
  - Scratching the optic of microscope

**Oversikt over besluttede risikoreducerende tiltak med beskrivelse:**



Cutting activity (fareklilde)

Cutting activity/Broken cutting machine (uønsket hendelse)

The incorrect setting of the machine may lead to broken cutting wheel, clamping or clogging the machine, damaging the sample stage and motor and damaging/destroying the samples

Samlet sannsynlighet vurdert for hendelsen: Lite sannsynlig (2)

Kommentar til vurdering av sannsynlighet:

1. Obligatory to supervise the cutting activity
2. Instruction manual is followed accordingly
3. Automatic calibration in the precision cutting to ensure all function running properly

Vurdering av risiko for følgende konsekvensområde: Ytre miljø

Vurdert sannsynlighet (felles for hendelsen): Lite sannsynlig (2)

Vurdert konsekvens: Liten (1)

Kommentar til vurdering av konsekvens:

[Ingen registreringer]



Cutting activity/Flying Debris (uønsket hendelse)

The debris from cutting activity would fly and hurt user if the lid/door are opened before the wheel stops completely

Samlet sannsynlighet vurdert for hendelsen: Svært lite sannsynlig (1)

Kommentar til vurdering av sannsynlighet:

1. The lid/door of the machine is never opened when the wheel is running
2. Automatic stop in precision cutting machine when the lid is open
3. The user has to always wear goggles

Vurdering av risiko for følgende konsekvensområde: Ytre miljø

Vurdert sannsynlighet (felles for hendelsen): Svært lite sannsynlig (1)

Vurdert konsekvens: Liten (1)

Kommentar til vurdering av konsekvens:

[Ingen registreringer]



**Grinding and Polishing (farekilde)**

1. Grinding of the samples with SIC paper or diamond pad
2. Polishing of the samples with polishing pad and diamond particles spray

**Grinding and Polishing/Wearing of finger tip and skin (uønsket hendelse)**

1. The tip of the finger and the skin could wear off due to un-proper techniques of grinding and polishing
2. Glove are not used during activity

Samlet sannsynlighet vurdert for hendelsen: Sannsynlig (3)

Kommentar til vurdering av sannsynlighet:

1. The user is not familiar with the proper technique of grinding and polishing
2. The user are required to wear gloves, lab-coat and goggles

**Vurdering av risiko for følgende konsekvensområde: Helse**

Vurdert sannsynlighet (felles for hendelsen): Sannsynlig (3)

Vurdert konsekvens: Liten (1)

Kommentar til vurdering av konsekvens:

small wear of the tip of the finger without bleeding

**Fume-hood activity (Etching) (farekilde)****Fume-hood activity (Etching)/Skin irritation (uønsket hendelse)**

Irritation from the etching liquid

Samlet sannsynlighet vurdert for hendelsen: Svært lite sannsynlig (1)

Kommentar til vurdering av sannsynlighet:

1. Etching is performed in fume-hood
2. The user are equipped with gloves, lab-coat and goggles

**Vurdering av risiko for følgende konsekvensområde: Helse**

Vurdert sannsynlighet (felles for hendelsen): Svært lite sannsynlig (1)

Vurdert konsekvens: Stor (3)

Kommentar til vurdering av konsekvens:

[Ingen registreringer]







**Fume-hood activity (Cleaning) (farekilde)**

Cleaning of samples using ethanol absolute, isopropanol or acetone in ultrasonic bath

**Fume-hood activity (Cleaning)/Splash of the solvent (uønsket hendelse)**

Splash or direct contact with ethanol, isopropanol or acetone

Samlet sannsynlighet vurdert for hendelsen: Sannsynlig (3)

Kommentar til vurdering av sannsynlighet:

1. Solvent bottle are manually pressurized to deliver the solvent

**Vurdering av risiko for følgende konsekvensområde: Helse**

Vurdert sannsynlighet (felles for hendelsen): Sannsynlig (3)

Vurdert konsekvens: Liten (1)

Kommentar til vurdering av konsekvens:

[Ingen registreringer]



**Microscopy analysis (farekilde)**

Analyze microstructures with light microscopy

**Microscopy analysis/Scratching the optic of microscope (uønsket hendelse)**

The optic of the microscope is very sensitive to scratch

Samlet sannsynlighet vurdert for hendelsen: Lite sannsynlig (2)

Kommentar til vurdering av sannsynlighet:

1. Magnification is performed in step-wise manner
2. Safe guard ring installed

**Vurdering av risiko for følgende konsekvensområde: Materielle verdier**

Vurdert sannsynlighet (felles for hendelsen): Lite sannsynlig (2)

Vurdert konsekvens: Liten (1)

Kommentar til vurdering av konsekvens:

[Ingen registreringer]





**Oversikt over besluttede risikoreducerende tiltak:**

Under presenteres en oversikt over risikoreducerende tiltak som skal bidra til å reduseres sannsynlighet og/eller konsekvens for uønskede hendelser.

**Oversikt over besluttede risikoreducerende tiltak med beskrivelse:**

